

**POWER REFLECTION AND TRANSMISSION
COEFFICIENTS FOR A CHIRAL SLAB AND MEANDER
LINE POLARIZER WITH CHIRAL SLAB**

77702

A MASTER'S THESIS

in

Electrical and Electronics Engineering

University of Gaziantep

By

Kemal DELIHACIOĞLU

November, 1998


Approval of the Graduate School of Natural Applied Sciences



Assoc. Prof. Dr. Ali Rıza TEKİN

Director

I certify that this thesis satisfies all the requirements as a thesis for the degree of Master of Science.



Prof. Dr. Tuncay EGE

Chairman of the Department

I certify that I have read this thesis and that in my opinion it is fully adequate, in scope and quality, as a thesis for the degree of Master of Science.



Asst. Prof. Dr. Savaş UÇKUN

Supervisor

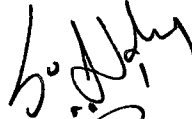
Examining Committee in Charge:

Prof. Dr. Tuncay EGE

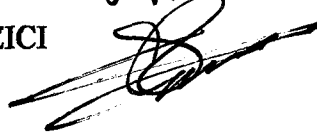
(Chairman)



Asst. Prof. Dr. Savaş UÇKUN



Prof. Dr. Sadettin ÖZYAZICI



ABSTRACT

POWER REFLECTION AND TRANSMISSION
COEFFICIENTS FOR A CHIRAL SLAB AND
MEANDER – LINE POLARIZER WITH CHIRAL SLAB

DELİHACIOĞLU Kemal

M.S. in Electrical and Electronics Engineering

Supervisor: Asst. Prof. Dr. Savaş UÇKUN

November 1998, 97 pages

In this study, the power reflection and transmission coefficients have been analyzed for TE and TM incident plane waves on a chiral slab and meander – line polarizer with chiral slab.

In the analysis of chiral slab without meander-line polarizer, the electric and magnetic fields are written in terms of the modal fields for a linearly polarized and circularly polarized fields in air and chiral regions, respectively. In the chiral region the electric and magnetic fields are expressed as the sum of left circularly polarized (LCP) and right circularly polarized (RCP) plane waves whereas in the air region a linearly polarized TE or TM wave is assumed and incident on a chiral slab. The derivation of power reflection

and transmission coefficients are realized in a straightforward manner after matching the tangential components of the electric and magnetic fields at the boundaries. Since at the boundary tangential components of the electric and magnetic fields are continuous.

For a meander-line polarizer with chiral slab, the fields are derived in modal form both in air and chiral regions. Meander-line strip is placed periodically in the xy plane. It is assumed to be infinitely thin and conducting perfectly. Due to the periodicity of the problem the fields are expanded into Floquet modes in the air and chiral regions. The boundary conditions combined with the orthogonality of the Floquet modes over a single periodic unit cell, lead to an integral equation for the unknown current density, induced on the metallic part of the meander-line by the incident plane wave. This integral equation can be solved by using the moment method by expanding the unknown current density in terms of a set of basis functions and testing with the same basis. The solution of the resulting matrix equations is carried out by the complex matrix inversion program. The power reflection and transmission coefficients can easily be found from the electric field equations by using the Poynting vector.

As a result, the power reflection and transmission coefficients have been plotted with respect to frequency and incident angle for different values of chirality admittance, slab thickness, and relative permittivity of the chiral medium.

Keywords : Meander – line , chiral

ÖZET

SİMETRİSİZ LEVHANIN VE SİMETRİSİZ LEVHA ÜZERİNE
YERLEŞTİRİLEN MENDERES BİÇİMLİ POLARİZÖRLERİN
YANSIMA VE İLETİM GÜÇ KATSAYILARININ BULUNMASI

DELİHACIOĞLU Kemal

Yüksek Lisans Tezi, Elektrik ve Elektronik Mühendisliği A.B.D.

Tez Yöneticisi: Yrd. Doç. Dr. Savaş UÇKUN

Kasım 1998, 97 sayfa

Bu çalışmada, simetrisiz(chiral) bir ortama ve simetrisiz ortam üzerine yerleştirilmiş menderes biçimli polarizöre, TE ya da TM olarak gelen düzlemsel dalgaların oluşturduğu yansıyan ve iletilen güç katsayılarının analizi yapıldı.

Simetrisiz ortamın analizinde, elektrik ve manyetik alanlar hem doğrusal hem de dairesel polarizasyonlu dalgalar için hava ve simetrisiz ortamda modal olarak yazıldı. Simetrisiz ortamda elektrik ve manyetik alanlar sağ ve sol el polarizasyonlu dalgaların toplamı olarak yazıldı. Elektrik ve manyetik alanların sınır şartlarını

sağlamasından sonra yansıyan ve iletilen güç katsayıları direkt olarak bulundu.

Simetrisiz levha üzerine yerleştirilmiş menderes biçimli polarizör için, yine elektrik ve manyetik alanlar hava ve simetrisiz ortamda modal olarak türetildi. Menderes biçimli polarizör x-y düzlemine periyodik olarak yerleştirildi. Problemin periyodik olmasından dolayı elektrik ve manyetik alanlar hava ve simetrisiz ortamda Floquet modları cinsinden yazıldı. Tek bir birim hücre üzerinde sınır şartları ve Floquet modlarının dikgen özelliğinin birleştirilmesiyle, gelen düzlemsel TE ya da TM dalga, metal kısmın üzerinde bilinmeyen akım yoğunluğu cinsinden bir integral denklemi verir. Bilinmeyen akım yoğunluğu temel fonksiyonlar cinsinden yazılıp, moment metodu kullanılarak çözüldü. Elde edilen matris denkleminin çözümü matrisin tersinin alınmasıyla gerçekleşti. Yansıyan ve iletilen güç katsayıları elektrik alan denklemlerinden Poynting vektör kullanılarak kolayca bulundu.

Sonuç olarak, yansıyan ve iletilen güç katsayıları, chirality admittansının, levha kalınlığının ve dielektrik sabitinin farklı değerleri için frekansa ve geliş açısına göre grafikleri çizildi.

Anahtar kelimeler: Menderes biçimli , simetrisiz

ACKNOWLEDGEMENT

I would like to present my gratitude to supervisor Asst. Prof. Dr. Savaş UÇKUN for his guidance and valuable suggestions.

I am greatly indebted to my family and my wife for their patience and encouragements.

I also thank my little cute son, Cevdet Can, for his generous love.



TABLE OF CONTENTS

	Page
ABSTRACT.....	iii
ÖZET.....	v
ACKNOWLEDGEMENT.....	vii
LIST OF FIGURES.....	x
1. INTRODUCTION.....	1
1.1. Electromagnetic Chirality.....	1
1.2. Meander – line Polarizer.....	5
1.3. Summary of Chapters	9
2. ANALYSIS OF CHIRAL SLAB.....	11
2.1. Propagation of Wave in Chiral Medium.....	11
2.2. Modal Fields in Air and Chiral Mediums.....	13
2.2.1. Modal Field for TM Incident Wave.....	14
2.2.2. Modal Field for TE Incident Wave.....	15
2.2.3. Modal Field for LCP Wave.....	16
2.2.4. Modal Field for RCP Wave.....	17
2.3. Power Reflection and Transmission Coefficient for a Chiral Slab (TM Incidence).....	17

	Page
2.4. Power Reflection and Transmission Coefficient for a Chiral Slab (TE Incidence).....	20
2.5. Numerical Results of the Chiral Slab.....	23
3. ANALYSIS OF MEANDER – LINE POLARIZER WITH CHIRAL SLAB.....	43
3.1. Floquet Theorem.....	43
3.2. Formulation of the Problem.....	50
4. SOLUTION BY MOMENT METHOD	60
4.1. Calculation of Inner Products.....	60
4.2. Numerical Results of Meander – line Polarizer.....	67
5. CONCLUSION.....	92
REFERENCES.....	94

LIST OF FIGURES

Figure		Page
2.1	Wave propagation in \vec{a}_r direction.....	14
2.2	Normalized power reflection and transmission coefficients against frequency for different values of chirality admittance; TE normal incidence, $\epsilon_r=2$ and $d=6.25$ mm. (a)- Power reflection coefficient TE, (b)- Power transmission coefficient TE, (c)- Power transmission coefficient TM.....	29
2.3	Normalized power reflection and transmission coefficients against frequency for different values of slab thickness; TE normal incidence; $\xi=0.003$ S and $\epsilon_r=2$. (a)- Power reflection coefficient TE, (b)- Power transmission coefficient TE, (c)- Power transmission coefficient TM.....	30
2.4	Normalized power reflection and transmission coefficients against frequency for different values of dielectric constant; TE normal incidence, $\xi=0.003$ S and $d=6.25$ mm. (a)- Power reflection coefficient TE, (b)- Power transmission coefficient TE, (c)- Power transmission coefficient TM.....	32
2.5	Normalized power reflection and transmission coefficients against incident angle θ for different values of chirality admittances; TM incidence, $\epsilon_r=9$ and $d=6.25$ mm. (a) – Power reflection coefficient TM, (b) – Power transmission coefficient TM, (c) – Power transmission coefficient TE.....	34
2.6	Normalized power reflection and transmission coefficients against incident angle θ for different values of slab thickness; TM incidence, $\xi=0.005$ S and $\epsilon_r=9$. (a) – Power reflection coefficient TM, (b) – Power	

	transmission coefficient TM, (c) – Power transmission coefficient TE.....	35
2.7	Normalized power reflection and transmission coefficients against incident angle θ for different values of dielectric constant; TM incidence, $\xi=0.005$ S and $d=6.25$ mm. (a) – Power reflection coefficient TM, (b) – Power transmission coefficient TM, (c) – Power transmission coefficient TE.....	37
2.8	Normalized power reflection and transmission coefficients against incident angle θ for different values of chirality admittances; TE incidence $\epsilon_r=9$ and $d=6.25$ mm. (a) – Power reflection coefficient TE, (b) – Power transmission coefficient TE, (c) – Power transmission coefficient TM.....	39
2.9	Normalized power reflection and transmission coefficients against incident angle θ for different values of slab thickness; TE incidence, $\epsilon_r=9$ and $\xi=0.005$ S. (a) – Power reflection coefficient TE, (b) – Power transmission coefficient TE, (c) – Power transmission coefficient TM.....	40
2.10	Normalized power reflection and transmission coefficients against incident angle θ for different values of dielectric constant; TE incidence, $\xi=0.005$, $d=6.25$ mm. (a) – Power reflection coefficient TE , (b) – Power transmission coefficient TE , (c) – Power transmission coefficient TM.	42
3.1	Geometry of the Meander – line polarizer.....	44
3.2	Lattice geometry.....	47
3.3	Side view of Meander – line polarizer	51
4.1	Subdivision of the periodic unit cell of Meander – line	61
4.2	Normalized power reflection and transmission coefficients against frequency for different values of chirality admittances; TE normal	

	incidence , $\epsilon_r=2.0$ and $d=6.25$ mm. (a) – Power reflection coefficient TE, (b)–Power transmission coefficient TE ,(c)–Power transmission coefficient TM.....	73
4.3	Normalized power reflection and transmission coefficients against frequency for different values of slab thickness; TE normal incidence , $\xi=0.003$ S and $\epsilon_r=2$. (a) – Power reflection coefficient TE, (b) – Power transmission coefficient TE , (c) – Power transmission coefficient TM	74
4.4	Normalized power reflection and transmission coefficients against frequency for different values of dielectric constant; TE normal incidence , $\xi=0.003$ S and $d=6.25$ mm. (a)–Power reflection coefficient TE, (b) – Power transmission coefficient TE , (c) – Power transmission coefficient TM	76
4.5	Normalized power reflection and transmission coefficients against frequency for different values of chirality admittances; TM normal incidence, $d=6.25$ mm and $\epsilon_r=2.0$. (a)–Power reflection coefficient TM, (b)–Power transmission coefficient TM, (c) – Power transmission coefficient TE.....	78
4.6	Normalized power reflection and transmission coefficients against frequency for different values of slab thickness; TM normal incidence, $\xi=0.003$ S and $\epsilon_r=2.0$. (a) – Power reflection coefficient TM , (b)–Power transmission coefficient TM , (c)–Power transmission coefficient TE.....	79
4.7	Normalized power reflection and transmission coefficients against frequency for different values of dielectric constants; TM normal incidence, $\xi=0.003$ S and $d=6.25$ mm. (a) – Power reflection coefficient TM , (b) – Power transmission coefficient TM , (c) – Power transmission coefficient TE.....	81
4.8	Normalized power reflection and transmission coefficients against incident angle θ for different values of chirality admittances; TE	

	incidence, $\epsilon_r=9$ and $d=6.25$ mm. (a) – Power reflection coefficient TE, (b) – Power transmission coefficient TE, (c) – Power transmission coefficient TM.....	83
4.9	Normalized power reflection and transmission coefficients against incident angle θ for different values of slab thickness; TE incidence, $\xi=0.005$ S and $\epsilon_r=9$. (a) – Power reflection coefficient TE, (b) – Power transmission coefficient TE, (c) – Power transmission coefficient TM.....	84
4.10	Normalized power reflection and transmission coefficients against incident angle θ for different values of dielectric constant; TE incidence and $\xi=0.005$ S and $d=6.25$ mm. (a) – Power reflection coefficient TE, (b) –Power transmission coefficient TE, (c) – Power transmission coefficient TM.....	86
4.11	Normalized power reflection and transmission coefficients against incident angle θ for different values of chirality admittances; TM incidence, $\epsilon_r=9$ and $d=6.25$ mm. (a) – Power reflection coefficient TM, (b) – Power transmission coefficient TM, (c) – Power transmission coefficient TE.....	88
4.12	Normalized power reflection and transmission coefficients against incident angle θ for different values of slab thickness; TM incidence, $\xi=0.005$ S and $\epsilon_r=9$. (a) – Power reflection coefficient TM, (b) – Power transmission coefficient TM, (c) – Power transmission coefficient TE.....	89
4.13	Normalized power reflection and transmission coefficients against incident angle θ for different values of dielectric constant; TM incidence, $\xi=0.005$ S and $d=6.25$ mm. (a) – Power reflection coefficient TM, (b) – Power transmission coefficient TM, (c)–Power transmission coefficient TE.....	91

CHAPTER 1

INTRODUCTION

1.1 Electromagnetic Chirality

The lack of geometric symmetry between an object and its mirror image is referred to as chirality. The mirror image of such a chiral object can not be made to coincide with the object itself by any operation involving rotations and/or translations. An object of this kind has the property of handedness either left or right handed. An object that is not chiral is said to be achiral. A chiral object and its mirror image are enantiomorphs of each other. If a chiral object is left (right) handed, its mirror image (enantiomorph) is right (left) handed. The readiest example is our two hands and some others are a wire helix, Mobius strip and irregular tetrahedron.

The interaction between an electromagnetic wave and chiral object can be such as to rotate the plane of the polarization of the wave to the right or left depending on the handedness of the objects. This is referred to as optical activity.

A linearly polarized wave incident on a chiral slab splits into two circularly polarized waves left and right with different phase velocities from each other. The two circularly polarized waves combine and a linearly polarized wave, whose plane of polarization is rotated with respect to plane of polarization of the incident plane wave, emerge behind the chiral slab. The amount of the rotation or attenuation depends on the distance travelled in the medium, and on the difference

between the two wave numbers which is an indication of degree of chirality given by ξ .

Chiral media have received considerable attention in recent years due to its potential applications in the fields of electromagnetic and microwave. It has been known as optical activity since the beginning of the nineteenth century. In 1811 Arago [1] discovered that the plane of polarization of linearly polarized light traversing a crystal of quartz was rotated by the crystal when the direction of propagation was along its optic axis.

The experiments of Biot [2]-[4] (from 1812 to 1838) on plates of quartz showed that : 1. The dependence of optical activity on the thickness of plate 2. The unequal rotations of the planes of polarization of light of different wavelengths and the absence of any optical activity when two plates of quartz of the same thickness but opposite handedness are used. In 1815 [5] Biot discovered that optical activity is not restricted to crystalline solids but also appears in certain liquids such as oils of turpentine and aqueous solutions of tartaric acid. These discoveries led to the fundamental problem of determining the basic cause of optical activity.

In 1822, Fresnel [6] showed that a ray of light travelling along the axis of a crystal of quartz is resolved into two circularly polarized rays of opposite handedness that travel with unequal phase velocities. He argued that the difference in two wave velocities is the cause of the optical activity. In 1848, Pasteur[7] postulated that optically active molecules are three-dimensional chiral figures, and the handedness of these molecules causes optical activity. Thus Pasteur introduced geometry into chemistry and originated the branch of chemistry called stereochemistry. More recently, in 1920 and 1922, Lindman [8],[9] devised a macroscopic model for the phenomenon by using microwaves instead of light, and wire spirals instead of chiral molecules. The validity of the model was verified a few years later by

Pickering [10]. By the end of the 19th century experimental and empirical facts on optical activity were well established and physicists had started to develop theories in order to explain the interaction of electromagnetic waves with chiral media.

BASSIRI et al. [11] analyzed the reflection from and transmission through a semi-infinite chiral medium by obtaining the Fresnel equations in terms of parallel and perpendicular polarized modes. The conditions are obtained for the total internal reflection of the incident wave from the interface and for the existence of the Brewster angle. The effects of the chirality on the polarization and the intensity of the reflected wave from the half space are illustrated by using Stokes parameters. The propagation of electromagnetic waves through an infinite slab of chiral medium is formulated for oblique incidence and solved analytically for the case of normal incidence.

JAGGARD et al. [12] investigated the electromagnetic properties of a structure that is both chiral and periodic using coupled-mode equations. The coupled mode equations derived from physical considerations. The coupled mode equations are used to examine bandgap structure and reflected and transmitted fields. Chirality is observed predominantly in transmission while periodicity is present in both reflection and transmission.

VIITANEN and LINDELL [13] found the solutions for the dispersion equation and for the eigenwaves for a uniaxial chiral medium. In the letter, the polarization properties of a transverse wave propagating through a uniaxial chiral slab are considered. The results give a simple possibility for constructing a polarization transformer for changing the polarization of a propagating plane wave.

GUIRE et al.[14] observed the well known phenomenon of optical rotation and dichroism that results from the handedness of certain molecules or polymers at micro – and millimeter – wave

frequencies by introducing a chiral microstructure in an ordinary dielectric material. The reflection properties of the metal-backed samples were measured with a free space system using a pair of spot focusing antennas and a vector network analyser. They concluded that chirality can be used as a sensitive parameter to control EM wave propagation characteristics in dielectric composites.

Cory and Rosenhouse [15] analysed the electromagnetic surface wave propagation along a chiral slab. It is found that for low chirality, the behaviour of the chiral slab is similar to that of a dielectric slab, for medium chirality, the waves are trapped inside the slab in two different modes, while for high chirality, they are trapped in a single mode only.

Kluszens and Newman [16] developed image theory for a chiral body over a perfect electric and magnetic conducting ground plane, using the chiral volume equivalence theorem and conventional image theory for electric and magnetic currents. It is shown that the image of the chiral body has the same material parameters as the original body, except that the chirality admittance of the image is the negative of the original.

Barsukov and Kiseleva [17] showed the existence of the surface electromagnetic waves on a plane boundary of an isotropic chiral dielectric. A dispersion equation for the surface waves is obtained together with its analytic solution. The ranges of parameters are found where the surface waves exist. In particular, the surface wave is shown to be possible if the permittivity of a chiral medium is positive. They also studied the energy of surface waves.

Hillion [18] presented the general form of electromagnetic plane waves propagating in a chiral medium and determined the electric and magnetic fields that they generate. As an illustration of these chiral plane waves, three particular problems reflection on a

perfectly conducting moving mirror, reflection and refraction on a dielectric interface between achiral and chiral media, diffraction by a perfectly conducting half plane are discussed.

Lekner [19] presented a review of the optical properties of the isotropic chiral media. The review includes discussion of wave propagation in chiral media, and derivation of the reflection and transmission amplitudes of an isotropic optically active medium. Boundary conditions and energy conservation relations are derived. For the chiral layer, simple formulae are given for the reflection and transmission coefficients at normal incidence, in the weak chirality limit, near the critical angles, and for a thin layer. Analytic expressions are given for all the reflection and transmission amplitudes in the general case.

1.2 Meander-line Polarizer

Circularly polarized waves are used for transmission of signals through the ionosphere, to reduce echo from rain, command guidance systems and for space telemetry applications of satellites. If the tip of the electric field vector traces out a circular locus in space then it is called a circular wave. Circularly polarized field consist of two orthogonal linearly polarized components with the same magnitude and time phase difference of odd multiples of 90° between them. The circularly polarized fields can be produced directly or from the linearly polarized fields.

A linearly polarized wave can be converted to circularly polarized wave by means of meander-line polarizer that provides a wide - band circular polarization and 90° phase difference in transmission between the two linear components. A linearly polarized wave incident on a meander-line polarizer can be considered as consisting of two equal orthogonal components that is parallel and perpendicular to the meander-line axis.

The first design of the meander-line polarizer was conceived at the Stanford Research Institute in 1966 and the computer program used in its design described in 1969.

Young et al.[20] carried out a theoretical analysis and discussion of experimental results of a meander-line polarizer. This polarizer was consisted of several printed circuit sheets with etched copper meander lines. The sheets were spaced about one quarter wavelength apart. It was observed that most of the dissipation loss occurred in the copper meander lines.

Montgomery [21] formulated the solution to the problem of scattering of a plane wave by an infinite periodic array of thin conductors on a dielectric. The solution to the unsymmetrical structure was given in order to include the effect of the single dielectric slab. The fields were expanded into set of Floquet modes inside and outside of the dielectric slab. An integral equation was obtained over a single unit cell by combining the orthogonality of the Floquet mode together with the boundary conditions. This integral equation was solved by using moment method. This formulation was valid for relatively thin dielectrics.

Levrel et al.[22] investigated the design of a meander line polarizer depends mainly on characterizing the admittance variation of an elementary sheet with respect to frequency and the constitutive dimensions for electric fields perpendicular and parallel to the line direction. They expanded the fields into Floquet modes in the air and dielectric regions. A periodic cell was chosen and divided into segments along x and y axis. The current over each segment was treated as an unknown. They stated the relative convergence problem whereby an improper ratio is chosen between the number of segments and the number of Floquet modes. The normalised susceptances and phase of the transmission coefficient were calculated as a function of frequency and constitutive parameters of the meander-line and

compared with the previous experimental data. They also studied the variations of the array's susceptances with respect to constitutive parameters in a wide range of frequencies.

Poey and Guige [23] studied the problem of determining the current distribution on a one dimensional infinite periodic structure. An infinite line of metallic meander was chosen for the periodic structure. The induced current distribution on the structure was obtained by means of the matrix inversion algorithm deduced from moment method for illuminated by plane wave of any incidence.

Chu and Lee [24] presented simple empirical formulas for parallel and perpendicular polarization susceptances for a meander-line grating plate. They investigated an analytical model in terms of E-type and H-type modes for the multilayered meanderline polarizer plate to analyse the transmission characteristics of the plane waves at normal and oblique incidence. The results were compared with previously published data in the literature. Thick meanderline polarizers can also be treated using this method.

Makino et al.[25] discussed the effect of the reflection from the meander-line circular polarizer on the axial ratio. They proposed a three-layered meander-line circular polarizer in which the first and third layers have identical meander lines and the second layer is a different meander line. The design method is presented so that a meander-line circular polarizer is constructed with smaller numbers and types of single -layer meander lines.

Uckun and Ege [26] considered the solution to the problem of scattering of a plane wave by an infinite periodic array of thick meander-line conductors on a dielectric sheet. Susceptance values are obtained for the perpendicular and parallel polarized plane wave excitation.

Wu [27] described a versatile meander line polarizer and demonstrated the arbitrary rotation of linear polarization. This polarizer consisted of eight-layer meander-line grids with rigid foam spacers between any two layers. It was shown that the field polarization rotation angle through this meander-line polarizer was twice the angle between the incident polarization and the polarizer grating lines.

Bhattacharyya et al.[28] presented analysis of a multilayered meander line polarizer. Using waveguide modal fields and Galerkin's method of moments, the equivalent susceptance of a meander line screen is determined. The equivalent susceptance includes the effect of the dielectric layers that are present in the close vicinity of the meander – line plane. The transmission matrix formulation then is invoked to find the transmission and reflection behaviour of a multilayered meander line structure. Numerical results for equivalent susceptance, return loss and axial ratio are found to compare with the measured data. Performance characteristics of a multilayered meander line polarizers are studied, and the results are presented.

In the analysis, the scattered transverse components of the electric and magnetic fields are expressed by a finite number of two dimensional Floquet modes in air and chiral regions within a unit cell [21]. The boundary conditions, combined with the orthogonality property of the Floquet modes over a single periodic unit cell leads to an integral equation for the unknown induced current density on the metallic part of the strips. This integral equation can be solved by using the moment method by expressing the unknown current density in terms of a set of basis functions with unknown coefficients . However, the meander-line scatterers are continuous along the x –axis the unknown current over each branch within a unit cell has been expanded into a set of pulse functions. Since the strips are narrow enough with respect to wavelength, the current component parallel to the width of the strip can be neglected. This

method of analysis for plane wave scattering problems from the two dimensional periodic arrays will clarify our problem.

In this study, a theoretical investigation of power reflection and transmission coefficient through the chiral slab (when meander-line is absent) and chiral slab with meander-line polarizer have been analysed for TE and TM wave excitations. The meander-line is considered to be thin and divided into five branches, three horizontal and two vertical. Two lower and one upper horizontal and two vertical branches are divided into specific number of segments within a unit cell.

Delihacioglu and Uckun [29] have presented some part of this study, the power reflection and transmission coefficients of chiral slabs without meander-line strips, in September, 1998.

1.3 Summary of Chapters

This chapter deals with the goal of the study as the analysis of the chiral slab and meander-line polarizer with chiral slab, gives a brief history of literature about the chiral medium and meander-line polarizer, also gives the reason for investigating the problem.

Chapter 2 deals with the analysis of the wave propagation in a chiral medium and the derivation of the modal fields for TE and TM wave incidences, for linearly polarized fields in air region and left and right circularly polarized fields in chiral region. The derivation of the power reflection and transmission coefficients for TM and TE incidences for a chiral slab (meander-line is absent) are given and the numerical results of chiral slab is presented in this chapter.

Chapter 3 is devoted to analysis of the meander-line polarizer with chiral slab. The scattered transverse electric and magnetic fields are expressed by a finite number of two dimensional Floquet modes

in air and chiral regions. The procedure to obtain an integral equation for the unknown current density induced on the conducting strips is revealed by using boundary conditions combined with the orthogonality property of the Floquet modes over a single periodic unit cell. This integral equation is solved by using the moment method by expressing the unknown current density in terms of a set of basis functions with unknown coefficients. The relations for the power reflection and transmission coefficients are obtained.

Chapter 4 deals with the calculation of the inner products for a unit cell of thin meander-line polarizer. This inner products are substituted into previously obtained matrix equation to get the current coefficients. After finding the elements of the impedance matrix and inverting the matrix, current coefficients are found. The numerical results of meander – line polarizer is also presented in this chapter.

Chapter 5 is devoted to the conclusions that are reached. It gives a brief summary of numerical results for the chiral slab and meander – line polarizer with chiral slab.

CHAPTER 2

ANALYSIS OF CHIRAL SLAB

2.1 Propagation of Wave in Chiral Medium

The isotropic, homogeneous, lossless and source free chiral medium can be described electromagnetically by the constitutive relations,

$$\vec{D} = \epsilon_c \vec{E} - j\xi \vec{B} \quad (2.1)$$

$$\vec{H} = -j\xi \vec{E} + \frac{1}{\mu_c} \vec{B} \quad (2.2)$$

where ϵ_c , μ_c and ξ are real constants and represent, respectively, permittivity, permeability and chirality admittance of the chiral medium. The magnitude of ξ is a measure of the degree of chirality while the sign of ξ specifies the medium handedness. When $\xi > 0$ the medium is a right handed and the sense of polarization is right handed, when $\xi < 0$, the medium is left handed and the sense of polarization is left handed; and when $\xi = 0$ the medium reduces to ordinary dielectric and there is no optical activity.

The displacement vector D and the magnetic field H inside a chiral medium depends on both E and B . In order to explain the dependence, assume a short metallic helix as a chiral object in a dielectric medium, the incident electric field induces currents in the straight portion of the chiral object, and by continuity these currents must also flow in the circular portion of the object. The current in the straight portion contributes to the electric dipole moment of the object and the current in the circular portion contributes to its

magnetic dipole moment. In a complementary manner, the incident magnetic field induces currents in the circular portion and by continuity in the straight portions. Thus, also the magnetic field contributes to the electric and magnetic dipole moments of the object.

On the other hand, the time harmonic Maxwell's equations for a source free region and an $e^{j\omega t}$ time suppression can be written as ,

$$\vec{\nabla} \times \vec{E} = -j\omega \vec{B} \quad (2.3a)$$

$$\vec{\nabla} \times \vec{H} = j\omega \vec{D} \quad (2.3b)$$

$$\vec{\nabla} \cdot \vec{D} = 0 \quad (2.3c)$$

$$\vec{\nabla} \cdot \vec{B} = 0 \quad (2.3d)$$

substituting eq. (2.1) into (2.3b) and eq. (2.2) into (2.3a) we obtain,

$$\vec{\nabla} \times \vec{H} = j\omega(\epsilon_c + \mu_c \xi^2) \vec{E} + \omega \mu_c \xi \vec{H} \quad (2.4)$$

$$\vec{\nabla} \times \vec{E} = -j\omega \mu_c \vec{H} + \omega \mu_c \xi \vec{E} \quad (2.5)$$

taking the curl of equations (2.4) and (2.5) one can obtain the chiral Helmholtz equation as,

$$\nabla \times \nabla \times \vec{H} - 2\omega \mu_c \xi \nabla \times \vec{H} - \omega^2 \mu_c \epsilon_c \vec{H} = 0 \quad (2.6)$$

$$\nabla \times \nabla \times \vec{E} - 2\omega \mu_c \xi \nabla \times \vec{E} - \omega^2 \mu_c \epsilon_c \vec{E} = 0 \quad (2.7)$$

From this equation it is found that propagating eigenmodes within such media consists of two circularly polarized waves with characteristic wave numbers,

$$k_R = \frac{2\pi}{\lambda_R} = \omega \mu_c \xi + \sqrt{\omega^2 \mu_c \epsilon_c + (\omega \mu_c \xi)^2} \quad (2.8)$$

$$k_L = \frac{2\pi}{\lambda_L} = -\omega \mu_c \xi + \sqrt{\omega^2 \mu_c \epsilon_c + (\omega \mu_c \xi)^2} \quad (2.9)$$

where k_L and k_R are real quantities for propagating waves. Hence the chiral medium allows double mode propagation; left circularly polarized (LCP) and right circularly polarized (RCP) wave. This is called polarization birefringence. The LCP and RCP waves propagate with different phase velocities $v_L = \omega/k_L$ and $v_R = \omega/k_R$ respectively. As a result, a linearly polarized wave cannot traverse this medium without changing its polarization giving rise to optical activity. A purely imaginary values of k_L and k_R corresponds to a decaying (evanescent) wave. This causes an attenuation and referred to as circular dichroism. Circular dichroism refers to a change of the polarization ellipticity of waves by the medium. In an isotropic chiral slab, a linearly polarized wave is divided into LCP and RCP waves with unequal attenuation and an elliptically polarized wave appears behind the chiral slab as a combination of the two circularly polarized waves.

2.2 Modal Fields in Air and Chiral Mediums

For a linearly polarized plane wave propagating in \vec{a}_r direction as shown in Figure 2.1 we can write,

$$\vec{E} = (E_\theta \vec{a}_\theta + E_\phi \vec{a}_\phi) e^{-jk\vec{a}_r \cdot \vec{r}} \quad (2.10)$$

where \vec{a}_r is the unit vector showing the direction of propagation and we assume that E_θ and E_ϕ are real values.

$$\vec{E} = E_\theta \vec{a}_\theta e^{-jk\vec{a}_r \cdot \vec{r}} + E_\phi \vec{a}_\phi e^{-jk\vec{a}_r \cdot \vec{r}}$$

both terms still represent a linearly polarized plane wave propagating in \vec{a}_r direction.

$$\vec{E}_1 = E_\theta \vec{a}_\theta e^{-jk\vec{a}_r \cdot \vec{r}} = E_\theta (\cos\theta \cos\phi \vec{a}_x + \cos\theta \sin\phi \vec{a}_y - \vec{a}_z \sin\theta) e^{-jk\vec{a}_r \cdot \vec{r}} \quad (2.11)$$

$$\vec{E}_2 = E_\phi \vec{a}_\phi e^{-jk\vec{a}_r \cdot \vec{r}} = E_\phi (-\sin\phi \vec{a}_x + \cos\phi \vec{a}_y) e^{-jk\vec{a}_r \cdot \vec{r}} \quad (2.12)$$

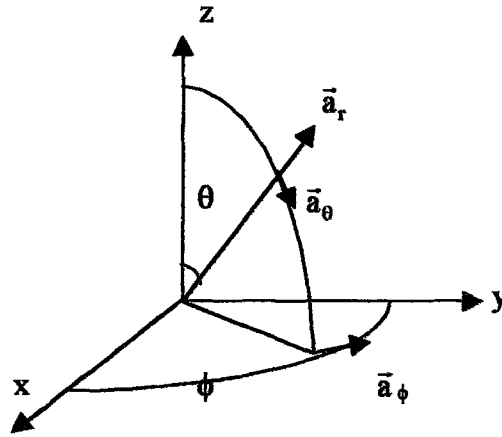


Fig. 2.1 Wave Propagation in \vec{a}_r direction

where $\vec{r} = x\vec{a}_x + y\vec{a}_y + z\vec{a}_z$ is the position vector, θ is the polar angle and ϕ is the azimuth angle.

The plane wave \vec{E}_2 has no z component so it represents a TE_z wave whereas the magnetic field component associated with \vec{E}_1 has no z component and so it is called TM_z wave.

2.2.1 Modal Field for TM Incident Wave

The electric and magnetic field vectors in air region for a TM wave can be written as,

$$\vec{E}^{TM} = E_0 \vec{a}_\theta e^{-jk_0 \vec{a}_r \cdot \vec{r}} \quad (2.13)$$

$$\vec{H}^{TM} = \frac{k_0}{\omega \mu_0} E_0 \vec{a}_\phi e^{-jk_0 \vec{a}_r \cdot \vec{r}} \quad (2.14)$$

where, E_0 is the amplitude of the incident TM wave.

Arranging the equations (2.13) and (2.14) in cartesian coordinate system the electric field and the corresponding magnetic field can be written as,

$$\vec{E}^{TM} = E_o \frac{\gamma}{k_o} \left(\frac{\vec{k}_T}{|\vec{k}_T|} - \frac{k_o}{\gamma} |\vec{k}_T| \cdot \vec{a}_z \right) e^{-j\vec{k}_T \cdot \vec{r}_T} e^{-j\gamma z} \quad (2.15)$$

$$\vec{H}^{TM} = E_o \frac{\gamma}{k_o} \vec{a}_z \times \frac{\vec{k}_T}{|\vec{k}_T|} e^{-j\vec{k}_T \cdot \vec{r}_T} e^{-j\gamma z} \quad (2.16)$$

where, $\vec{k}_T = \vec{a}_x k_o \cos\phi \sin\theta + \vec{a}_y k_o \cos\theta \sin\phi$, $\vec{r}_T = x \vec{a}_x + y \vec{a}_y$,

$$\gamma = \sqrt{k_o^2 - |\vec{k}_T|^2}, \quad k_o = \omega \sqrt{\mu_o \epsilon_o}$$

The transverse components of the fields can be written as ,

$$\vec{E}^{TM} = E_o^{TM} \vec{\Psi}_{TM} e^{-j\gamma z} \quad (2.17)$$

$$\vec{H}^{TM} = \vec{a}_z \times Y^{TM} E_o^{TM} \vec{\Psi}_{TM} e^{-j\gamma z} \quad (2.18)$$

where

$$E_o^{TM} = E_o \frac{\gamma}{k_o}, \quad \vec{\Psi}_{TM} = \vec{e}_{TM} e^{-j\vec{k}_T \cdot \vec{r}_T}, \quad Y^{TM} = Y \frac{k_o}{\gamma}, \quad Y = \sqrt{\frac{\mu_o}{\epsilon_o}}$$

$$\vec{e}_{TM} = \frac{\vec{k}_T}{|\vec{k}_T|} = \vec{a}_x \cos\phi + \vec{a}_y \sin\phi$$

2.2.2 Modal Field for TE Incident Wave

The electric and magnetic field vector in air region for a TE wave can be written as,

$$\vec{E}^{TE} = E_o \vec{a}_\phi e^{-jk_o \vec{a}_r \cdot \vec{r}} \quad (2.19)$$

$$\vec{H}^{TE} = \frac{k_o}{\omega \mu_o} E_o \vec{a}_\theta e^{-jk_o \vec{a}_r \cdot \vec{r}} \quad (2.20)$$

arranging the equations (2.19) and (2.20) in cartesian coordinate system the electric and magnetic fields can be written as,

$$\vec{E}^{TE} = E_0 \left(\vec{a}_z \times \frac{\vec{k}_T}{|\vec{k}_T|} \right) e^{-j\vec{k}_T \cdot \vec{r}_T} e^{-j\gamma z} \quad (2.21)$$

$$\vec{H}^{TE} = E_0 \frac{\gamma}{k_0} \left(\vec{a}_z \times \vec{a}_z \times \frac{\vec{k}_T}{|\vec{k}_T|} + \frac{k_0}{\gamma} \frac{\vec{k}_T}{|\vec{k}_T|} \vec{a}_z \right) e^{-j\vec{k}_T \cdot \vec{r}_T} e^{-j\gamma z} \quad (2.22)$$

the transverse components of the electric and magnetic fields can be written as,

$$\vec{E}^{TE} = E_0^{TE} \vec{\Psi}_{TE} e^{-j\gamma z} \quad (2.23)$$

$$\vec{H}^{TE} = \vec{a}_z \times Y^{TE} E_0^{TE} \vec{\Psi}_{TE} e^{-j\gamma z} \quad (2.24)$$

where $E_0^{TE} = E_0$, $\vec{\Psi}_{TE} = \vec{e}_{TE} e^{-j\vec{k}_T \cdot \vec{r}_T}$,

$$\vec{e}_{TE} = \vec{a}_z \times \frac{\vec{k}_T}{|\vec{k}_T|} = -\vec{a}_x \sin\phi + \vec{a}_y \cos\phi, \quad Y^{TE} = Y \frac{\gamma}{k_0}$$

2.2.3 Modal Field for LCP Wave

A left circularly polarized wave travelling in a homogeneous, isotropic, lossless chiral medium can be written in the following form,

$$\vec{E}_{LCP} = E_L (\vec{a}_\theta + j \vec{a}_\phi) e^{-jk_L \vec{a}_r \cdot \vec{r}} \quad (2.25)$$

the corresponding magnetic field can be found from the equation,

$$\vec{H} = \frac{-1}{j\omega\mu_c} (\nabla \times \vec{E} - \omega\mu_c \xi \vec{E}) \quad (2.26)$$

from equations (2.25) and (2.26) by using the cartesian coordinate system, one can obtain the transverse components of the electric and magnetic fields,

$$\vec{E}_{LCP} = (E_L^{TM} \vec{e}_{TM} + j E_L^{TE} \vec{e}_{TE}) e^{-j\vec{k}_T \cdot \vec{r}_T} e^{-j\gamma_L z} \quad (2.27)$$

$$\vec{H}_{LCP} = \vec{a}_z \times (Y_L^{TM} E_L^{TM} \vec{e}_{TM} + jY_L^{TE} E_L^{TE} \vec{e}_{TE}) e^{-j\vec{k}_T \cdot \vec{r}_T} e^{-j\gamma_L z} \quad (2.28)$$

where,

$$E_L^{TM} = E_L \frac{\gamma_L}{k_L}, \quad E_L^{TE} = E_L, \quad Y_L^{TM} = Y_c \frac{k_L}{\gamma_L}, \quad Y_L^{TE} = Y_c \frac{\gamma_L}{k_L}$$

$$Y_c = \frac{k_c}{\omega \mu_c}, \quad k_c = \sqrt{\omega^2 \mu_c \epsilon_c + (\omega \mu_c \xi)^2}, \quad \gamma_L = \sqrt{k_L^2 - |\vec{k}_T|^2}$$

2.2.4 Modal Field for RCP Wave

A right circularly polarized wave travelling in a homogeneous, isotropic, lossless chiral medium can be written in the following form ,

$$\vec{E}_{RCP} = E_R (\vec{a}_\theta - j \vec{a}_\phi) e^{-j\vec{k}_R \cdot \vec{r}_R} \quad (2.29)$$

the corresponding magnetic field can be obtained from equation (2.26). From equations (2.26) and (2.29) by using the cartesian coordinate system, one can obtain the transverse components of the electric and magnetic fields ,

$$\vec{E}_{RCP} = (E_R^{TM} \vec{e}_{TM} - jE_R^{TE} \vec{e}_{TE}) e^{-j\vec{k}_T \cdot \vec{r}_T} e^{-j\gamma_R z} \quad (2.30)$$

$$\vec{H}_{RCP} = \vec{a}_z \times (Y_R^{TM} E_R^{TM} \vec{e}_{TM} - jY_R^{TE} E_R^{TE} \vec{e}_{TE}) e^{-j\vec{k}_T \cdot \vec{r}_T} e^{-j\gamma_R z} \quad (2.31)$$

where $E_R^{TE} = E_R$, $E_R^{TM} = E_R \frac{\gamma_R}{k_R}$

$$Y_R^{TM} = Y_c \frac{k_R}{\gamma_R}, \quad Y_R^{TE} = Y_c \frac{\gamma_R}{k_R}, \quad \gamma_R = \sqrt{k_R^2 - |\vec{k}_T|^2}$$

2.3 Power Reflection and Transmission Coefficient for a Chiral Slab (TM Incidence)

The transverse component of the electric and magnetic fields for TM incidence in air region can be written as,

$$\vec{E}_{\text{inc}} = E_0^{\text{TM}} \vec{\Psi}_1 e^{-j\gamma z} \quad (2.32a)$$

$$\vec{H}_{\text{inc}} = \vec{a}_z \times Y^{(1)} E_0^{\text{TM}} \vec{\Psi}_1 e^{-j\gamma z} \quad (2.32b)$$

where E_0^{TM} is the amplitude of the TM incident wave. Since left and right circularly polarized waves travel in the chiral medium we can assume that a reflected and transmitted TE waves exist in the air regions, in addition to the reflected and transmitted TM waves. Thus for the reflected wave we can write,

$$\vec{E}_r = \sum_{m=1}^2 j^{m-1} E_r^{(m)} \vec{\Psi}_m e^{j\gamma z} \quad (2.33a)$$

$$\vec{H}_r = -\vec{a}_z \times \sum_{m=1}^2 j^{m-1} Y_r^{(m)} E_r^{(m)} \vec{\Psi}_m e^{j\gamma z} \quad (2.33b)$$

where $m=1$ for TM modes and $m=2$ for TE modes. Inside the chiral slab ($0 < z < d$), fields propagating in $+z$ direction ,

$$\vec{E}_c^+ = \sum_{m=1}^2 j^{m-1} (A_L^{(m)} e^{-j\gamma_L z} + (-1)^{m-1} A_R^{(m)} e^{-j\gamma_R z}) \vec{\Psi}_m \quad (2.34)$$

$$\vec{H}_c^+ = -\vec{a}_z \times \sum_{m=1}^2 j^{m-1} (Y_L^{(m)} A_L^{(m)} e^{-j\gamma_L z} + (-1)^{m-1} Y_R^{(m)} A_R^{(m)} e^{-j\gamma_R z}) \vec{\Psi}_m \quad (2.35)$$

Fields propagating in $-z$ direction,

$$\vec{E}_c^- = \sum_{m=1}^2 (-j)^{m-1} (B_L^{(m)} e^{j\gamma_L z} + (-1)^{m-1} B_R^{(m)} e^{j\gamma_R z}) \vec{\Psi}_m \quad (2.36)$$

$$\vec{H}_c^- = -\vec{a}_z \times \sum_{m=1}^2 (-j)^{m-1} (Y_L^{(m)} B_L^{(m)} e^{j\gamma_L z} + (-1)^{m-1} Y_R^{(m)} B_R^{(m)} e^{j\gamma_R z}) \vec{\Psi}_m \quad (2.37)$$

Transmitted fields for $z > d$,

$$\vec{E}_t = \sum_{m=1}^2 j^{m-1} E_t^{(m)} \vec{\Psi}_m e^{-j\gamma(z-d)} \quad (2.38a)$$

$$\bar{H}_1 = \bar{a}_z \times \sum_{m=1}^2 j^{m-1} Y^{(m)} E_1^{(m)} \bar{\Psi}_m e^{-j\gamma(z-d)} \quad (2.38b)$$

where $\bar{\Psi}_m = e^{-jk_T \bar{r}_T} \bar{e}_m$,

$$\bar{e}_1 = \frac{\bar{k}_T}{|\bar{k}_T|} \quad m=1 \text{ for TM modes,}$$

$$\bar{e}_2 = \bar{a}_z \times \bar{e}_1 \quad m=2 \text{ for TE modes,}$$

$$A_{L,R}^{(m)} = \left(\frac{Y_c}{Y_{L,R}^{(1)}} \right)^{2-m} A_{L,R}, \quad B_{L,R}^{(m)} = \left(\frac{Y_c}{Y_{L,R}^{(1)}} \right)^{2-m} B_{L,R}$$

$$Y_{L,R}^{(1)} = Y_c \frac{k_{L,R}}{\gamma_{L,R}}, \quad Y_{L,R}^{(2)} = Y_c \frac{\gamma_{L,R}}{k_{L,R}}, \quad k_c = \sqrt{\omega^2 \mu_c \epsilon_c + (\omega \mu_c \xi)^2}$$

$$Y^{(1)} = Y \frac{k}{\gamma}, \quad Y^{(2)} = Y \frac{\gamma}{k}, \quad Y_c = \frac{k_c}{\omega \mu_c}, \quad k = \omega \sqrt{\mu_c \epsilon_c}$$

$$\gamma = \left\{ \begin{array}{l} \sqrt{k^2 - |k_T|^2} \\ -j\sqrt{|k_T|^2 - k^2} \end{array} \right\} \quad \left. \begin{array}{l} k^2 > |k_T|^2 \\ k^2 < |k_T|^2 \end{array} \right\}$$

$$\gamma_{L,R} = \left\{ \begin{array}{l} \sqrt{k_{L,R}^2 - |k_T|^2} \\ -j\sqrt{|k_T|^2 - k_{L,R}^2} \end{array} \right\} \quad \left. \begin{array}{l} k_{L,R}^2 > |k_T|^2 \\ k_{L,R}^2 < |k_T|^2 \end{array} \right\}$$

Matching the tangential electric and magnetic fields at the boundaries at $z=0$ and $z=d$, since at the boundary transverse components of the electric and magnetic fields are continuous, then the modal coefficients of the reflected and transmitted fields can be obtained in terms of the incident field.

$$E_{\text{rom}}^{\text{TM}} = A_L^{(m)} + (-1)^{m-1} A_R^{(m)} + (-1)^{m-1} B_L^{(m)} + B_R^{(m)} + (m-2)E_0^{\text{TM}} \quad (2.39)$$

$$E_{\text{tot}}^{\text{TM}} = A_L^{(m)} e^{-j\gamma_L d} + (-1)^{m-1} A_R^{(m)} e^{-j\gamma_R d} + (-1)^{m-1} B_L^{(m)} e^{j\gamma_L d} + B_R^{(m)} e^{j\gamma_R d} \quad (2.40)$$

where superscript TM represents the TM excitation, subscript r and t represent the reflected and transmitted fields, subscript o represent the chiral slab without meander-line polarizer, subscript m represents TM or TE modes and

$$\begin{bmatrix} B_L \\ B_R \end{bmatrix} = \begin{bmatrix} r_{LL} & r_{LR} \\ r_{RL} & r_{RR} \end{bmatrix} \begin{bmatrix} A_L \\ A_R \end{bmatrix}, \quad \begin{bmatrix} A_L \\ A_R \end{bmatrix} = \frac{1}{\Delta A} \begin{bmatrix} A_{11} & A_{12} \\ A_{21} & A_{22} \end{bmatrix} \begin{bmatrix} 2Y^{(1)}E_o^{\text{TM}} \\ 0 \end{bmatrix}$$

$$r_{LL} = \frac{1}{\Delta I} (S_1 + S_2) e^{-2j\gamma_L d}, \quad r_{RR} = \frac{1}{\Delta I} (S_2 - S_1) e^{-2j\gamma_R d}$$

$$r_{LR} = \frac{2Y_R^{(2)}(Y^2 - Y_c^2)}{\Delta I} e^{-j(\gamma_L + \gamma_R)d}, \quad r_{RL} = \frac{2Y_L^{(2)}(Y^2 - Y_c^2)}{\Delta I} e^{-j(\gamma_L + \gamma_R)d}$$

$$\Delta I = Y_L^{(2)}(Y^{(2)} + Y_R^{(2)})(Y^{(1)} + Y_L^{(1)}) + Y_R^{(2)}(Y^{(2)} + Y_L^{(2)})(Y^{(1)} + Y_R^{(1)})$$

$$S_1 = (Y^2 + Y_c^2)(Y_R^{(2)} - Y_L^{(2)}), \quad S_2 = 2Y_R^{(2)}(Y_R^{(1)}Y^{(2)} - Y_L^{(2)}Y^{(1)})$$

$$A_{11} = Y_L^{(2)}(Y^{(1)} + Y_L^{(1)}) + Y_L^{(2)}(Y^{(1)} - Y_L^{(1)})r_{LL} + Y_R^{(2)}(Y^{(1)} - Y_R^{(1)})r_{RL}$$

$$A_{12} = Y_R^{(2)}(Y^{(1)} + Y_R^{(1)}) + Y_L^{(2)}(Y^{(1)} - Y_L^{(1)})r_{LR} + Y_R^{(2)}(Y^{(1)} - Y_R^{(1)})r_{RR}$$

$$A_{21} = (Y^{(2)} + Y_L^{(2)}) - (Y^{(2)} - Y_L^{(2)})r_{LL} + (Y^{(2)} - Y_R^{(2)})r_{RL}$$

$$A_{22} = (Y^{(2)} + Y_R^{(2)}) + (Y^{(2)} - Y_L^{(2)})r_{LR} - (Y^{(2)} - Y_R^{(2)})r_{RR}$$

$$\Delta A = A_{11}A_{22} - A_{21}A_{12}$$

2.4 Power Reflection and Transmission Coefficients for a Chiral Slab (TE incidence)

The transverse component of the electric and magnetic fields for TE incidence in air region can be written as,

$$\vec{E}_{inc} = E_0^{TE} \vec{\Psi}_1 e^{-j\gamma z} \quad (2.41a)$$

$$\vec{H}_{inc} = \vec{a}_z \times Y^{(1)} E_0^{TE} \vec{\Psi}_1 e^{-j\gamma z} \quad (2.41b)$$

where E_0^{TE} is the amplitude of the incident TE wave. The TM waves exist in the air regions in addition to the TE waves, so the reflected electric and magnetic fields are,

$$\vec{E}_r = \sum_{i=1}^2 j^{i-1} E_r^{(i)} \vec{\Psi}_i e^{j\gamma z} \quad (2.42a)$$

$$\vec{H}_r = -\vec{a}_z \times \sum_{i=1}^2 j^{i-1} Y^{(i)} E_r^{(i)} \vec{\Psi}_i e^{j\gamma z} \quad (2.42b)$$

where $i=1$ for TE modes and $i=2$ for TM modes. Inside the chiral slab ($0 < z < d$), fields propagating in $+z$ direction,

$$\vec{E}_c^+ = \sum_{i=1}^2 j^{i-1} [(-1)^i C_L^{(i)} e^{-j\gamma_L z} + C_R^{(i)} e^{-j\gamma_R z}] \vec{\Psi}_i \quad (2.43a)$$

$$\vec{H}_c^+ = -\vec{a}_z \times \sum_{i=1}^2 j^{i-1} [(-1)^i Y_L^{(i)} C_L^{(i)} e^{-j\gamma_L z} + Y_R^{(i)} C_R^{(i)} e^{-j\gamma_R z}] \vec{\Psi}_i \quad (2.43b)$$

Fields propagating in $-z$ direction,

$$\vec{E}_c^- = \sum_{i=1}^2 (-j)^{1-i} [-D_L^{(i)} e^{j\gamma_L z} + (-1)^{1-i} D_R^{(i)} e^{j\gamma_R z}] \vec{\Psi}_i \quad (2.44a)$$

$$\vec{H}_c^- = -\vec{a}_z \times \sum_{i=1}^2 (-j)^{1-i} [-Y_L^{(i)} D_L^{(i)} e^{j\gamma_L z} + (-1)^{1-i} Y_R^{(i)} D_R^{(i)} e^{j\gamma_R z}] \vec{\Psi}_i \quad (2.44b)$$

Transmitted fields for $z > d$,

$$\vec{E}_t = \sum_{i=1}^2 j^{i-1} E_t^{(i)} \vec{\Psi}_i e^{-j\gamma(z-d)} \quad (2.45a)$$

$$\vec{H}_t = \vec{a}_z \times \sum_{i=1}^2 j^{i-1} Y^{(i)} E_t^{(i)} \vec{\Psi}_i e^{-j\gamma(z-d)} \quad (2.45b)$$

where $\vec{\Psi}_i = e^{-jk_T \cdot \vec{r}_T} \vec{e}_i$, $i=1,2$.

$$\vec{e}_1 = \vec{a}_z \times \vec{e}_2 \quad i=1 \quad \text{for TE modes}$$

$$\vec{e}_2 = \frac{\vec{k}_T}{|\vec{k}_T|} \quad i=2 \quad \text{for TM modes}$$

Matching the tangential electric and magnetic fields at the boundaries at $z=0$ and $z=d$ the modal coefficients of the reflected and transmitted fields can be obtained in terms of the incident field.

$$E_{\text{toi}}^{\text{TE}} = (-1)^i C_L^{(i)} + C_R^{(i)} - D_L^{(i)} + (-1)^{i-1} D_R^{(i)} + (i-2)E_o^{\text{TE}} \quad (2.46)$$

$$E_{\text{toi}}^{\text{TE}} = (-1)^i C_L^{(i)} e^{-j\gamma_L d} + C_R^{(i)} e^{-j\gamma_R d} - D_L^{(i)} e^{j\gamma_L d} + (-1)^{i-1} D_R^{(i)} e^{j\gamma_R d} \quad (2.47)$$

where superscript TE represents the TE wave excitation, subscript r and t represent the reflected and transmitted fields, subscript o represent the chiral slab without meander-line polarizer, subscript i represents TE or TM modes and

$$\begin{bmatrix} D_L \\ D_R \end{bmatrix} = \begin{bmatrix} m_{LL} & m_{LR} \\ m_{RL} & m_{RR} \end{bmatrix} \begin{bmatrix} C_L \\ C_R \end{bmatrix}, \quad \begin{bmatrix} C_L \\ C_R \end{bmatrix} = \frac{1}{\Delta B} \begin{bmatrix} B_{11} & B_{12} \\ B_{21} & B_{22} \end{bmatrix} \begin{bmatrix} 2Y^{(1)}E_o^{\text{TE}} \\ 0 \end{bmatrix}$$

$$m_{LL} = \frac{1}{\Delta 2} (S_1 + S_2) e^{-2j\gamma_L d}, \quad m_{RR} = \frac{1}{\Delta 2} (S_2 - S_1) e^{-2j\gamma_R d}$$

$$m_{RL} = \frac{2Y_R^{(2)}(Y^2 - Y_c^2)}{\Delta 2} e^{-j(\gamma_L + \gamma_R)d}, \quad m_{LR} = \frac{2Y_L^{(2)}(Y^2 - Y_c^2)}{\Delta 2} e^{-j(\gamma_L + \gamma_R)d}$$

$$\Delta 2 = Y_L^{(1)}(Y^{(1)} + Y_R^{(1)})(Y^{(2)} + Y_L^{(2)}) + Y_R^{(1)}(Y^{(1)} + Y_L^{(1)})(Y^{(2)} + Y_R^{(2)})$$

$$S_1 = (Y^2 + Y_c^2)(Y_R^{(2)} - Y_L^{(2)}), \quad S_2 = 2Y_R^{(2)}(Y_R^{(1)}Y^{(2)} - Y_L^{(2)}Y^{(1)})$$

$$B_{11} = (Y^{(1)} + Y_L^{(1)}) + (Y^{(1)} - Y_L^{(1)})F_{LL} - (Y^{(1)} - Y_R^{(1)})F_{RL}$$

$$B_{12} = (Y^{(1)} + Y_R^{(1)}) - (Y^{(1)} - Y_L^{(1)})F_{LR} + (Y^{(1)} - Y_R^{(1)})F_{RR}$$

$$B_{21} = Y_L^{(1)}(Y^{(2)} + Y_L^{(2)}) - Y_L^{(1)}(Y^{(2)} - Y_L^{(2)})F_{LL} + Y_R^{(1)}(Y^{(2)} - Y_R^{(2)})F_{RL}$$

$$B_{22} = Y_R^{(1)}(Y^{(2)} + Y_R^{(2)}) + Y_L^{(1)}(Y^{(2)} - Y_L^{(2)})F_{LR} - Y_R^{(1)}(Y^{(2)} - Y_R^{(2)})F_{RR}$$

$$\Delta B = B_{11}B_{22} - B_{21}B_{12}$$

2.5 Numerical Results of the Chiral Slab

In this section, the numerical results of the power reflection and transmission characteristic of the chiral slab are presented. The effects of chirality admittance, slab thickness and relative permittivity of chiral slab are analyzed for both TM and TE polarization of the incident field and plotted with respect to frequency and incidence angle.

The power reflection and transmission coefficients are plotted with respect to frequency in Figures 2.2 to 2.4 and the chiral slab is excited by a normally incident plane wave of either TE or TM polarization. For Figures 2.5 to 2.7 and Figures 2.8 to 2.10 the chiral slab is excited by normal incidence of TM and TE polarizations, respectively. For Figures 2.5 to 2.10 the power reflection and transmission coefficients are plotted with respect to incidence angle theta and for these figures frequency is taken as 12 Ghz. For all figures it is assumed that $\mu = \mu_0$. For normal incidence the cross-polar power reflection coefficient is zero for both types of plane wave incidences, TM and TE polarization; that is why they are not plotted. During the study it was observed that both reflection and transmission coefficients were not affected for the variation of the azimuth angle ϕ . Therefore the variation of the ϕ values are not plotted and ϕ is assumed to be equal to zero for all plotted figures.

The plotted values of power reflection and transmission coefficients in all figures have been normalised with respect to the incident power. The results have been seen to be in good agreement

with the energy conservation law. The summation of co – and cross – polar power reflection and transmission coefficient amplitudes are equal to unity. That is;

$$(E_r^{(1)})^2 + \left(\frac{E_r^{(2)}}{\cos\theta}\right)^2 + (E_t^{(1)})^2 + \left(\frac{E_t^{(2)}}{\cos\theta}\right)^2 = 1$$

for TE incidence where $E_r^{(1)}$ and $E_t^{(1)}$ are co – polar TE, $E_r^{(2)}$ and $E_t^{(2)}$ are the cross – polar TM component electric fields, respectively. Similar equation can be written for TM incident wave as,

$$(E_r^{TM})^2 + (E_r^{TE} \cos\theta)^2 + (E_t^{TM})^2 + (E_t^{TE} \cos\theta)^2 = 1.$$

It has also been seen that for normal incidence of either TE or TM incident plane wave, the power reflection and transmission coefficients are the same as given by Lakhtakia et al.[30], for that reason it is only plotted for TE polarization of the incident plane wave. At the beginning, it is assumed that the chiral medium has the following parameters for Figures 2.2 to 2.4; $\xi=0.003$ S, slab thickness $d=6.25$ mm and relative permittivity of $\epsilon_r=2.0$. As shown in Fig.2.2 four different values of the chirality admittance are chosen $\xi=0$ (dielectric), $\xi=0.001$ S, $\xi=0.002$ S, and $\xi=0.003$ S by considering the bound for the chirality admittance; $0 \leq \xi \leq \sqrt{\frac{\epsilon_c}{\mu_c}}$ as given in [31].

The power reflection and transmission coefficients against frequency for different values of chirality admittance are shown in Figure 2.2. As it can be seen from the figure, the presence of the handedness strongly alters the power reflection and transmission characteristics. The peak value of the computed power reflection coefficient is less in the absence of chirality. The amplitude of the cross-polar power transmission coefficients are equal to zero for $\xi=0$.

As the chirality admittance increases the peak value of the co – polar power reflection coefficient also increases and shifts to lower frequencies with narrowing bandwidth. The co – polar power transmission coefficient is zero for $\xi=0.002$ S, and $\xi =0.003$ S at frequency of 16 and 11 Ghz, respectively. It is unity at 1 Ghz and 17 Ghz for $\xi=0$. As shown in Fig. 2.2.c, full transmission is observed for the cross – polar power transmission coefficient at the frequency of close to 15 Ghz for $\xi=0.002$ S. The amplitude of the cross – polar power transmission coefficient is reduced to zero around 21 Ghz for $\xi=0.003$.

The peak magnitude of the co – polar power reflection coefficient is not affected from the variation of the slab thickness as shown in Figure 2.3. More peaks appear with the same amplitude and narrow bandwidth is observed for $d=12.5$ mm. As slab thickness increases, the co– and cross–polar power transmission coefficients shift to lower frequencies with narrow bandwidth and two peaks with different amplitudes are observed for $d=12.5$ mm for the range of 1 to 25 Ghz.

The power reflection and transmission coefficients against frequency for different dielectric constants of the chiral slab are shown in Figure 2.4. If dielectric constant increases the co – polar power reflection coefficient also increases. More peaks are observed with the same amplitude as ϵ_r increases. The co – polar power transmission coefficient is zero at 10.5 Ghz even if the dielectric constant changes and unity at 20.5 Ghz for $\epsilon_r=4.0$. Full transmission is also obtained for the cross – polar power transmission coefficient for the value of $\epsilon_r=4.0$ at 10.5 Ghz and is zero at 20.5 Ghz for all ϵ_r values as shown in Figure 2.4.c. Two peaks with different amplitudes are also observed for the value of $\epsilon_r=9.0$ at the frequency range of 1 to 25 Ghz.

There is a Brewster angle for TM polarization of the incident plane wave as shown in Figure 2.5.a. As ξ increases the Brewster angle approaches 90° with narrowing bandwidth up to value of $\xi=0.003$ S. After the Brewster angle the power reflection coefficient sharply increases and reaches unity for different values of chirality admittance. The co – polar power transmission coefficient is unity at $\theta=69^\circ$ for $\xi=0$ and the magnitude decreases shifting to right side with narrowing bandwidth as chirality admittance increases up to value of $\xi=0.003$ S. For $\xi=0.006$ S the co – polar power transmission coefficient increases. The cross – polar power transmission coefficient increases as chirality admittance increases from $\xi=0$ to $\xi=0.003$ S and then decreases for the value of $\xi=0.006$ S.

The power reflection and transmission coefficients against incident angle θ for different slab thickness are shown Figure 2.6. When $d=3.125$ mm ($\lambda/8$) there is no Brewster angle and the co – polar power transmission coefficient is nearly zero whereas the cross – polar power transmission coefficient is much greater. When $d=6.25$ mm ($\lambda/4$) and $d=12.5$ mm ($\lambda/2$) there is a Brewster angle at $\theta=75^\circ$ and cross – polar power transmission coefficient is close to zero for both values of slab thickness. Therefore the co – polar power transmission coefficient is unity at the Brewster angle as shown in Figure 2.5.b.

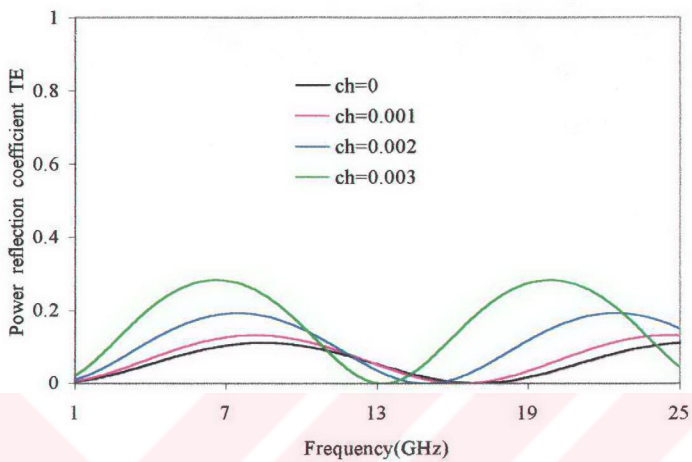
The power reflection and transmission coefficients against incident angle θ for different dielectric constants of the chiral slab are shown in Figure 2.7. If dielectric constant increases from $\epsilon_r=8$ to $\epsilon_r=11$ the magnitude of co – polar power reflection coefficient decreases up to Brewster angle at $\theta=75^\circ$ and from that point it sharply increases to unity at $\theta=90^\circ$. The variation of the dielectric constant does not change the Brewster angle. As dielectric constant increases the co – polar power transmission coefficient also increases. After the Brewster angle it sharply decreases to zero value at $\theta=90^\circ$.

There is a slight increase for cross – polar power transmission coefficient as ϵ_r increases but it is close to zero.

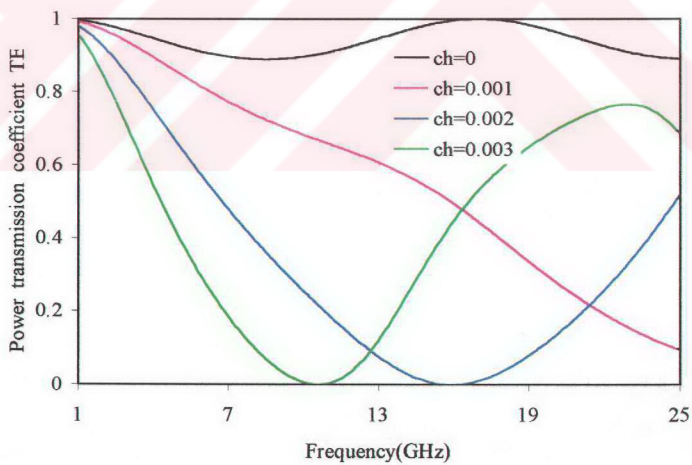
There is no Brewster angle for TE polarization of the incident plane wave as shown in Figure 2.8.a. As ξ changes from 0 to 0.003 the co – polar power reflection coefficient has approximately the same value up to $\theta=20^\circ$. The magnitude of co – polar power transmission coefficient decreases and approaches zero at $\theta=90^\circ$ as ξ increases from 0 to 0.003 and then increases for the value of $\xi=0.006$ S. The cross – polar power transmission coefficient also increases as ξ increases up to $\xi=0.003$ S and then decreases for $\xi=0.006$ S.

The power reflection and transmission coefficients against incident angle θ for different values of slab thickness are shown in Figure 2.9. The magnitude of co – polar power reflection coefficient increases as d increases from $d=3.125$ mm($\lambda/8$) to $d=12.5$ mm($\lambda/2$) and all values approaches unity about 90° . The co – polar power transmission coefficient decreases as the incidence angle increases and approaches zero at $\theta=90^\circ$. The cross – polar power transmission coefficient is nearly zero for $d=12.5$ mm, $d=6.25$ mm and greater for $d=3.125$ mm as shown in Figure 2.9.c.

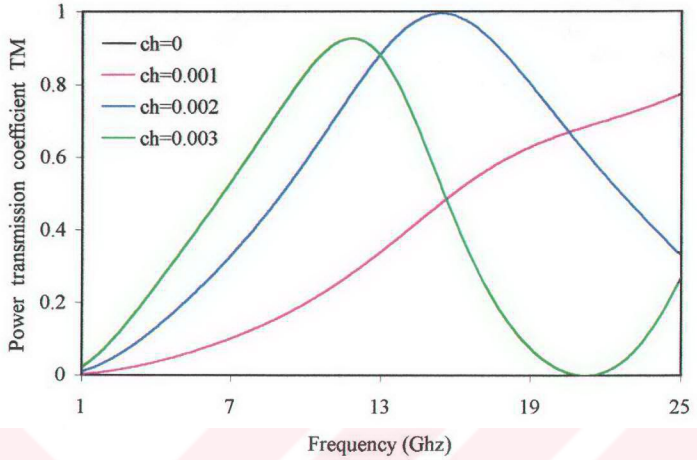
The power reflection and transmission coefficients against incident angle θ for different dielectric constants are shown in Fig. 2.10. When ϵ_r increases the co – polar power reflection coefficient decreases and approaches unity whereas the co – polar power transmission coefficient increases and approaches zero at $\theta=90^\circ$. There is a slight increase for cross – polar power transmission coefficient as ϵ_r increases and as shown from the scale of Figure 2.10.c all of the magnitudes are very close to zero.



(a)

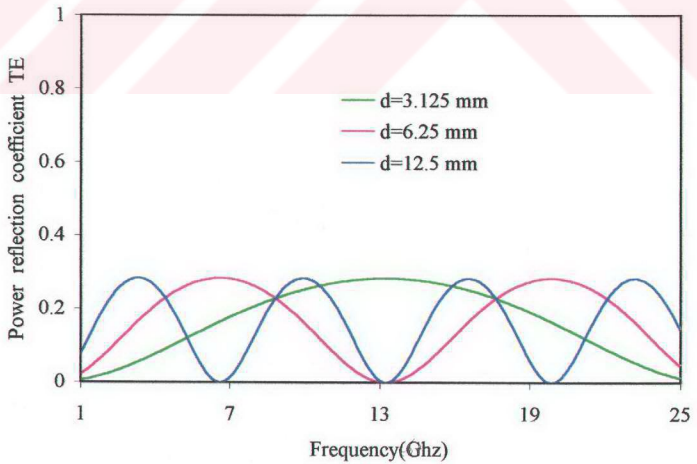


(b)

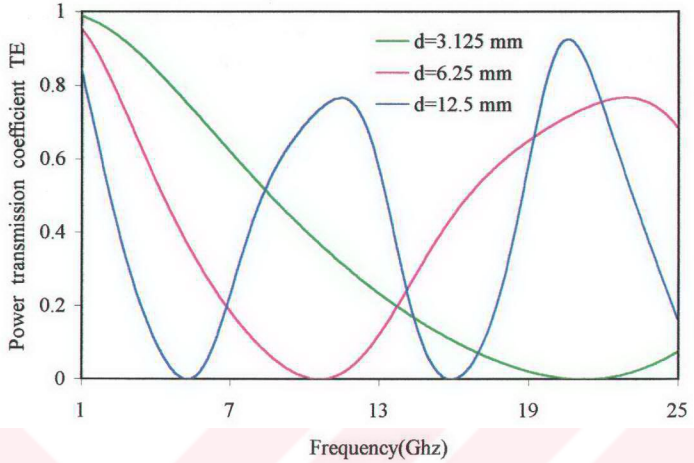


(c)

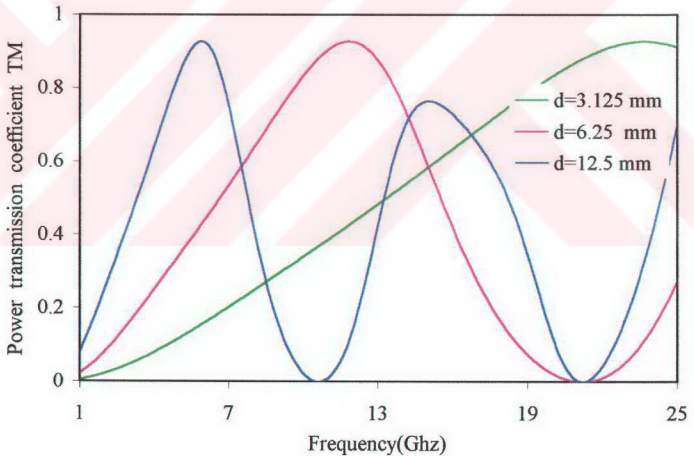
Figure 2.2 Normalized power reflection and transmission coefficients against frequency for different values of chirality admittances; TE normal incidence, $\epsilon_r=2$ and $d=6.25$ mm. (a)- Power reflection coefficient TE, (b)- Power transmission coefficient TE, (c)- Power transmission coefficient TM.



(a)

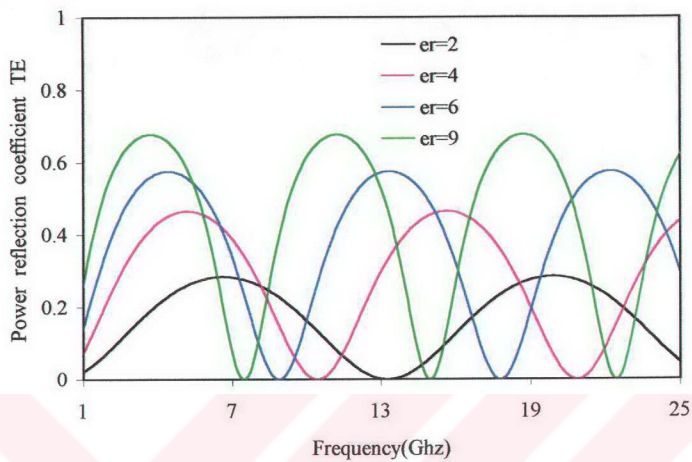


(b)

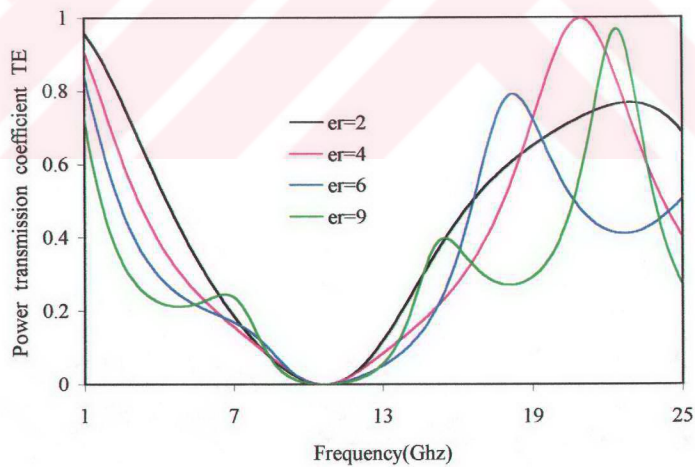


(c)

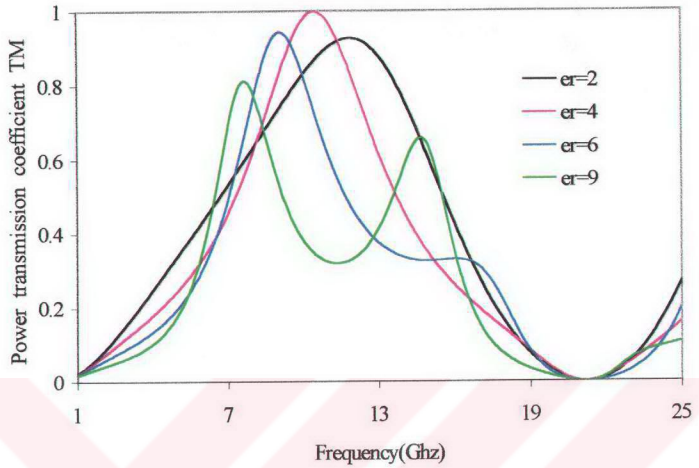
Figure 2.3 Normalized power reflection and transmission coefficients against frequency for different values of slab thickness; TE normal incidence; $\xi=0.003$ S and $\epsilon_r=2$. (a)- Power reflection coefficient TE, (b)- Power transmission coefficient TE, (c)- Power transmission coefficient TM.



(a)

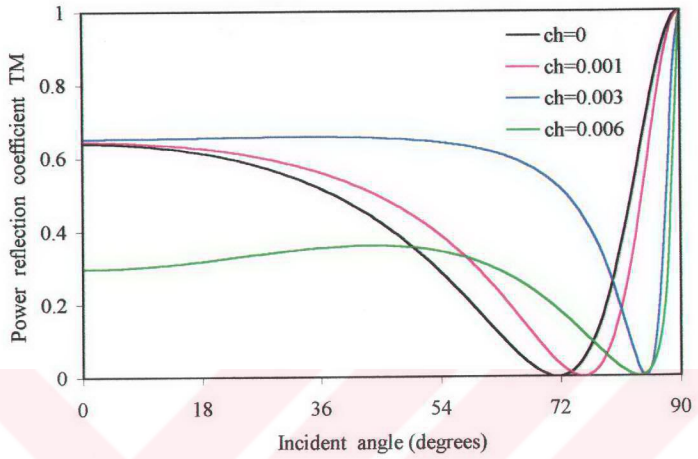


(b)

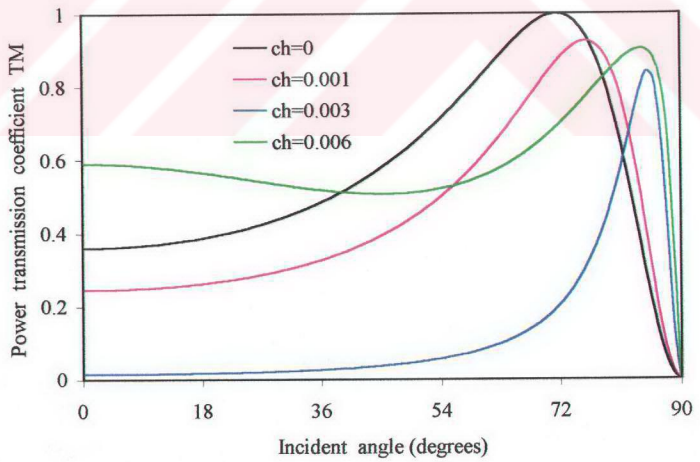


(c)

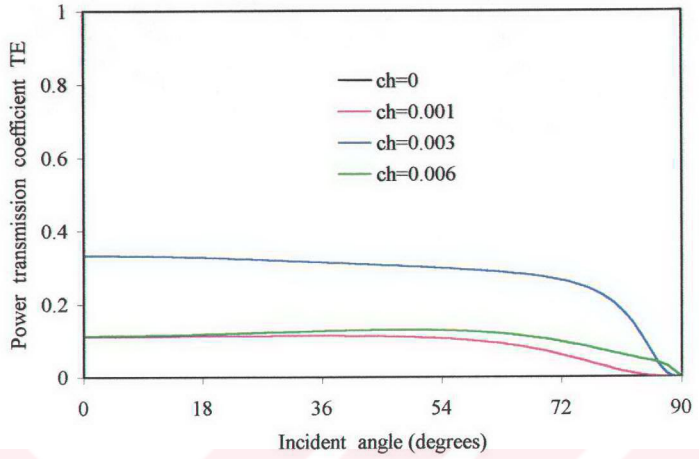
Figure 2.4 Normalized power reflection and transmission coefficients against frequency for different values of dielectric constant; TE normal incidence, $\xi=0.003$ S and $d=6.25$ mm. (a)- Power reflection coefficient TE, (b)- Power transmission coefficient TE, (c)- Power transmission coefficient TM.



(a)

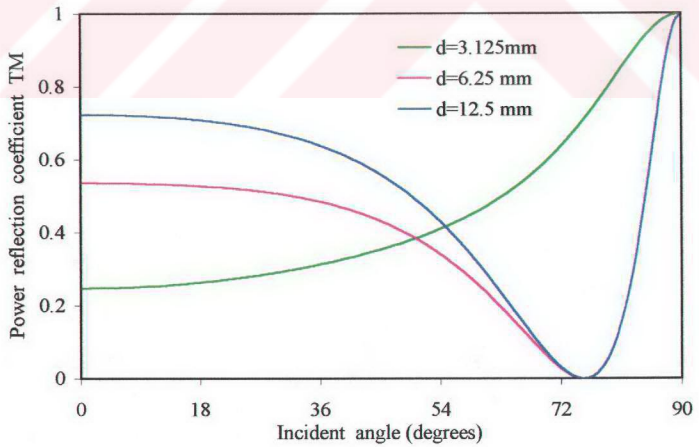


(b)

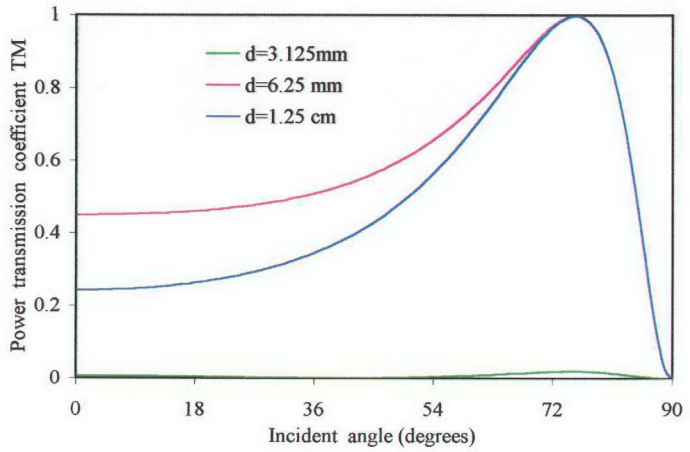


(c)

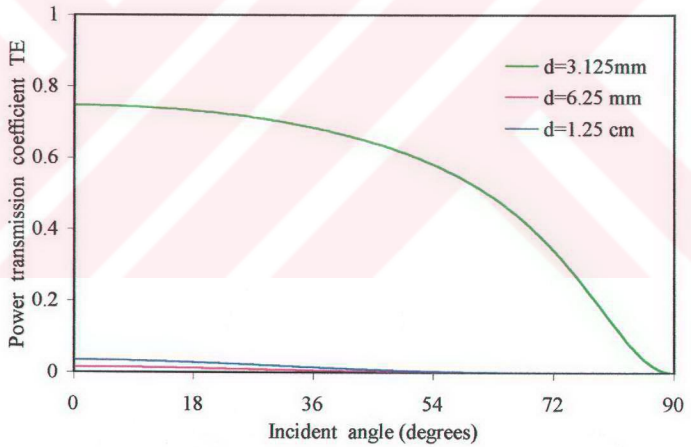
Figure 2.5. Normalized power reflection and transmission coefficients against incident angle θ for different values of chirality admittances; TM incidence, $\epsilon_r=9$ and $d=6.25$ mm. (a) – Power reflection coefficient TM, (b) – Power transmission coefficient TM, (c) – Power transmission coefficient TE.



(a)

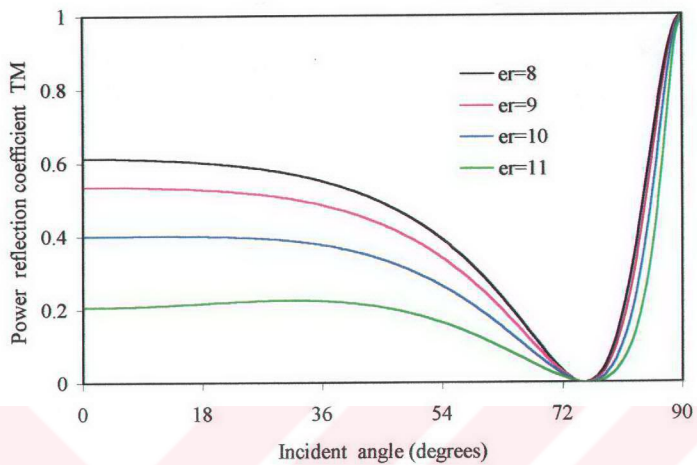


(b)

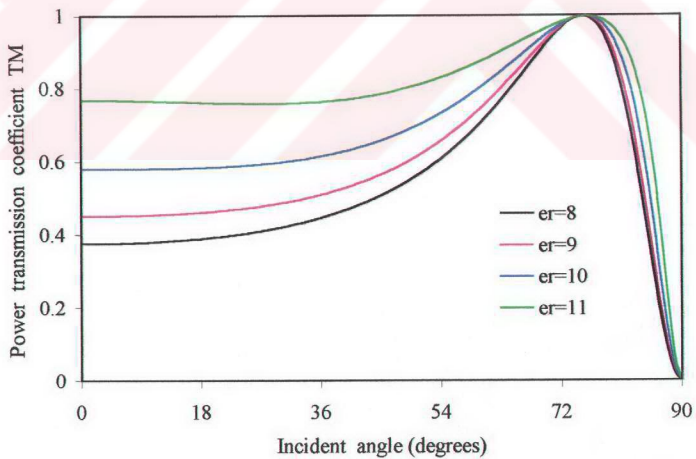


(c)

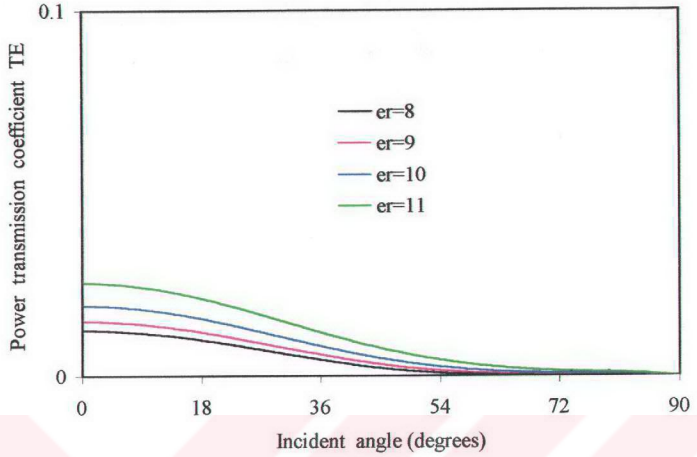
Figure 2.6. Normalized power reflection and transmission coefficients against incident angle θ for different values of slab thickness; TM incidence, $\xi=0.005$ S, and $\epsilon_r=9$. (a) – Power reflection coefficient TM, (b) – Power transmission coefficient TM, (c) – Power transmission coefficient TE.



(a)

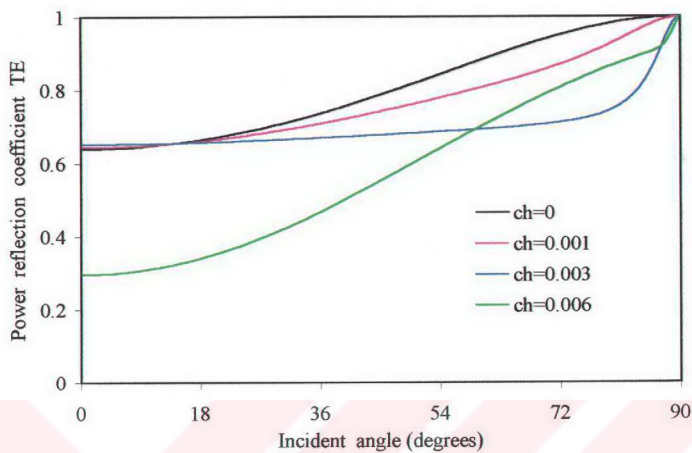


(b)

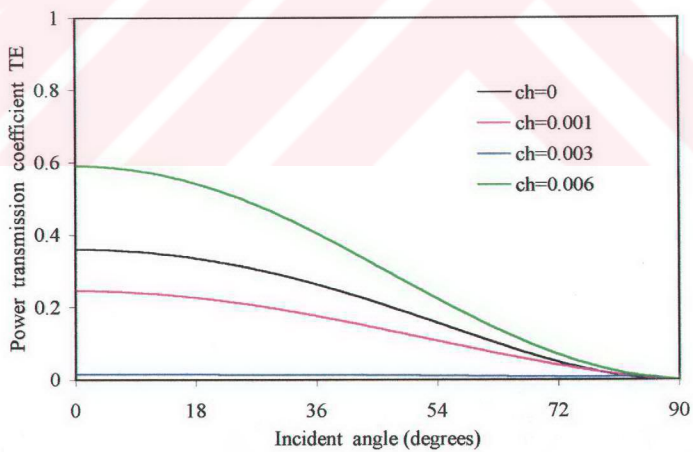


(c)

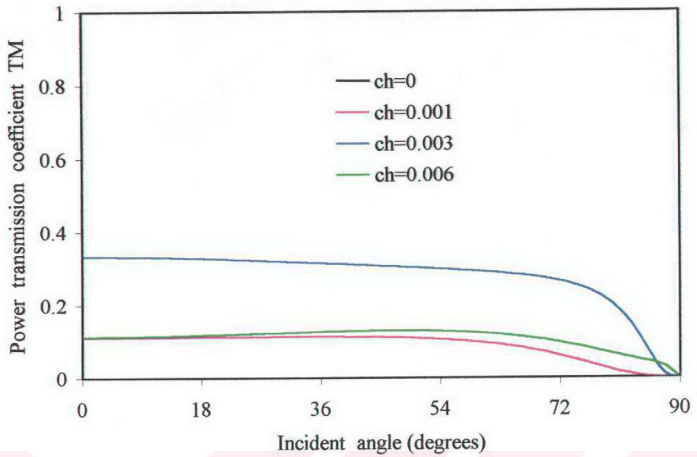
Figure 2.7. Normalized power reflection and transmission coefficients against incident angle θ for different values of dielectric constant; TM incidence, $\xi=0.005$ S and $d=6.25$ mm. (a) – Power reflection coefficient TM, (b) –Power transmission coefficient TM, (c)–Power transmission coefficient TE.



(a)

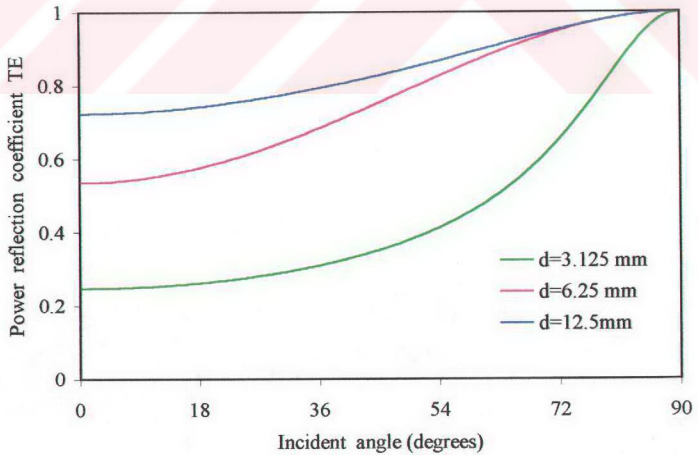


(b)

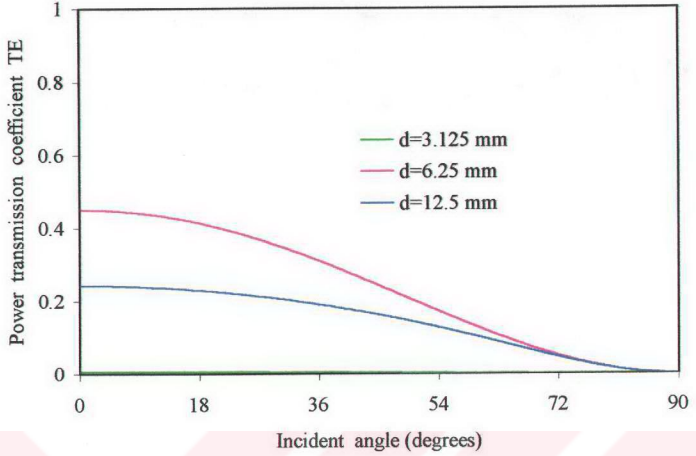


(c)

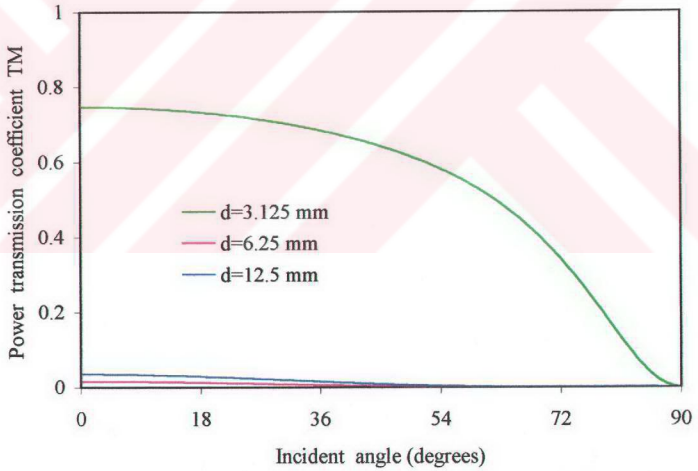
Figure 2.8. Normalized power reflection and transmission coefficients against incident angle θ for different values of chirality admittances; TE incidence, $\epsilon_r=9$ and $d=6.25$ mm. (a) – Power reflection coefficient TE, (b) – Power transmission coefficient TE, (c) – Power transmission coefficient TM.



(a)

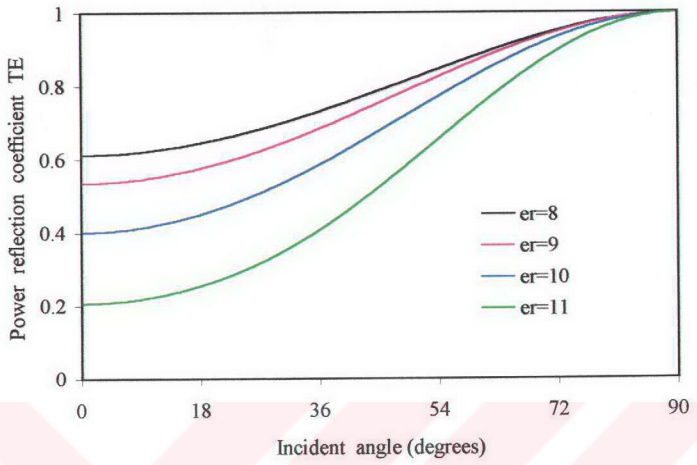


(b)

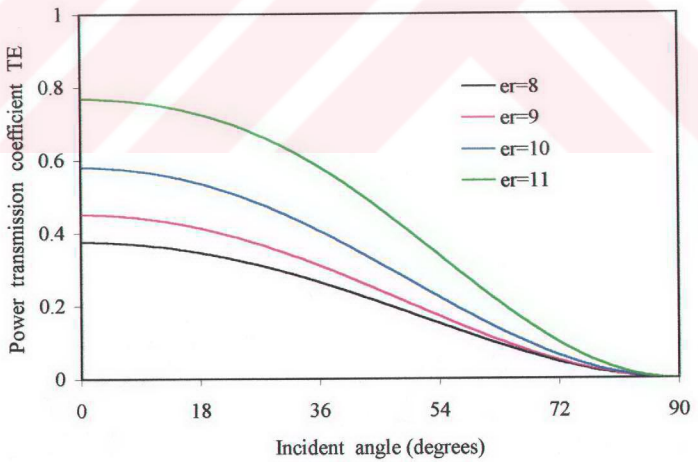


(c)

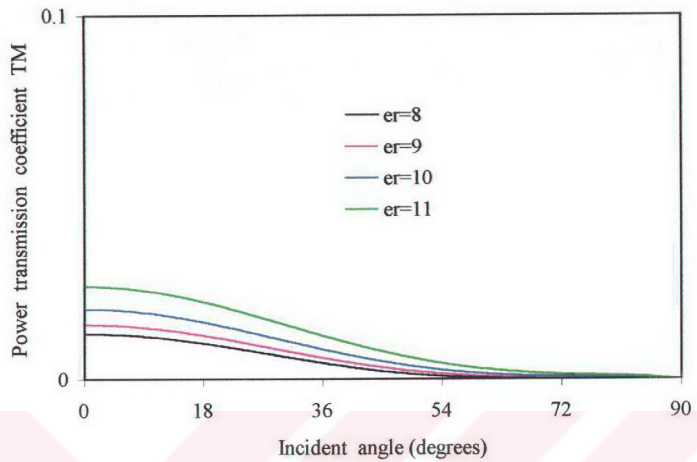
Figure 2.9. Normalized power reflection and transmission coefficients against incident angle θ for different values of slab thickness; TE incidence, $\epsilon_r=9$ and $\xi=0.005$ S. (a) – Power reflection coefficient TE, (b) – Power transmission coefficient TE, (c) – Power transmission coefficient TM.



(a)



(b)



(c)

Figure 2.10. Normalized power reflection and transmission coefficients against incident angle θ for different values of dielectric constant ; TE incidence, $\xi=0.005$ S and $d=6.25$ mm. (a) – Power reflection coefficient TE , (b) – Power transmission coefficient TE , (c) – Power transmission coefficient TM.

CHAPTER 3

ANALYSIS OF MEANDER – LINE POLARIZER WITH CHIRAL SLAB

3.1 Floquet Theorem

Floquet's theorem [32], is essentially an extension of the Fourier series theorem for periodic functions. The extension permits a modal description of any field or function which repeats itself periodically except for a multiplicative exponential factor. The problem of periodic structure and an infinite extent can be solved by using Floquet theorem. Floquet's theorem will allow user to describe the fields in terms of a complete orthogonal set of modes.

To determine a suitable field representation for the fields in the region ($z \geq 0$), any rectangular field component is well known to be a solution of the homogeneous scalar Helmholtz equation. For the periodic Meander-line structure shown in Figure 3.1 Helmholtz equation can be written as,

$$(\nabla^2 + k^2)\bar{\Psi}(x,y,z)=0 \quad (3.1)$$

where $k^2 = \omega^2 \mu \epsilon$. If the field varies with z , the direction of propagation can be written as,

$$\Psi(x,y,z) = e^{-jz} \bar{\Psi}(x,y) \quad (3.2)$$

then Equation (3.1) becomes

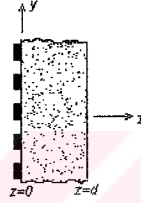
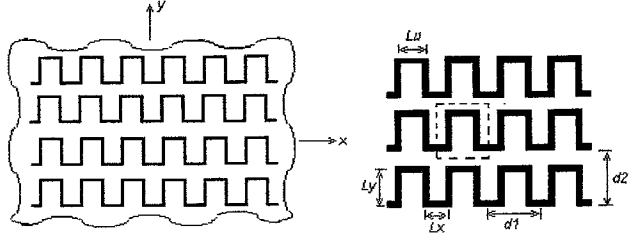


Fig. 3.1 Geometry of the Meander-line Polarizer

$$\left(\frac{\partial^2}{\partial x^2} + \frac{\partial^2}{\partial y^2} + (k^2 - \gamma^2) \right) \bar{\Psi}(x, y) = 0 \quad (3.3)$$

Applying the technique of separation of variables, the partial differential equation (3.3) can be written as two ordinary differential equations:

$$\bar{\Psi}(x, y) = f(x) g(y) \quad (3.4)$$

$$\left(\frac{d^2}{dx^2} + k_x^2 \right) f(x) = 0 \quad (3.5)$$

for the x dependence and

$$\left(\frac{d^2}{dy^2} + k_y^2 \right) g(y) = 0 \quad (3.6)$$

for the y dependence, k_x and k_y are separation constants such that,

$$\gamma^2 = k^2 - k_x^2 - k_y^2$$

The structure is periodic both in x and y directions then the solution should also be periodic according to Floquet theorem. Thus if $f(x)$ and $g(y)$ are to represent the waves propagating in x and y directions, respectively, it is necessary that,

$$f(x+b) = e^{-jk_x b} f(x) \quad (3.7)$$

$$g(y+d) = e^{-jk_y d} g(y) \quad (3.8)$$

where d_1 and d_2 are the periodicities in the x and y directions, respectively. This is possible if,

$$f(x) = e^{-jk_x x} F_p(x) \quad (3.9)$$

$$g(y) = e^{-jk_y y} G_p(y) \quad (3.10)$$

where $F_p(x)$ and $G_p(y)$ are the periodic functions of x with period d_1 and function of y with period d_2 , respectively. Therefore $F_p(x)$ and $G_p(y)$ can be expanded into a Fourier series;

$$F_p(x) = \sum_{p=-\infty}^{\infty} A_p e^{-j \frac{2\pi}{d_1} p x} \quad (3.11)$$

$$G_p(y) = \sum_{q=-\infty}^{\infty} B_q e^{-j \frac{2\pi}{d_2} q y} \quad (3.12)$$

Substituting (3.11) and (3.12) into (3.9) and (3.10) one can obtain ,

$$f(x) = \sum_{p=-\infty}^{\infty} A_p e^{-j \left(k_x + \frac{2\pi}{d_1} p \right) x} \quad (3.13)$$

$$g(y) = \sum_{q=-\infty}^{\infty} B_p e^{-j\left(k_{y0} + \frac{2\pi}{d_2}q\right)y} \quad (3.14)$$

Therefore the solution to equation (3.2) can be written as ,

$$\Psi(x, y, z) = \sum_{p=-\infty}^{\infty} \sum_{q=-\infty}^{\infty} A_{pq} B_{pq} e^{-j\left(k_{x0} + \frac{2\pi}{d_1}p\right)x} e^{-j\left(k_{y0} + \frac{2\pi}{d_2}q\right)y} e^{-j\gamma_{pq}z} \quad (3.15)$$

where

$$\gamma_{pq}^2 = k^2 - \left(k_{x0} + \frac{2\pi}{d_1}p\right)^2 - \left(k_{y0} + \frac{2\pi}{d_2}q\right)^2 \quad (3.16)$$

the constants k_{x0} and k_{y0} are the wave numbers in the x and y direction of the incident wave. Now consider a periodic structure along the skewed (nonorthogonal) coordinates η_1 and η_2 as shown in Figure 3.1. Without loss of generality, the η_1 is chosen to coincide with the x axis and η_2 makes an angle α , with respect to the x axis. Then the element location is now defined by two indices p and q as,

$$\vec{\rho}_{pq} = p d_1 \vec{\eta}_1 + q d_2 \vec{\eta}_2 \quad (3.17)$$

where η_1 and η_2 are unit vectors along the η_1 and η_2 axes, while d_1 and d_2 represent the periodicities of the two dimensional structure along η_1 and η_2 , respectively. A basic unit cell now has the shape of a parallelogram as depicted in Figure 3.1.

The lattice geometry described by the vectors η_1 and η_2 will be referred as direct lattice. The η_1 and η_2 vectors can also be written in terms of cartesian coordinate systems as follows,

$$\begin{bmatrix} \vec{\eta}_1 \\ \vec{\eta}_2 \end{bmatrix} = \begin{bmatrix} 1 & 0 \\ \cos\alpha & \sin\alpha \end{bmatrix} \begin{bmatrix} \vec{a}_x \\ \vec{a}_y \end{bmatrix} \quad (3.18)$$

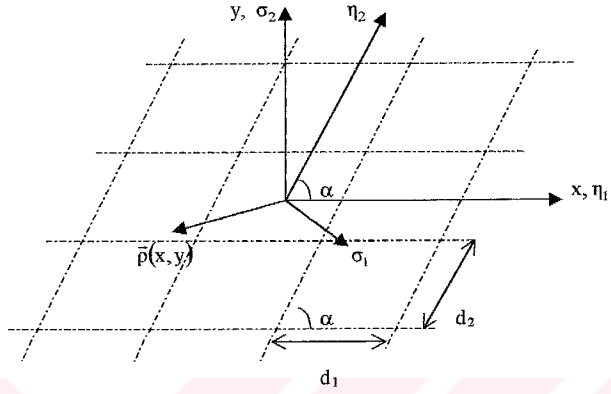


Fig. 3.2 Lattice geometry

One may also define another set of vectors σ_1 and σ_2 called reciprocal lattice vectors such that ,

$$\vec{\sigma}_i \cdot \vec{\eta}_k = \delta_{ik} = \begin{cases} 1 & i = k \\ 0 & i \neq k \end{cases}, i = k = 1, 2 \quad (3.19)$$

writing σ_1 and σ_2 in terms of cartesian components,

$$\begin{aligned} \vec{\sigma}_1 &= \vec{a}_x \sigma_{11} + \vec{a}_y \sigma_{12} \\ \vec{\sigma}_2 &= \vec{a}_x \sigma_{21} + \vec{a}_y \sigma_{22} \end{aligned} \quad (3.20)$$

from equations (3.18),(3.19) and (3.20) the following relations are obtained,

$$\begin{aligned} \vec{\eta}_1 \cdot \vec{\sigma}_1 &= \sigma_{11} = 1 \\ \vec{\eta}_1 \cdot \vec{\sigma}_2 &= \sigma_{21} = 0 \\ \vec{\eta}_2 \cdot \vec{\sigma}_1 &= \sigma_{11} \cos \alpha + \sigma_{12} \sin \alpha = 0 \\ \vec{\eta}_2 \cdot \vec{\sigma}_2 &= \sigma_{21} \cos \alpha + \sigma_{22} \sin \alpha = 1 \end{aligned} \quad (3.21)$$

from equation (3.21) one can obtain ,

$$\sigma_{11} = 1, \sigma_{21} = 0, \sigma_{12} = -\cot\alpha, \sigma_{22} = \operatorname{cosec}\alpha$$

Therefore the reciprocal vectors will be

$$\begin{aligned}\vec{\sigma}_1 &= \vec{a}_x - \vec{a}_y \cot\alpha \\ \vec{\sigma}_2 &= \vec{a}_y \operatorname{cosec}\alpha\end{aligned}\quad (3.22)$$

Now consider a periodic function $F(x, y)$ in the direct lattice such that it has the same values at points defined by the vectors,

$$\vec{\rho}(x, y) = x\vec{a}_x + y\vec{a}_y \quad (3.23)$$

$$\vec{\rho}(\eta_1, \eta_2) = \eta_1\vec{\eta}_1 + \eta_2\vec{\eta}_2 \quad (3.24)$$

$\vec{\rho}(x, y)$ is represented by η_1 and η_2 components along the unit vectors. Thus a new function $f(\eta_1, \eta_2)$ with periods d_1 and d_2 in η_1 and η_2 directions are obtained. This function can be written in Fourier series as,

$$f(\eta_1, \eta_2) = \sum_{p=-\infty}^{\infty} \sum_{q=-\infty}^{\infty} A_{pq} B_{pq} e^{-j\frac{2\pi}{d_1} p\eta_1} e^{-j\frac{2\pi}{d_2} q\eta_2} \quad (3.25)$$

remembering $\sigma_1 \perp \eta_2$ and $\sigma_2 \perp \eta_1$, η_1 and η_2 can be expressed in terms of reciprocal lattice vectors,

$$\begin{aligned}\vec{\sigma}_1 \cdot \vec{\rho} &= (\vec{\sigma}_1 \cdot \vec{\eta}_1)\eta_1 + (\vec{\sigma}_1 \cdot \vec{\eta}_2)\eta_2 = \eta_1 \\ \vec{\sigma}_2 \cdot \vec{\rho} &= (\vec{\sigma}_2 \cdot \vec{\eta}_1)\eta_1 + (\vec{\sigma}_2 \cdot \vec{\eta}_2)\eta_2 = \eta_2\end{aligned}\quad (3.26)$$

Substituting in equation (3.25)

$$F(x, y) = \sum_{p=-\infty}^{\infty} \sum_{q=-\infty}^{\infty} A_{pq} B_{pq} e^{-j\frac{2\pi}{d_1} p(\vec{\sigma}_1 \cdot \vec{\rho})} e^{-j\frac{2\pi}{d_2} q(\vec{\sigma}_2 \cdot \vec{\rho})} \quad (3.27)$$

in terms of x , y and α ,

$$F(x, y) = \sum_{p=-\infty}^{\infty} \sum_{q=-\infty}^{\infty} A_{pq} B_{pq} e^{-j\frac{2\pi}{d_1} p(x-y \cot \alpha)} e^{-j\frac{2\pi}{d_2} qy \operatorname{cosec} \alpha} \quad (3.28)$$

where

$$\begin{aligned}\eta_1 &= \bar{\sigma}_1 \cdot \bar{\rho} = x - y \cot \alpha \\ \eta_2 &= \bar{\sigma}_2 \cdot \bar{\rho} = y \operatorname{cosec} \alpha\end{aligned}\quad (3.29)$$

For the periodic structure shown in Figure (3.1) a complete set of solution given by equation (3.15) the scalar wave equation can be written as,

$$\Psi = \sum_p \sum_q A_{pq} B_{pq} e^{-j\left(k_{\eta_1} + \frac{2\pi}{d_1} p\right) \eta_1} e^{-j\left(k_{\eta_2} + \frac{2\pi}{d_2} q\right) \eta_2} e^{-j\gamma_{pq} z} \quad (3.30)$$

where k_{η_1} and k_{η_2} are the wave numbers along the η_1 and η_2 axis respectively.

$$\begin{aligned}k_{\eta_1} &= \bar{\eta}_1 \cdot \bar{k} = \bar{a}_x \cdot \bar{k} = k \sin \theta \cos \varphi \\ k_{\eta_2} &= \bar{\eta}_2 \cdot \bar{k} = (\bar{a}_x \cos \alpha + \bar{a}_y \sin \alpha) \cdot \bar{k} \\ k_{\eta_2} &= k (\sin \theta \cos \varphi \cos \alpha + \sin \theta \sin \varphi \sin \alpha) \\ \bar{k} &= k \sin \theta \cos \varphi \bar{a}_x + k \sin \theta \sin \varphi \bar{a}_y + k \cos \theta \bar{a}_z\end{aligned}\quad (3.31)$$

therefore Equation (3.30) can be rewritten as,

$$\Psi = \sum_{p=-\infty}^{\infty} \sum_{q=-\infty}^{\infty} A_{pq} B_{pq} e^{-j\left(k_{x_0} + \frac{2\pi}{d_1} p\right) x} e^{-j\left(k_{y_0} - \frac{2\pi}{d_1 \tan \alpha} p + \frac{2\pi}{d_2 \sin \alpha} q\right) y} e^{-j\gamma_{pq} z} \quad (3.32)$$

where

$$\gamma_{pq}^2 = k^2 - \left(k_{x_0} + \frac{2\pi}{d_1} p\right)^2 - \left(k_{y_0} - \frac{2\pi}{d_1 \tan \alpha} p + \frac{2\pi}{d_2 \sin \alpha} q\right)^2 \quad (3.33)$$

Now let us define two vectors k_1 and k_2 ,

$$\begin{aligned}\bar{k}_1 &= \frac{2\pi d_2}{A} \bar{\eta}_2 \times \bar{a}_z \\ \bar{k}_1 &= \frac{2\pi d_2}{A} (\cos \alpha \bar{a}_x + \sin \alpha \bar{a}_y) \times \bar{a}_z = \bar{a}_x \frac{2\pi}{d_1} - \bar{a}_y \frac{2\pi}{d_1 \tan \alpha}\end{aligned}\quad (3.34)$$

$$\bar{k}_2 = \frac{2\pi b}{A} \bar{a}_z \times \bar{a}_x = \frac{2\pi}{d \sin \alpha} \bar{a}_y \quad (3.35)$$

where A is the area of the unit cell, $A = d_1 d_2 \sin \alpha$.

$$(\vec{p}\vec{k}_1 + q\vec{k}_2) \cdot \vec{\rho} = \frac{2\pi p}{d_1} x + \left(\frac{2\pi q}{d_2 \sin \alpha} - \frac{2\pi p}{d_1 \tan \alpha} \right) y \quad (3.36)$$

substituting equation (3.36) into (3.32) yields;

$$\Psi = \sum_{p=-\infty}^{\infty} \sum_{q=-\infty}^{\infty} A_{pq} B_{pq} e^{-j(k_{x0}x + k_{y0}y)} e^{-j(\vec{p}\vec{k}_1 + q\vec{k}_2) \cdot \vec{\rho}} e^{-j\gamma_{pq}z} \quad (3.37)$$

$$\Psi = \sum_{p=-\infty}^{\infty} \sum_{q=-\infty}^{\infty} A_{pq} B_{pq} e^{-j\vec{k}_{\Gamma pq} \cdot \vec{\rho}} e^{-j\gamma_{pq}z} \quad (3.38)$$

where $\vec{k}_{\Gamma pq} = \vec{k}_{\Gamma} + p\vec{k}_1 + q\vec{k}_2$

$$\vec{k}_{\Gamma pq} = \left(k_{x0} + \frac{2\pi}{d_1} p \right) \vec{a}_x + \left(k_{y0} - \frac{2\pi}{d_1 \tan \alpha} p + \frac{2\pi}{d_2 \sin \alpha} q \right) \vec{a}_y \quad (3.39)$$

$$\gamma_{pq}^2 = k^2 - \vec{k}_{\Gamma pq} \cdot \vec{k}_{\Gamma pq}, \quad k_{x0} = k \sin \theta \cos \varphi, \quad k_{y0} = k \sin \theta \sin \varphi.$$

3.2 Formulation of the problem

In this section, a more general formulation of the scattering problem of a two dimensional periodic array of thin meander-line strips is presented. The formulation applies to thin perfectly conducting meander-line placed periodically along any two skewed coordinates. The incident field is assumed to be a plane wave of either TM or TE polarization. The incident field is produced by the external sources in the absence of the any scatterers (meander-line) and the presence of the chiral slab. The total field is the sum of the incident field and the field scattered from the conducting body. Therefore, the scattered field at any point in space is the difference between the total field and the incident field at that point. The scattered fields, on the other hand, are produced by the current distributions on the scatterers. The procedure to be presented here is to expand the electromagnetic field distribution near the array of conducting meander-line strips into a set of Floquet mode functions. By requiring the total electric field vanish on the conducting strips ,

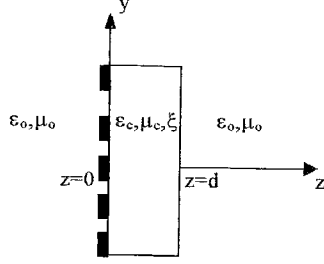


Fig. 3.3 Side view of Meander-line polarizer with chiral slab

an integral equation for the unknown current is first expressed by complete set of orthonormal mode functions and then its mode coefficients are determined by the method of moments. The scattered fields due to the current induced on the scatterers contain higher order Floquet modes. The electric field in dielectric region ($z < 0$), for TM incidence can be written as;

$$\vec{E}_1 = \sum_{m=1}^2 \sum_p \sum_q j^{m-1} E_{1pq}^{(m)} e^{jY_{pq}z} \vec{\Psi}_{1mpq} \quad (3.40a)$$

$$\vec{H}_1 = -\vec{a}_z \times \sum_{m=1}^2 \sum_p \sum_q j^{m-1} Y_{pq}^m E_{1pq}^{(m)} e^{jY_{pq}z} \vec{\Psi}_{1mpq} \quad (3.40b)$$

where [21], $\vec{\Psi}_{1mpq} = \frac{1}{\sqrt{A}} e^{-jk_{Tpq} \cdot \vec{r}_T} \vec{e}_{1mpq}$, $m=1$ or 2 , $p, q=0, \pm 1, \pm 2, \pm 3, \dots$

$$\vec{e}_{1pq} = \frac{\vec{k}_{Tpq}}{|\vec{k}_{Tpq}|}, \quad \text{TM modes (m=1)}$$

$$\vec{e}_{2pq} = \vec{a}_z \times \vec{e}_{1pq}, \quad \text{TE modes (m=2)}$$

inside the chiral slab, $0 < z < d$

$$\vec{E}_2^+ = \sum_{m=1}^2 \sum_p \sum_q j^{m-1} (A_{Lpq}^{(m)} e^{-jY_{Lpq}z} + (-1)^{m-1} A_{Rpq}^{(m)} e^{-jY_{Rpq}z}) \vec{\Psi}_{mpq} \quad (3.41a)$$

$$\vec{E}_2^- = \sum_{m=1}^2 \sum_p \sum_q (-j)^{m-1} (B_{Lpq}^{(m)} e^{j\gamma_{Lpq} z} + (-1)^{m-1} B_{Rpq}^{(m)} e^{j\gamma_{Rpq} z}) \vec{\Psi}_{mpq} \quad (3.41b)$$

$$\vec{H}_2^+ = \vec{a}_z \times \sum_{m=1}^2 \sum_p \sum_q j^{m-1} (Y_{Lpq}^{(m)} A_{Lpq}^{(m)} \cdot e^{-j\gamma_{Lpq} z} + (-1)^{m-1} Y_{Rpq}^{(m)} A_{Rpq}^{(m)} \cdot e^{-j\gamma_{Rpq} z}) \vec{\Psi}_{mpq} \quad (3.42a)$$

$$\vec{H}_2^- = -\vec{a}_z \times \sum_{m=1}^2 \sum_p \sum_q (-j)^{m-1} (Y_{Lpq}^{(m)} B_{Lpq}^{(m)} \cdot e^{j\gamma_{Lpq} z} + (-1)^{m-1} Y_{Rpq}^{(m)} B_{Rpq}^{(m)} \cdot e^{j\gamma_{Rpq} z}) \vec{\Psi}_{mpq} \quad (3.42b)$$

for $z > d$,

$$\vec{E}_3 = \sum_{m=1}^2 \sum_p \sum_q j^{m-1} E_{3pq}^{(m)} e^{-j\gamma_{pq}(z-d)} \vec{\Psi}_{mpq} \quad (3.43a)$$

$$\vec{H}_3 = \vec{a}_z \times \sum_{m=1}^2 \sum_p \sum_q j^{m-1} Y_{pq}^{(m)} E_{3pq}^{(m)} e^{-j\gamma_{pq}(z-d)} \vec{\Psi}_{mpq} \quad (3.43b)$$

The following boundary conditions should be satisfied due to the scatterer at $z=0$:

1. At $z=0$ tangential component of the electric field must be continuous that is; $\vec{E}_1 = (\vec{E}_2^+ + \vec{E}_2^-)$.

2. The boundary condition on the tangential magnetic field at $z=0$ is that the field must be discontinuous by an amount equal to current density on the scatterer according to

$$\vec{a}_z \times \{ (\vec{H}_2^+ + \vec{H}_2^-) - \vec{H}_1 \} = \vec{J} \quad (3.44)$$

3. Tangential components of electric and magnetic fields are continuous at $z=d$, that is, $(\vec{E}_2^+ + \vec{E}_2^-) = \vec{E}_3$ and $(\vec{H}_2^+ + \vec{H}_2^-) = \vec{H}_3$.

Matching these three boundary conditions combined with the orthogonality of the Floquet modes over a unit cell leads to an integral equations in which the magnitude of the scattered fields are expressed in terms of unknown current density.

$$E_{\text{tpqm}}^{\text{TM}} = A_{\text{Lpq}}^{(m)} + (-1)^{m-1} A_{\text{Rpq}}^{(m)} + (-1)^{m-1} B_{\text{Lpq}}^{(m)} + B_{\text{Rpq}}^{(m)} \quad (3.45)$$

$$E_{\text{tpqm}}^{\text{TM}} = A_{\text{Lpq}}^{(m)} e^{-j\gamma_{\text{Lpq}} d} + (-1)^{m-1} A_{\text{Rpq}}^{(m)} e^{-j\gamma_{\text{Rpq}} d} + (-1)^{m-1} B_{\text{Lpq}}^{(m)} e^{j\gamma_{\text{Lpq}} d} + B_{\text{Rpq}}^{(m)} e^{j\gamma_{\text{Rpq}} d} \quad (3.46)$$

where

$$\begin{bmatrix} B_{\text{Lpq}} \\ B_{\text{Rpq}} \end{bmatrix} = \frac{1}{u} \begin{bmatrix} u_1 & u_2 \\ u_3 & u_4 \end{bmatrix} \begin{bmatrix} A_{\text{Lpq}} \\ A_{\text{Rpq}} \end{bmatrix}, \quad \begin{bmatrix} A_{\text{Lpq}} \\ A_{\text{Rpq}} \end{bmatrix} = \frac{1}{v} \begin{bmatrix} v_1 & v_2 \\ v_3 & v_4 \end{bmatrix} \begin{bmatrix} E_{\text{tpq1}}^{\text{TM}} \\ E_{\text{tpq2}}^{\text{TM}} \end{bmatrix}$$

$$\begin{bmatrix} E_{\text{tpq1}}^{\text{TM}} \\ E_{\text{tpq2}}^{\text{TM}} \end{bmatrix} = \frac{1}{r} \begin{bmatrix} r_1 & r_2 \\ r_3 & r_4 \end{bmatrix} \begin{bmatrix} E_{\text{tpq1}}^{\text{TM}} \\ E_{\text{tpq2}}^{\text{TM}} \end{bmatrix} = \begin{bmatrix} t_1 & t_2 \\ t_3 & t_4 \end{bmatrix} \frac{1}{v} \begin{bmatrix} v_1 & v_2 \\ v_3 & v_4 \end{bmatrix} \frac{1}{r} \begin{bmatrix} r_1 & r_2 \\ r_3 & r_4 \end{bmatrix} \begin{bmatrix} I_{\text{1pq}} \\ I_{\text{2pq}} \end{bmatrix}$$

$$u = (Y^{(1)} + Y_L^{(1)})(Y^{(2)} + Y_R^{(2)})Y_L^{(2)} + (Y^{(2)} + Y_L^{(2)})(Y^{(1)} + Y_R^{(1)})Y_R^{(2)}$$

$$u_1 = [(Y^{(1)} + Y_R^{(1)})(Y^{(2)} - Y_L^{(2)})Y_R^{(2)} - (Y^{(2)} + Y_R^{(2)})(Y^{(1)} - Y_L^{(1)})Y_L^{(2)}] e^{-j2\gamma_{\text{L}} d}$$

$$u_2 = [(Y^{(1)} + Y_R^{(1)})(Y_R^{(2)} - Y^{(2)}) - (Y^{(1)} - Y_R^{(1)})(Y^{(2)} + Y_R^{(2)})] Y_R^{(2)} e^{-j2(\gamma_{\text{L}} + \gamma_{\text{R}}) d}$$

$$u_3 = -[(Y^{(1)} - Y_L^{(1)})(Y_L^{(2)} + Y^{(2)}) - (Y^{(1)} + Y_L^{(1)})(Y^{(2)} - Y_L^{(2)})] Y_L^{(2)} e^{-j2(\gamma_{\text{L}} + \gamma_{\text{R}}) d}$$

$$u_4 = -[(Y^{(1)} - Y_R^{(1)})(Y^{(2)} + Y_L^{(2)})Y_R^{(2)} + (Y_R^{(2)} - Y^{(2)})(Y^{(1)} + Y_L^{(1)})Y_L^{(2)}] e^{-j2\gamma_{\text{R}} d}$$

$$v = (Y_L^{(2)} + Y_L^{(2)}u_1 + Y_R^{(2)}u_3)(-1 - u_2 + u_4) - (1 - u_1 + u_3)(Y_R^{(2)} + Y_L^{(2)}u_2 + Y_R^{(2)}u_4)$$

$$v_1 = Y_c(-1 - u_2 + u_4), \quad v_2 = -Y_R^{(2)} - Y_L^{(2)}u_2 - Y_R^{(2)}u_4$$

$$v_3 = Y_c(-1 + u_1 - u_3), \quad v_4 = Y_L^{(2)} + Y_L^{(2)}u_1 + Y_R^{(2)}u_3$$

$$r = r_1 \quad r_4 - r_2 \quad r_3$$

$$r_1 = v_2(-Y_L^{(2)} - Y_L^{(2)}u_1 + Y_R^{(2)}u_3) + v_4(Y_R^{(2)} - Y_L^{(2)}u_2 + Y_R^{(2)}u_4) - Y^{(2)}$$

$$r_2 = j[Y_c v_2(-1 + u_1 + u_3) + Y_c v_4(-1 + u_2 + u_4)]$$

$$r_3 = -v_1(-Y_L^{(2)} - Y_L^{(2)}u_1 + Y_R^{(2)}u_3) - v_3(Y_R^{(2)} - Y_L^{(2)}u_2 + Y_R^{(2)}u_4)$$

$$r_4 = -j[Y_c v_1(-1 + u_1 + u_3) + Y_c v_3(-1 + u_2 + u_4)] - Y^{(1)}$$

$$t_1 = \frac{1}{Y_c} [Y_L^{(2)} e^{-j\gamma_L d} + \frac{1}{u} (Y_L^{(2)} u_1 e^{j\gamma_L d} + Y_R^{(2)} u_3 e^{j\gamma_R d})]$$

$$t_2 = \frac{1}{Y_c} [Y_R^{(2)} e^{-j\gamma_R d} + \frac{1}{u} (Y_L^{(2)} u_2 e^{j\gamma_L d} + Y_R^{(2)} u_4 e^{j\gamma_R d})]$$

$$t_3 = e^{-j\gamma_L d} - \frac{1}{u} (u_1 e^{j\gamma_L d} - u_3 e^{j\gamma_R d}), \quad t_4 = -e^{-j\gamma_R d} - \frac{1}{u} (u_2 e^{j\gamma_L d} - u_4 e^{j\gamma_R d})$$

$$A_{Lpq}^{(m)} = \left(\frac{Y_{Lpq}^{(2)}}{Y_c} \right)^{2-m} A_{Lpq}, \quad A_{Rpq}^{(m)} = \left(\frac{Y_{Rpq}^{(2)}}{Y_c} \right)^{2-m} A_{Rpq}$$

$$B_{Lpq}^{(m)} = \left(\frac{Y_{Lpq}^{(2)}}{Y_c} \right)^{2-m} B_{Lpq}, \quad B_{Rpq}^{(m)} = \left(\frac{Y_{Rpq}^{(2)}}{Y_c} \right)^{2-m} B_{Rpq}$$

$$Y_{Lpq}^{(1)} = Y_c \frac{k_L}{\gamma_{Lpq}}, \quad Y_{Rpq}^{(1)} = Y_c \frac{k_R}{\gamma_{Rpq}}, \quad Y_{pq}^{(1)} = Y \frac{k}{\gamma_{pq}}$$

$$Y_{Lpq}^{(2)} = Y_c \frac{\gamma_{Lpq}}{k_L}, \quad Y_{Rpq}^{(2)} = Y_c \frac{\gamma_{Rpq}}{k_R}, \quad Y_{pq}^{(2)} = Y \frac{\gamma_{pq}}{k}$$

$$\gamma_{L,Rpq} = \left\{ \begin{array}{ll} \sqrt{k_{L,R}^2 - |k_{Tpq}|^2} & k_{L,R}^2 > |k_{Tpq}|^2 \\ -j\sqrt{|k_{Tpq}|^2 - k_{L,R}^2} & k_{L,R}^2 < |k_{Tpq}|^2 \end{array} \right\}$$

$$I_{mpq} = \frac{1}{\sqrt{A}} \iint \vec{J}(x, y) \cdot e^{j\vec{k}_{Tpq} \cdot \vec{r}} \vec{c}_{mpq} dx dy, \quad A = d_1 d_2 \sin \alpha$$

The current density function can be expanded into a finite series with unknown coefficients,

$$\vec{J} = \sum_{n=1}^N \alpha_n \vec{I}_n(x, y) \quad (3.47)$$

$$\mathbf{I}_{mpq} = \frac{1}{\sqrt{A}} \iint \sum_{n=1}^N \alpha_n \bar{\mathbf{I}}_n(x, y) \cdot \bar{\Psi}_{mpq} dx dy = \sum_{n=1}^N \alpha_n \langle \bar{\mathbf{I}}_n, \bar{\Psi}_{mpq} \rangle \quad (3.48)$$

To find unknown current density the Moment Method is used. After finding current density, the unknown complex coefficients can be found in terms of the current density and the medium parameters.

Since both the scattered and incident field satisfy the air-chiral boundary conditions, the only remaining boundary condition is that the total tangential electric field vanish on the metallic part of the scatterer (meander-line). Therefore at $z=0$ we have ,

$$\bar{\mathbf{E}}_{inc}(x, y, 0) + \bar{\mathbf{E}}_{ref}(x, y, 0) + \bar{\mathbf{E}}_{scat}(x, y, 0) = 0 \quad (3.49)$$

$$\sum_{m=1}^2 (\mathbf{E}_o^{TM} + j^{m-1} \mathbf{E}_{ro1}^{TM}) \bar{\Psi}_m = - \sum_{m=1}^2 \sum_p \sum_q j^{m-1} \mathbf{E}_{rpqm}^{TM} \bar{\Psi}_{mpq} \quad (3.50)$$

Multiplying both sides of above equation by $\mathbf{I}_1, \mathbf{I}_2, \mathbf{I}_3, \dots, \mathbf{I}_N$ successively and then integrating over a unit cell N set of equations can be obtained ,

$$(\mathbf{E}_o^{TM} + \mathbf{E}_{ro1}^{TM}) \langle \bar{\mathbf{I}}_k, \bar{\Psi}_1^* \rangle + j \mathbf{E}_{ro2}^{TM} \langle \bar{\mathbf{I}}_k, \bar{\Psi}_2^* \rangle = - \frac{1}{A} \sum_{n=1}^N \alpha_n \sum_q \sum_p [$$

$$(\tau_1 \langle \bar{\mathbf{I}}_n, \bar{\Psi}_{1pq} \rangle + \tau_2 \langle \bar{\mathbf{I}}_n, \bar{\Psi}_{2pq} \rangle) \langle \bar{\mathbf{I}}_k, \bar{\Psi}_{1pq}^* \rangle$$

$$+ j (\tau_3 \langle \bar{\mathbf{I}}_n, \bar{\Psi}_{1pq} \rangle + \tau_4 \langle \bar{\mathbf{I}}_n, \bar{\Psi}_{2pq} \rangle) \langle \bar{\mathbf{I}}_k, \bar{\Psi}_{2pq}^* \rangle] \quad (3.51)$$

where $k = 1, 2, 3, \dots, N$

Equation (3.51) is a matrix equation for the unknown coefficients of the current expansion. Upon finding the unknown coefficients α_n by complex matrix inversion we can find the total reflected field at $z=0$ as,

$$\begin{aligned} \vec{E}_r = & \{ E_{r01}^{TM} \vec{\Psi}_1 + \frac{1}{\sqrt{A}} \sum_{n=1}^N \alpha_n \sum_{p=-\infty}^{\infty} \sum_{q=-\infty}^{\infty} (r_1 < \vec{l}_n, \vec{\Psi}_{1pq} > + r_2 < \vec{l}_n, \vec{\Psi}_{2pq} >) \vec{\Psi}_{1pq} \\ & + j [E_{r02}^{TM} \vec{\Psi}_2 + \frac{1}{\sqrt{A}} \sum_{n=1}^N \alpha_n \sum_{p=-\infty}^{\infty} \sum_{q=-\infty}^{\infty} (r_3 < \vec{l}_n, \vec{\Psi}_{1pq} > + r_4 < \vec{l}_n, \vec{\Psi}_{2pq} >) \vec{\Psi}_{2pq}] \} \end{aligned} \quad (3.52)$$

We can also find the transmitted field at $z=d$,

$$\begin{aligned} \vec{E}_t = & \{ E_{t01}^{TM} \vec{\Psi}_1 + \frac{1}{\sqrt{A}} \sum_{n=1}^N \alpha_n \sum_{p=-\infty}^{\infty} \sum_{q=-\infty}^{\infty} (t_1 < \vec{l}_n, \vec{\Psi}_{1pq} > + t_2 < \vec{l}_n, \vec{\Psi}_{2pq} >) \vec{\Psi}_{1pq} \\ & + j [E_{t02}^{TM} \vec{\Psi}_2 + \frac{1}{\sqrt{A}} \sum_{n=1}^N \alpha_n \sum_{p=-\infty}^{\infty} \sum_{q=-\infty}^{\infty} (t_3 < \vec{l}_n, \vec{\Psi}_{1pq} > + t_4 < \vec{l}_n, \vec{\Psi}_{2pq} >) \vec{\Psi}_{2pq}] \} \end{aligned} \quad (3.53)$$

The scattered fields for TE incidence can also be written similar to TM wave incidence such as,

In dielectric region, ($z < 0$)

$$\vec{E}_1 = \sum_{i=1}^2 \sum_p \sum_q j^{i-1} E_{1pq}^{(i)} e^{jY_{pq}z} \vec{\Psi}_{1pq} \quad (3.54a)$$

$$\vec{H}_1 = -\vec{a}_z \times \sum_{i=1}^2 \sum_p \sum_q j^{i-1} Y_{pq}^{(i)} E_{1pq}^{(i)} e^{jY_{pq}z} \vec{\Psi}_{1pq} \quad (3.54b)$$

$$\text{where} \quad \vec{\Psi}_{ipq} = \frac{1}{\sqrt{A}} e^{-jk_{Tpq} \cdot \vec{r}} \vec{e}_{ipq}, \quad i=1 \text{ or } 2.$$

$$\vec{e}_{1pq} = \vec{a}_z \times \vec{u}_{2pq}, \quad \text{TE modes (i=1)}$$

$$\vec{e}_{2pq} = \frac{\vec{k}_{Tpq}}{|\vec{k}_{Tpq}|}, \quad \text{TM modes (i=2)}$$

inside the chiral slab, ($0 < z < d$)

$$\vec{E}_2 = \sum_{i=1}^2 \sum_p \sum_q j^{i-1} (-1)^i C_{Lpq}^{(i)} e^{-jY_{Lpq}z} + C_{Rpq}^{(i)} e^{-jY_{Rpq}z} \vec{\Psi}_{1pq} \quad (3.55a)$$

$$\vec{E}_2^- = \sum_{i=1}^2 \sum_p \sum_q (-j)^{i-1} ((-1)^j D_{Lpq}^{(i)} e^{j\gamma_{Lpq} z} + D_{Rpq}^{(i)} e^{j\gamma_{Rpq} z}) \vec{\Psi}_{ipq} \quad (3.55b)$$

$$\vec{H}_2^+ = \vec{a}_z \times \sum_{i=1}^2 \sum_p \sum_q j^{i-1} ((-1)^j Y_{Lpq}^{(i)} C_{Lpq}^{(i)} e^{-j\gamma_{Lpq} z} + Y_{Rpq}^{(i)} C_{Rpq}^{(i)} e^{-j\gamma_{Rpq} z}) \vec{\Psi}_{ipq} \quad (3.56a)$$

$$\vec{H}_2^- = -\vec{a}_z \times \sum_{i=1}^2 \sum_p \sum_q (-j)^{i-1} ((-1)^j Y_{Lpq}^{(i)} D_{Lpq}^{(i)} e^{j\gamma_{Lpq} z} + Y_{Rpq}^{(i)} D_{Rpq}^{(i)} e^{j\gamma_{Rpq} z}) \vec{\Psi}_{ipq} \quad (3.56b)$$

for $z > d$,

$$\vec{E}_3 = \sum_{i=1}^2 \sum_p \sum_q j^{i-1} E_{3pq}^{(i)} e^{-j\gamma_{pq}(z-d)} \vec{\Psi}_{ipq} \quad (3.57a)$$

$$\vec{H}_3 = \vec{a}_z \times \sum_{i=1}^2 \sum_p \sum_q j^{i-1} Y_{pq}^{(i)} E_{3pq}^{(i)} e^{-j\gamma_{pq}(z-d)} \vec{\Psi}_{ipq} \quad (3.57b)$$

where $i=1,2$. $i=1$ represents for TE component and $i=2$ represents for TM component. Applying the same boundary conditions given in TM incidence case , reflected and transmitted electric fields can be obtained for TE incidence case as;

$$E_{tpq1}^{TE} = (-1)^j C_{Lpq}^{(i)} + C_{Rpq}^{(i)} - D_{Lpq}^{(i)} + (-1)^{j-1} D_{Rpq}^{(i)} \quad (3.58)$$

$$E_{tpq2}^{TE} = (-1)^j C_{Lpq}^{(i)} e^{-j\gamma_{Lpq} d} + C_{Rpq}^{(i)} e^{-j\gamma_{Rpq} d} - D_{Lpq}^{(i)} e^{j\gamma_{Lpq} d} + (-1)^{j-1} D_{Rpq}^{(i)} e^{j\gamma_{Rpq} d} \quad (3.59)$$

where

$$\begin{bmatrix} D_{Lpq} \\ D_{Rpq} \end{bmatrix} = \frac{1}{a} \begin{bmatrix} a_1 & a_2 \\ a_3 & a_4 \end{bmatrix} \begin{bmatrix} C_{Lpq} \\ C_{Rpq} \end{bmatrix}, \quad \begin{bmatrix} C_{Lpq} \\ C_{Rpq} \end{bmatrix} = \frac{1}{b} \begin{bmatrix} b_1 & b_2 \\ b_3 & b_4 \end{bmatrix} \begin{bmatrix} E_{tpq1}^{TE} \\ E_{tpq2}^{TE} \end{bmatrix}$$

$$\begin{bmatrix} E_{tpq1}^{TE} \\ E_{tpq2}^{TE} \end{bmatrix} = \frac{1}{c} \begin{bmatrix} c_1 & c_2 \\ c_3 & c_4 \end{bmatrix} \begin{bmatrix} I_{1pq} \\ I_{2pq} \end{bmatrix}, \quad \begin{bmatrix} E_{tpq1}^{TE} \\ E_{tpq2}^{TE} \end{bmatrix} = \begin{bmatrix} s_1 & s_2 \\ s_3 & s_4 \end{bmatrix} \frac{1}{b} \begin{bmatrix} b_1 & b_2 \\ b_3 & b_4 \end{bmatrix} \frac{1}{c} \begin{bmatrix} c_1 & c_2 \\ c_3 & c_4 \end{bmatrix} \begin{bmatrix} I_{1pq} \\ I_{2pq} \end{bmatrix}$$

$$a = (Y^{(1)} + Y_L^{(1)})(Y^{(2)} + Y_R^{(2)})Y_R^{(1)} + (Y^{(2)} + Y_L^{(2)})(Y^{(1)} + Y_R^{(1)})Y_R^{(1)}$$

$$a_1 = [(Y_L^{(1)} - Y^{(1)})(Y^{(2)} + Y_R^{(2)})Y_R^{(1)} + (Y^{(2)} - Y_L^{(2)})(Y^{(1)} + Y_R^{(1)})Y_L^{(1)}]e^{-j2\gamma_L d}$$

$$a_2 = [(Y^{(1)} - Y_R^{(1)})(Y_R^{(2)} + Y^{(2)}) + (Y^{(1)} + Y_R^{(1)})(Y^{(2)} - Y_R^{(2)})]Y_R^{(1)}e^{-j2(\gamma_L + \gamma_R)d}$$

$$a_3 = [(Y^{(1)} - Y_L^{(1)})(Y_L^{(2)} + Y^{(2)}) + (Y^{(1)} + Y_L^{(1)})(Y^{(2)} - Y_L^{(2)})]Y_L^{(1)}e^{-j2(\gamma_L + \gamma_R)d}$$

$$a_4 = [(Y_R^{(1)} - Y^{(1)})(Y^{(2)} + Y_L^{(2)})Y_L^{(1)} + (Y^{(2)} - Y_R^{(2)})(Y^{(1)} + Y_L^{(1)})Y_R^{(1)}]e^{-j2\gamma_R d}$$

$$b = (Y_L^{(1)} - Y_L^{(1)}u_1 - Y_R^{(1)}u_3)(1 - u_2 + u_4) + (1 + u_1 - u_3)(Y_R^{(1)} - Y_L^{(1)}u_2 - Y_R^{(1)}u_4)$$

$$b_1 = Y_c(1 - u_2 + u_4) \quad , \quad b_2 = -Y_R^{(1)} + Y_L^{(1)}u_2 + Y_R^{(1)}u_4$$

$$b_3 = Y_c(1 + u_1 - u_3) \quad , \quad b_4 = Y_L^{(1)} - Y_L^{(1)}u_1 - Y_R^{(1)}u_3$$

$$c = c_1 c_4 - c_2 c_3$$

$$c_1 = j[b_2(Y_L^{(1)} - Y_L^{(1)}u_1 + Y_R^{(1)}u_3) + b_4(-Y_R^{(1)} - Y_L^{(1)}u_2 + Y_R^{(1)}u_4) - Y^{(1)}]$$

$$c_2 = -[Y_c b_2(1 + u_1 + u_3) + Y_c b_4(1 + u_2 + u_4)]$$

$$c_3 = -j[b_1(Y_L^{(1)} - Y_L^{(1)}u_1 + Y_R^{(1)}u_3) + b_3(-Y_R^{(1)} - Y_L^{(1)}u_2 + Y_R^{(1)}u_4)]$$

$$c_4 = [Y_c b_1(1 + u_1 + u_3) + Y_c b_3(1 + u_2 + u_4) + Y^{(2)}]$$

$$s_1 = \frac{1}{Y_c} [Y_L^{(1)}e^{-j\gamma_L d} - \frac{1}{a}(Y_L^{(1)}a_1e^{j\gamma_L d} + Y_R^{(1)}a_3e^{j\gamma_R d})]$$

$$s_2 = \frac{1}{Y_c} [Y_R^{(1)}e^{-j\gamma_R d} - \frac{1}{a}(Y_L^{(1)}a_2e^{j\gamma_L d} + Y_R^{(1)}a_4e^{j\gamma_R d})]$$

$$s_3 = -e^{-j\gamma_L d} - \frac{1}{a}(a_1e^{j\gamma_L d} - a_3e^{j\gamma_R d}) \quad , \quad s_4 = e^{-j\gamma_R d} - \frac{1}{a}(a_2e^{j\gamma_L d} - a_4e^{j\gamma_R d})$$

$$C_{Lpq}^{(i)} = \left(\frac{Y_{Lpq}^{(i)}}{Y_c} \right)^{i-1} C_{Lpq} \quad , \quad C_{Rpq}^{(i)} = \left(\frac{Y_{Rpq}^{(i)}}{Y_c} \right)^{i-1} C_{Rpq}$$

$$D_{Lpq}^{(i)} = \left(\frac{Y_{Lpq}^{(i)}}{Y_c} \right)^{i-1} D_{Lpq} \quad , \quad D_{Rpq}^{(i)} = \left(\frac{Y_{Rpq}^{(i)}}{Y_c} \right)^{i-1} D_{Rpq}$$

$$Y_{Lpq}^{(2)} = Y_c \frac{k_L}{\gamma_{Lpq}} \quad , \quad Y_{Rpq}^{(2)} = Y_c \frac{k_R}{\gamma_{Rpq}} \quad , \quad Y_{pq}^{(2)} = Y \frac{k}{\gamma_{pq}}$$

$$Y_{Lpq}^{(i)} = Y_c \frac{\gamma_{Lpq}}{k_L} \quad , \quad Y_{Rpq}^{(i)} = Y_c \frac{\gamma_{Rpq}}{k_R} \quad , \quad Y_{pq}^{(i)} = Y \frac{\gamma_{pq}}{k}$$

$$(E_{ro}^{TE} + E_{ro1}^{TE}) \langle \bar{I}_k, \bar{\Psi}_1^* \rangle + j E_{ro2}^{TE} \langle \bar{I}_k, \bar{\Psi}_2^* \rangle = -\frac{1}{A} \sum_{n=1}^N \alpha_n \sum_q \sum_p [$$

$$(\tau_1 \langle \bar{I}_n, \bar{\Psi}_{1pq} \rangle + \tau_2 \langle \bar{I}_n, \bar{\Psi}_{2pq} \rangle) \langle \bar{I}_k, \bar{\Psi}_{1pq}^* \rangle$$

$$+ j (\tau_3 \langle \bar{I}_n, \bar{\Psi}_{1pq} \rangle + \tau_4 \langle \bar{I}_n, \bar{\Psi}_{2pq} \rangle) \langle \bar{I}_k, \bar{\Psi}_{2pq}^* \rangle] \quad (3.60)$$

Equation (3.60) is a matrix equation for the unknown coefficients of the current expansion. Upon finding the unknown coefficients α_n by complex matrix inversion we can find the total reflected field at $z=0$ as,

$$\bar{E}_r = \{ E_{ro1}^{TE} \bar{\Psi}_1 + \frac{1}{\sqrt{A}} \sum_{n=1}^N \alpha_n \sum_{p=-\infty}^{\infty} \sum_{q=-\infty}^{\infty} (\tau_1 \langle \bar{I}_n, \bar{\Psi}_{1pq} \rangle + \tau_2 \langle \bar{I}_n, \bar{\Psi}_{2pq} \rangle) \bar{\Psi}_{1pq}$$

$$+ j [E_{ro2}^{TE} \bar{\Psi}_2 + \frac{1}{\sqrt{A}} \sum_{n=1}^N \alpha_n \sum_{p=-\infty}^{\infty} \sum_{q=-\infty}^{\infty} (\tau_3 \langle \bar{I}_n, \bar{\Psi}_{1pq} \rangle + \tau_4 \langle \bar{I}_n, \bar{\Psi}_{2pq} \rangle) \bar{\Psi}_{2pq} \} \quad (3.61)$$

We can also find the transmitted field at $z=d$,

$$\bar{E}_t = \{ E_{to1}^{TE} \bar{\Psi}_1 + \frac{1}{\sqrt{A}} \sum_{n=1}^N \alpha_n \sum_{p=-\infty}^{\infty} \sum_{q=-\infty}^{\infty} (\tau_1 \langle \bar{I}_n, \bar{\Psi}_{1pq} \rangle + \tau_2 \langle \bar{I}_n, \bar{\Psi}_{2pq} \rangle) \bar{\Psi}_{1pq}$$

$$+ j [E_{to2}^{TE} \bar{\Psi}_2 + \frac{1}{\sqrt{A}} \sum_{n=1}^N \alpha_n \sum_{p=-\infty}^{\infty} \sum_{q=-\infty}^{\infty} (\tau_3 \langle \bar{I}_n, \bar{\Psi}_{1pq} \rangle + \tau_4 \langle \bar{I}_n, \bar{\Psi}_{2pq} \rangle) \bar{\Psi}_{2pq} \} \quad (3.62)$$

CHAPTER 4

SOLUTION BY MOMENT METHOD

4.1 Calculation of Inner Products

The meander - line array is a two dimensional periodic array as shown in Figure 3.1. The assumption here is that the strips are infinitely thin and perfectly conducting in the x-y plane.

Consider the periodic unit cell as consisting of five branches, three horizontal and two vertical as shown in Figure 4.1. Each branch is divided into small segments along the x and y axes, the current being unknown over each segments. Branches 1 and 5 are divided into n_1 segments (n_1 is even number) along the x-axis, branches 2 and 4 are divided into n_2 segments along the y-axis and branch 3 is divided into n_3 segments along the x-axis, totally $n_1 + 2n_2 + n_3$ segments per unit cell.

As previously explained, matching the boundary conditions combined with the orthogonality property of the Floquet modes over a single periodic unit cell leads to an integral equation for the unknown induced current density $\vec{J}=(x,y)$ on the conducting strips. This integral equation can be solved by using the Moment-method [33], by expressing the unknown current density in terms of a set of basis functions with unknown coefficients and testing it with the same basis function. We will assume that the expansion functions are a set of orthogonal pulse functions over each segment and the strips are narrow enough with respect to wavelength in order to neglect the current component that is parallel to the width of the strip.

The current density function can be expanded into a finite series with unknown coefficients α_n as,

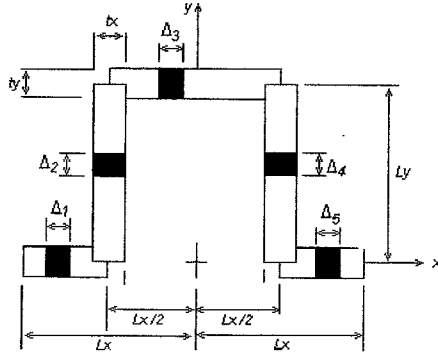


Figure 4.1 Subdivision of the periodic unit cell of meander – line

$$\vec{J} = \sum_{n=1}^N \alpha_n \vec{I}_n(x, y) \quad (4.1)$$

In order to derive an integral equation for the moment method one can insert,

$$\vec{\Psi}_{mpq} = e^{-j\vec{k}_{mpq} \cdot \vec{r}} \vec{e}_{mpq} = e^{-j(k_x x + k_y y)} \vec{e}_{mpq} \quad (4.2)$$

$$\vec{e}_{1pq} = \vec{a}_x \cos \phi + \vec{a}_y \sin \phi, \quad \vec{e}_{2pq} = -\vec{a}_x \cos \phi + \vec{a}_y \sin \phi$$

into equation,

$$\langle \vec{I}_n, \vec{\Psi}_{mpq} \rangle = \iint \vec{I}_n(x, y) \vec{\Psi}_{mpq} dx dy \quad (4.3)$$

that is,

$$\langle \vec{I}_n, \vec{\Psi}_{mpq} \rangle = \iint (\vec{a}_x I_x + \vec{a}_y I_y) (\vec{a}_x e_x + \vec{a}_y e_y) e^{-j(k_x x + k_y y)} dx dy \quad (4.4)$$

where e_x and e_y are the x and y components of the \vec{e}_{mpq} ,

Inner products for each branch derived separately. The length of the branch 1 and 5 is $L/2$ and it is divided into n_1 segments ($n_1/2$ segments for branch 1 and $n_1/2$ segments for branch 5 that's why n_1 is chosen even number) as shown in Figure 4.1. For the first segment in branch 1 the inner product can be written as,

$$\langle \bar{I}_n, \bar{\Psi}_{mpq} \rangle = \int_{-L_x}^{-L_x + \Delta_1} \int_{-\frac{t_y}{2}}^{\frac{t_y}{2}} (I_x e_x + I_y e_y) e^{-j(k_x x + k_y y)} dx dy \quad (4.5)$$

since the y component of current coefficient is zero on branch 1 and x component of current, I_x is equal to unity due to selection of pulse functions.

Therefore the inner product for the n-th segment of branch 1;

$$\begin{aligned} \langle \bar{I}_n, \bar{\Psi}_{mpq} \rangle &= e_x \int_{-L_x + (n_1 - 1)\Delta_1}^{-L_x + n_1\Delta_1} \int_{-\frac{t_y}{2}}^{\frac{t_y}{2}} e^{j(k_x x + k_y y)} dx dy = \frac{e_x}{-k_x k_y} 2 \sin\left(\frac{k_y t_y}{2}\right) \{ \\ &\sin((-L_x + n_1\Delta_1)k_x) - \sin((-L_x + (n_1 - 1)\Delta_1)k_x) \\ &-j[\cos((-L_x + n_1\Delta_1)k_x) - \cos((-L_x + (n_1 - 1)\Delta_1)k_x)] \} \quad (4.6) \end{aligned}$$

$$\begin{aligned} \langle \bar{I}_n, \bar{\Psi}_{mpq}^* \rangle &= e_x \int_{-L_x + (n_1 - 1)\Delta_1}^{-L_x + n_1\Delta_1} \int_{-\frac{t_y}{2}}^{\frac{t_y}{2}} e^{-j(k_x x + k_y y)} dx dy = \frac{e_x}{k_x k_y} 2 \sin\left(\frac{k_y t_y}{2}\right) \{ \\ &\sin(-L_x + n_1\Delta_1)k_x - \sin(-L_x + (n_1 - 1)\Delta_1)k_x \\ &+j[\cos(-L_x + n_1\Delta_1)k_x - \cos(-L_x + (n_1 - 1)\Delta_1)k_x] \} \quad (4.7) \end{aligned}$$

For branches 2 and 4, the length of the branches is L_y it is divided into n_2 segments with the length of each segment taken as Δ_2 , as shown in Figure 4.1. The inner product for first segment of branch 2 can be written as,

$$\begin{aligned} \langle \bar{I}_n, \bar{\Psi}_{mpq} \rangle &= \int_{\frac{L_x - t_x}{2}}^{\frac{L_x - t_x}{2}} \int_0^{\Delta_2} (\bar{I}_x e_x + \bar{I}_y e_y) e^{j(k_x x + k_y y)} dx dy \\ \langle \bar{I}_n, \bar{\Psi}_{mpq} \rangle &= e_y \int_{\frac{L_x - t_x}{2}}^{\frac{L_x - t_x}{2}} \int_0^{\Delta_2} e^{-j(k_x x + k_y y)} dx dy \end{aligned} \quad (4.8)$$

since the width of the branch 2 is narrow enough with respect to wavelength therefore we can neglect the x component of the current. The inner product for branch 2 can be written as ,

$$\begin{aligned} \langle \bar{I}_n, \bar{\Psi}_{mpq} \rangle &= e_y \int_{\frac{L_x - t_x}{2}}^{\frac{L_x - t_x}{2}} \int_{(n_2 - 1)\Delta_2}^{n_2 \Delta_2} e^{j(k_x x + k_y y)} dx dy = \frac{e_y}{k_x k_y} 2 \sin\left(\frac{k_x t_x}{2}\right) \{ \\ &\sin(k_y n_2 \Delta_2 - \frac{k_x L_x}{2}) - \sin(k_y (n_2 - 1)\Delta_2 - \frac{k_x L_x}{2}) \\ &-j[\cos(k_y n_2 \Delta_2 - \frac{k_x L_x}{2}) - \cos(k_y (n_2 - 1)\Delta_2 - \frac{k_x L_x}{2})] \} \end{aligned} \quad (4.9)$$

$$\begin{aligned} \langle \bar{I}_n, \bar{\Psi}_{mpq}^* \rangle &= e_y \int_{\frac{L_x - t_x}{2}}^{\frac{L_x - t_x}{2}} \int_{(n_2 - 1)\Delta_2}^{n_2 \Delta_2} e^{-j(k_x x + k_y y)} dx dy = \frac{e_y}{k_x k_y} 2 \sin\left(\frac{k_x t_x}{2}\right) \{ \\ &-\sin(\frac{k_x L_x}{2} - k_y n_2 \Delta_2) + \sin(\frac{k_x L_x}{2} - k_y (n_2 - 1)\Delta_2) \\ &+j[\cos(\frac{k_x L_x}{2} - k_y n_2 \Delta_2) - \cos(\frac{k_x L_x}{2} - k_y (n_2 - 1)\Delta_2)] \} \end{aligned} \quad (4.10)$$

In the light of the explanations given above the inner products for branches 3, 4 and 5 can be written as follows ;

For branch 3,

$$\begin{aligned} \langle \bar{I}_n, \bar{\Psi}_{mpq} \rangle &= e_x \int_{-\frac{L_x}{2} + n_3 \Delta_3}^{\frac{L_x}{2} + n_3 \Delta_3} \int_{L_y - \frac{t_y}{2}}^{L_y + \frac{t_y}{2}} e^{j(k_x x + k_y y)} dx dy = \frac{e_x}{k_x k_y} 2 \sin\left(\frac{k_y t_y}{2}\right) \{ \\ &\sin(k_y L_y + k_x(n_3 \Delta_3 - \frac{L_x}{2})) - \sin(k_y L_y + k_x((n_3 - 1)\Delta_3 - \frac{L_x}{2})) \\ &-j[\cos(k_y L_y + k_x(n_3 \Delta_3 - \frac{L_x}{2})) - \cos(k_y L_y + k_x(n_3 \Delta_3 - \frac{L_x}{2}))] \} \quad (4.11) \end{aligned}$$

$$\begin{aligned} \langle \bar{I}_n, \Psi_{mpq}^* \rangle &= e_x \int_{-\frac{L_x}{2} + (n_3 - 1)\Delta_3}^{\frac{L_x}{2} + n_3 \Delta_3} \int_{L_y - \frac{t_y}{2}}^{L_y + \frac{t_y}{2}} e^{-j(k_x x + k_y y)} dx dy = \frac{e_x}{k_x k_y} 2 \sin\left(\frac{k_y t_y}{2}\right) \{ \\ &\sin(k_y L_y + k_x(n_3 \Delta_3 - \frac{L_x}{2})) - \sin(k_y L_y + k_x((n_3 - 1)\Delta_3 - \frac{L_x}{2})) \\ &+j[\cos(k_y L_y + k_x(n_3 \Delta_3 - \frac{L_x}{2})) - \cos(k_y L_y + k_x(n_3 \Delta_3 - \frac{L_x}{2}))] \} \quad (4.12) \end{aligned}$$

For branch 4 ,

$$\begin{aligned} \langle \bar{I}_n, \bar{\Psi}_{mpq} \rangle &= e_y \int_{\frac{L_x - t_x}{2}}^{\frac{L_x + t_x}{2}} \int_{L_y - (n_4 - 1)\Delta_4}^{L_y - n_4 \Delta_4} e^{j(k_x x + k_y y)} dx dy = \frac{e_y}{k_x k_y} 2 \sin\left(\frac{k_x t_x}{2}\right) \{ \\ &\sin(k_y(L_y - n_4 \Delta_4) + \frac{k_x L_x}{2}) - \sin(k_y(L_y - (n_4 - 1)\Delta_4) + \frac{k_x L_x}{2}) \\ &-j[\cos(k_y(L_y - n_4 \Delta_4) + \frac{k_x L_x}{2}) - \cos(k_y(L_y - (n_4 - 1)\Delta_4) + \frac{k_x L_x}{2})] \} \quad (4.13) \end{aligned}$$

$$\begin{aligned} \langle \bar{I}_n, \bar{\Psi}_{mpq}^* \rangle &= e_y \int_{\frac{L_x - t_x}{2}}^{\frac{L_x + t_x}{2}} \int_{L_y - (n_4 - 1)\Delta_4}^{L_y - n_4 \Delta_4} e^{-j(k_x x + k_y y)} dx dy = \frac{e_y}{k_x k_y} 2 \sin\left(\frac{k_x t_x}{2}\right) \{ \\ &\sin(k_y(L_y - n_4 \Delta_4) + \frac{k_x L_x}{2}) - \sin(k_y(L_y - (n_4 - 1)\Delta_4) + \frac{k_x L_x}{2}) \end{aligned}$$

$$+j[\cos(k_y(L_y - n_4\Delta_4) + \frac{k_x L_x}{2}) - \cos(L_y - (n_4 - 1)\Delta_4) + \frac{k_x L_x}{2}]] \quad (4.14)$$

For branch 5,

$$\begin{aligned} \langle \vec{I}_n, \vec{\Psi}_{mpq}^* \rangle = e_x \int_{\frac{L_x}{2} + (n_5 - 1)\Delta_5}^{\frac{L_x}{2} + n_5\Delta_5} \int_{-\frac{t_y}{2}}^{\frac{t_y}{2}} e^{j(k_x x + k_y y)} dx dy = \frac{e_x}{k_x k_y} 2 \sin\left(\frac{k_y t_y}{2}\right) \{ \\ \sin\left(\frac{L_x}{2} + n_5\Delta_5\right)k_x - \sin\left(\frac{L_x}{2} + (n_5 - 1)\Delta_5\right)k_x \\ -j[\cos\left(\frac{L_x}{2} + n_{s1}\Delta_5\right)k_x - \cos\left(\frac{L_x}{2} + (n_{s1} - 1)\Delta_5\right)k_x]\} \quad (4.15) \end{aligned}$$

$$\begin{aligned} \langle \vec{I}_n, \vec{\Psi}_{mpq}^* \rangle = e_x \int_{\frac{L_x}{2} + (n_5 - 1)\Delta_5}^{\frac{L_x}{2} + n_5\Delta_5} \int_{-\frac{t_y}{2}}^{\frac{t_y}{2}} e^{-j(k_x x + k_y y)} dx dy = \frac{e_x}{k_x k_y} 2 \sin\left(\frac{k_y t_y}{2}\right) \{ \\ \sin\left(\frac{L_x}{2} + n_5\Delta_5\right)k_x - \sin\left(\frac{L_x}{2} + (n_5 - 1)\Delta_5\right)k_x \\ +j[\cos\left(\frac{L_x}{2} + n_{s1}\Delta_5\right)k_x - \cos\left(\frac{L_x}{2} + (n_{s1} - 1)\Delta_5\right)k_x]\} \quad (4.16) \end{aligned}$$

Choosing proper floquet mode p, q values and using the above inner products the equation (3.51), (3.60) can be rewritten in matrix form as follows for TM and TE excitations respectively.

$$[\mathbf{V}_n^{\text{TM}}] = [\mathbf{Z}_{kn}^{\text{TM}}] [\alpha_n^{\text{TM}}] \quad (4.17)$$

$$[\mathbf{V}_n^{\text{TE}}] = [\mathbf{Z}_{kn}^{\text{TE}}] [\alpha_n^{\text{TE}}] \quad (4.18)$$

where \mathbf{V}_n 's are source matrix, \mathbf{Z}_{kn} impedance matrix and α_n current coefficient to be found.

$$[\mathbf{V}_n^{\text{TM}}] = (\mathbf{E}_o^{\text{TM}} + \mathbf{E}_{ro}^{\text{TM}}) \langle \vec{I}_n, \vec{\Psi}_1^* \rangle + j\mathbf{E}_{ro}^{\text{TE}} \langle \vec{I}_n, \vec{\Psi}_2^* \rangle \quad (4.19)$$

$$[V_n^{TE}] = (E_o^{TE} + E_{ro}^{TE}) < \bar{I}_n, \bar{\Psi}_1^* > + j E_{ro}^{TM} < \bar{I}_n, \bar{\Psi}_2^* > \quad (4.20)$$

$$[Z_{kn}^{TM}] = -\frac{1}{A} \sum_p \sum_q [(r_1 < \bar{I}_n, \bar{\Psi}_{1pq} > + r_2 < \bar{I}_n, \bar{\Psi}_{2pq} >)] < \bar{I}_k, \bar{\Psi}_{1pq}^* > \\ + j (r_3 < \bar{I}_n, \bar{\Psi}_{1pq} > + r_4 < \bar{I}_n, \bar{\Psi}_{2pq} >)] < \bar{I}_k, \bar{\Psi}_{2pq}^* > \quad (4.21)$$

$$[Z_{kn}^{TE}] = -\frac{1}{A} \sum_q \sum_p [(r_1 < \bar{I}_n, \bar{\Psi}_{1pq} > + r_2 < \bar{I}_n, \bar{\Psi}_{2pq} >)] < \bar{I}_k, \bar{\Psi}_{1pq}^* > \\ + j (r_3 < \bar{I}_n, \bar{\Psi}_{1pq} > + r_4 < \bar{I}_n, \bar{\Psi}_{2pq} >)] < \bar{I}_k, \bar{\Psi}_{2pq}^* > \quad (4.22)$$

where $k = 1, 2, 3, \dots, N$

For the first row of the matrix, equation (4.17) and (4.18) one can write ,

$$V_1^{TM} = \alpha_1 \{ Z_{11}^{TM} + Z_{21}^{TM} + Z_{31}^{TM} + \dots + Z_{N1}^{TM} \} + \alpha_2 \{ Z_{12}^{TM} + Z_{22}^{TM} + Z_{32}^{TM} + \dots + Z_{N2}^{TM} \} + \\ \alpha_3 \{ Z_{13}^{TM} + Z_{23}^{TM} + Z_{33}^{TM} + \dots + Z_{N3}^{TM} \} + \dots + \alpha_N \{ Z_{1N}^{TM} + Z_{2N}^{TM} + Z_{3N}^{TM} + \dots + Z_{NN}^{TM} \}$$

$$V_1^{TE} = \alpha_1 \{ Z_{11}^{TE} + Z_{21}^{TE} + Z_{31}^{TE} + \dots + Z_{N1}^{TE} \} + \alpha_2 \{ Z_{12}^{TE} + Z_{22}^{TE} + Z_{32}^{TE} + \dots + Z_{N2}^{TE} \} + \\ \alpha_3 \{ Z_{13}^{TE} + Z_{23}^{TE} + Z_{33}^{TE} + \dots + Z_{N3}^{TE} \} + \dots + \alpha_N \{ Z_{1N}^{TE} + Z_{2N}^{TE} + Z_{3N}^{TE} + \dots + Z_{NN}^{TE} \}$$

$$V_1^{TM} = (E_o^{TM} + E_{ro}^{TM}) < \bar{I}_1, \bar{\Psi}_1^* > + j E_{ro}^{TE} < \bar{I}_1, \bar{\Psi}_2^* > \quad (4.23)$$

$$V_1^{TE} = (E_o^{TE} + E_{ro}^{TE}) < \bar{I}_1, \bar{\Psi}_1^* > + j E_{ro}^{TM} < \bar{I}_1, \bar{\Psi}_2^* > \quad (4.24)$$

Once the source vector is known and the elements of the impedance matrix are calculated then the unknown current coefficients, α_n can be found by inverting the complex matrix. After finding the current coefficients the reflected and transmitted powers can be found from the Equations (3.52) and (3.53) for TM excitations and from the Equations (3.61) and (3.62) for TE excitations using the Poynting vector.

4.2 Numerical Results of Meander-line Polarizer with Chiral Slab

In this section, the numerical results of power reflection and transmission characteristics of meander-line polarizer with chiral slab are presented. The effects of the chirality admittance, slab thickness and dielectric constant are analyzed. The power reflection and transmission coefficients have been plotted with respect to frequency and incidence angle for both type of linearly polarized TE and TM incident plane waves.

We assumed that the meander-line is two dimensional infinite array of perfectly conducting narrow (with respect to λ) strips having the dimensions; $d_1=5$ mm, $d_2=10$ mm, $L_u=L_x=2.5$ mm, $L_y=5$ mm, as shown in Figure 3.1, and $t_y=t_x=0.25$ mm, as shown in Figure 4.1. During the calculations different p, q values of the floquet mode numbers were tried and it was seen that $p=q=20$ gave the best result, where the sum of normalized power reflection and transmission coefficients were equal to unity.

To obtain a physically acceptable solution, the values of segments n_1, n_2 and n_3 have to be correctly determined for the fixed values of p and q . Therefore the critical value of n_2 can be obtained by the following relation [34];

$$n_2 = (2q + 1) \frac{L_y}{d_2}$$

In order to have the same length – segments the number of segments along x-axis is found as $n_1 = n_3 = n_2/2$ since the lengths of L_x and L_u are the halves of L_y in this case.

In Figures 4.2 to 4.4 and Figures 4.5 to 4.7 the different values of chirality admittance, slab thickness and dielectric constant with respect to frequency are shown for TE and TM polarization, respectively. In Figures 4.8 to 4.10 and Figures 4.11 to 4.13 different values of chirality admittance, slab thickness and dielectric constant with respect to incidence angle are shown.

In Figure 4.2 power reflection and transmission coefficients are obtained for different chirality admittances with slab thickness $d=6.25$ mm and relative permittivity $\epsilon_r=2.0$ for TE polarization. More resonances are obtained for co – polar power reflection coefficient. When the chirality admittance is increased the resonant frequency shifts to lower frequencies. The first resonance bandwidth is more narrow than the others. As chirality admittances increase the co – polar power transmission coefficients decrease and shift to lower frequencies. The first peak magnitudes of the cross–polar TM power transmission coefficients increase and shift to lower frequencies as chirality admittances increase. Approximately full transmission is obtained for $\xi=0.002$ and $\xi=0.003$ at 15.2 and 10.7 GHz, respectively.

In Figure 4.3 power reflection and transmission coefficients are obtained for different values of slab thickness with $\xi=0.003$ S and $\epsilon_r=2.0$. Two resonances are obtained for co – polar power reflection coefficient at $d=3.125$ mm. The first one is more narrow than the second one. When the slab thickness is increased the resonant frequencies shift to lower frequencies narrowing the bandwidth. The co–polar power transmission coefficient dramatically decreases for $d=3.125$ mm. For slab thickness of $d=6.25$ mm and $d=12.5$ mm more peaks are seen.

In Figure 4.4 power reflection and transmission coefficients are obtained for different dielectric constants with $\xi=0.003$ S and $d=6.25$ mm. As it can be seen from the figure four resonances exist for $\epsilon_r=2.0$. The first resonance bandwidth is more narrow than the higher order resonances. As ϵ_r is increased the resonant frequencies shift to lower frequencies. If the first resonances are compared a small increase in bandwidth is observed as ϵ_r is increased. The co – polar power transmission coefficient reduces as ϵ_r is increased up to 10 GHz. Approximately full transmission is observed for $\epsilon_r=4$ at the frequency of 20 GHz. The cross–polar power transmission coefficient has two peaks for $\epsilon_r=2$, that is close to unity. The first one is more wider than the second one. If ϵ_r is increased these two peaks are narrowed and their amplitudes are reduced for the first peak. For $\epsilon_r=6$ more peaks are seen.

In Figure 4.5 the power reflection and transmission coefficients are obtained for different values of chirality admittances with slab thickness $d=6.25$ mm and dielectric constant $\epsilon_r=2.0$ for TM incident wave. As shown in figure four different values of chirality admittance are chosen; $\xi=0$, $\xi=0.001$, $\xi=0.002$ and $\xi=0.003$ S. As it can be seen from the Figure 4.5.a, the power reflection coefficient is unity at the resonant frequency of 10 Ghz for four different values of chirality admittances. At resonant frequency the co – and cross – polar power transmission coefficients are zero. The co – polar power transmission coefficient decreases while the chirality admittance increases, but this is not true for $\xi=0.003$ S between 10 and 25 Ghz as shown in Figure 4.5.b. The cross – polar power transmission coefficient increases for increasing value of chirality admittance up to frequency of 10 Ghz. It has a unity at the frequency of 15.5 Ghz for $\xi=0.002$ S as shown in Figure 4.5.c.

In Figure 4.6 the power reflection and transmission coefficients are obtained for different values of slab thickness with chirality admittance $\xi=0.003$ S and dielectric constant $\epsilon_r=2.0$ for TM incident case. Three different values of slab thickness are selected; $d=3.125$ mm, $d=6.25$ mm, and $d=12.5$ mm. The variation of the slab thickness does not change the resonant frequency. The co – and cross – polar power transmission coefficients are zero at resonance frequency.

In Figure 4.7 power reflection and transmission coefficients are obtained for different dielectric constants with chirality admittance $\xi=0.003$ S and slab thickness $d=6.25$ mm for TM case. Three different values are chosen for the dielectric constants; $\epsilon_r=2.0$, $\epsilon_r=4.0$ and $\epsilon_r=6.0$. When the value of dielectric constant increases the resonant frequency shifts to lower frequencies and more resonances appear as seen in Figure 4.7a. The bandwidths of the first resonances are approximately the same for all dielectric constants. The co – polar power transmission coefficient is zero at 10 Ghz for three ϵ_r values. The cross – polar power transmission coefficient has two peaks for $\epsilon_r=2.0$ as shown in Figure 4.7.c. As the values of ϵ_r increase the amplitudes of first peaks decrease while the amplitude of second ones increase. For $\epsilon_r=4.0$ it has a unity around 11 Ghz.

In Figure 4.8 the power reflection and transmission coefficients against incidence angle θ are obtained for different chirality admittances with dielectric constant $\epsilon_r=9$, frequency $f=12$ Ghz and slab thickness $d=6.25$ mm ($\lambda/4$) for TE illumination. There is no Brewster angle for TE case for different values of chirality admittances. The co – polar power transmission coefficient decreases as chirality admittance increases up to $\xi=0.003$ S and an increase is observed for $\xi=0.006$ S up to 47° . The cross – polar power transmission coefficient is zero for $\xi=0$ and its amplitude increases for $\xi=0.001$ S and $\xi=0.003$ S. After that decreases for $\xi=0.006$ S. At 90° it is zero.

In Figure 4.9 power reflection and transmission coefficients against incidence angle θ are obtained for different values of slab thickness with chirality admittance $\xi=0.005$ S and dielectric constant $\epsilon_r=9$. The co – polar power reflection coefficient is nearly unity for $d=6.25$ mm ($\lambda/4$) up to 36° and a sharp decrease and then an oscillation is observed as shown in Figure 4.9.a. The co – polar power transmission coefficient is nearly zero for $d=3.125$ mm ($\lambda/8$). There is a sharp increase for $d=6.25$ mm ($\lambda/4$) around 36° as seen in Figure 4.9.b. The cross–polar power transmission coefficient is approximately zero for $d=12.5$ mm ($\lambda/2$) and $d=6.25$ mm ($\lambda/4$). There is a small peak for $d=\lambda/2$ at 80° and a wider peak is seen at about 45° for $d=\lambda/4$.

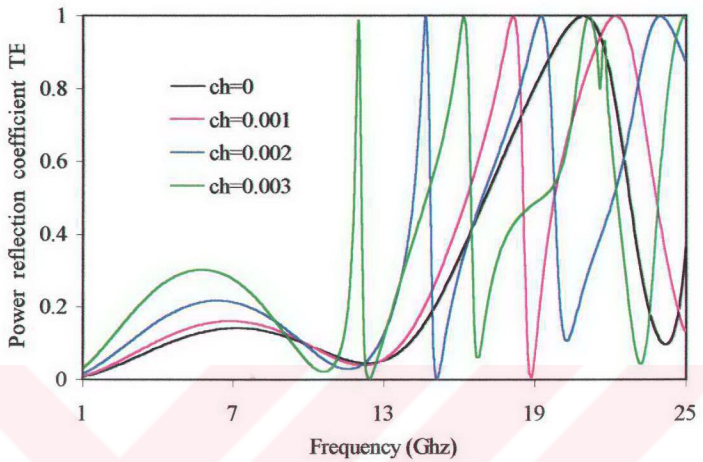
In Figure 4.10 power reflection and transmission coefficients against incidence angle are obtained for different values of dielectric constant with chirality admittance $\xi=0.005$ S and slab thickness $d=6.25$ mm for TE case. The reflection and transmission coefficients are oscillating between 0° and 80° .

In Figure 4.11 power reflection and transmission coefficients against incidence angle are obtained for different chirality admittances with dielectric constant $\epsilon_r=9.0$, frequency $f=12$ Ghz and slab thickness $d=6.25$ mm ($\lambda/4$) for TM illumination. There is a Brewster angle only for $\xi=0$ and $\xi=0.001$ S. The co – polar power reflection coefficient shifts towards to 90° with narrowing bandwidth and Brewster angle disappears for $\xi=0.003$ S. The bandwidth enlarges for $\xi=0.006$ S and the magnitude decreases. The co – polar power

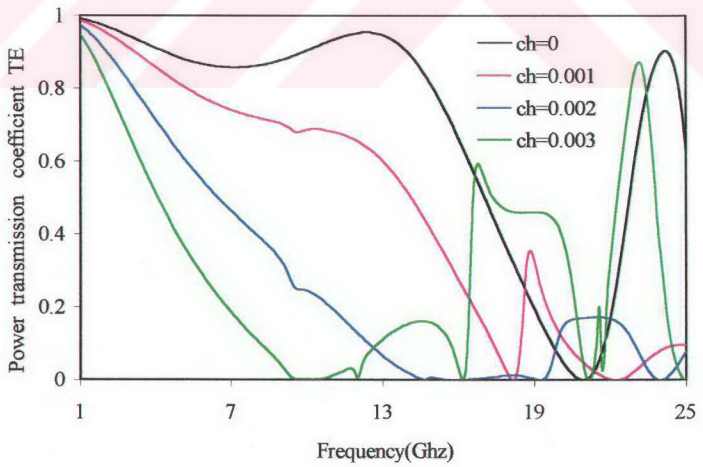
transmission coefficient has unity for only at 72° for $\xi=0$. Its magnitude decreases with narrowing bandwidth for increasing value of ξ up to $\xi=0.003$ S and then increases again for $\xi=0.006$ S. The cross – polar power transmission coefficient is oscillating for different value of chirality admittance ξ .

In Figure 4.12 power reflection and transmission coefficients against incidence angle are obtained for different values of slab thickness with chirality admittance $\xi=0.005$, dielectric constant $\epsilon_r=9.0$ and frequency $f=12$ Ghz for TM case. The Brewster angle only exist for the slab thickness of $d=\lambda/4$ at $\theta=76^\circ$ as shown in Figure 4.12.b. The co – polar power transmission coefficient is unity at $\theta=76^\circ$ for $d=\lambda/4$ and it is approximately reduced to zero for $d=\lambda/2$. The cross – polar power transmission coefficient is nearly zero for $d=\lambda/4$ and it is much greater for $d=\lambda/8$. As θ approaches 90° the cross – polar power transmission coefficient is dramatically reduced to zero as seen in Figure 4.12.c.

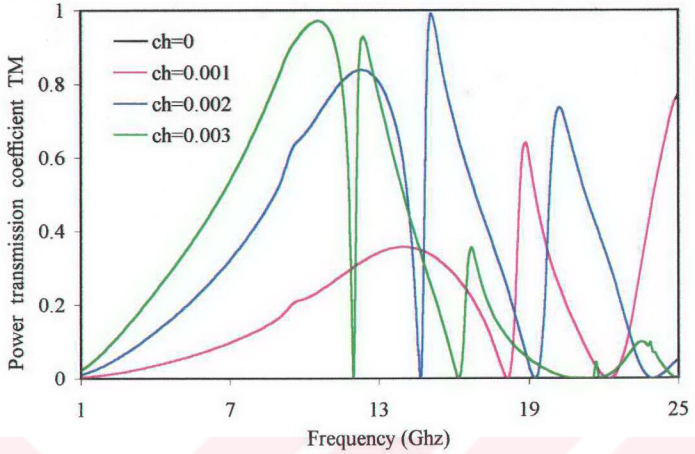
In Figure 4.13 power reflection and transmission coefficients against incidence angle are obtained for different values of dielectric constant with chirality admittance $\xi=0.005$ and slab thickness $d=6.25$ mm for TM case. There is a Brewster angle for all values of ϵ_r at $\theta=76^\circ$. After the Brewster angle the co – polar power reflection coefficient sharply increases and approaches unity as shown in Figure 4.13.a. The co – polar power transmission coefficient is unity at $\theta=76^\circ$ and sharply reduces to zero at 90° for four different value of ϵ_r . The cross – polar power transmission coefficient is so small for all values of ϵ_r and it has a small peak for $\epsilon_r=8$ at 7° .



(a)

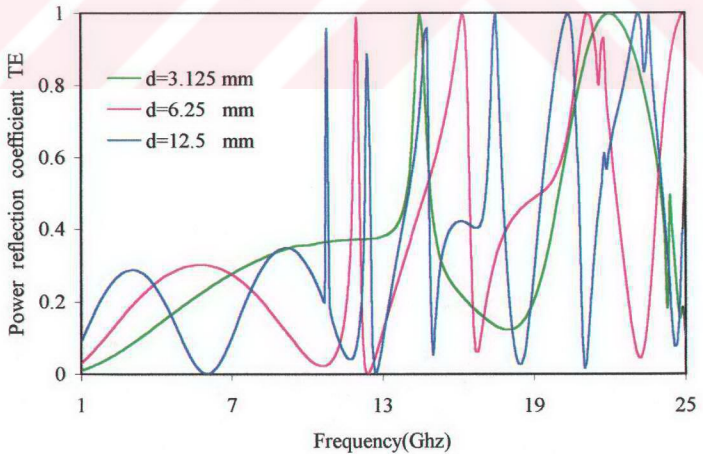


(b)

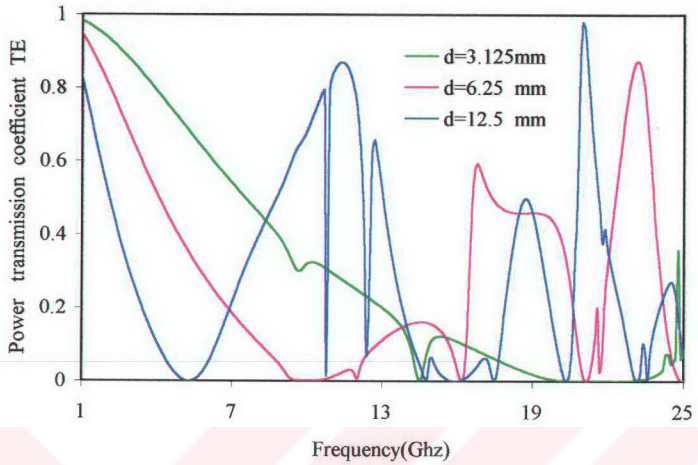


(c)

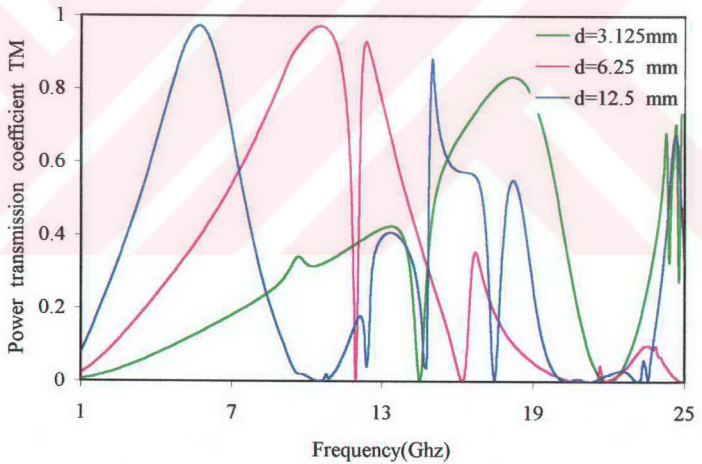
Figure 4.2. Normalized power reflection and transmission coefficients against frequency for different values of chirality admittances ; TE normal incidence , $\epsilon_r=2.0$ and $d=6.25$ mm. (a) – Power reflection coefficient TE ,(b)– Power transmission coefficient TE ,(c)–Power transmission coefficient TM.



(a)

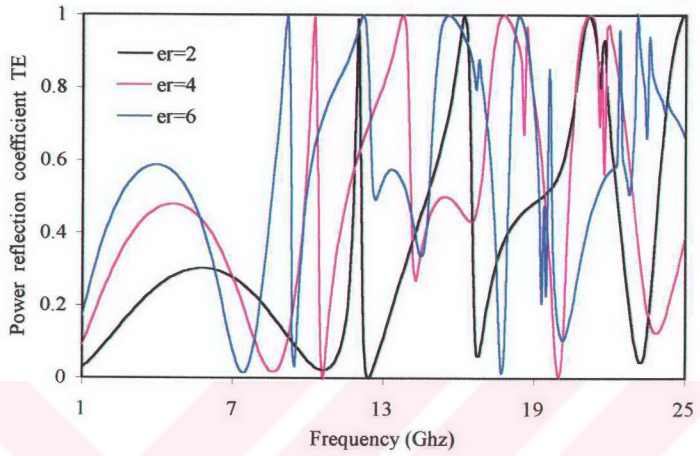


(b)

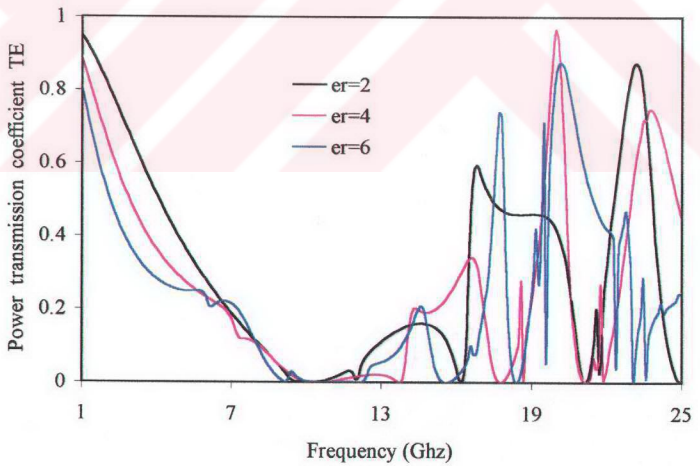


(c)

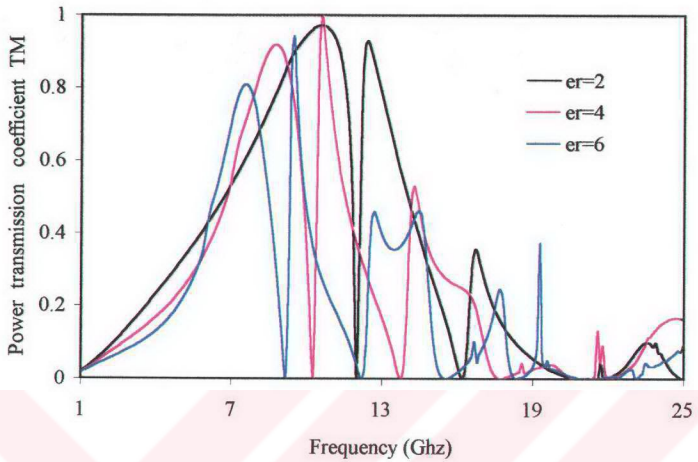
Figure 4.3. Normalized power reflection and transmission coefficients against frequency for different values of slab thickness; TE normal incidence, $\xi=0.003\text{ S}$ and $\epsilon_r=2$. (a) – Power reflection coefficient TE, (b) – Power transmission coefficient TE, (c) – Power transmission coefficient TM.



(a)

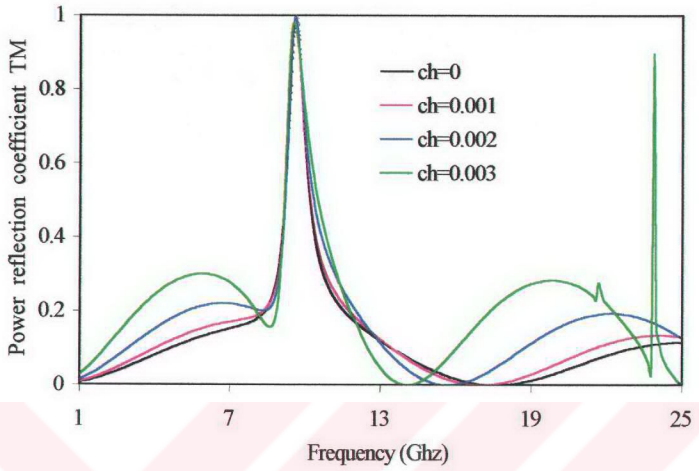


(c)

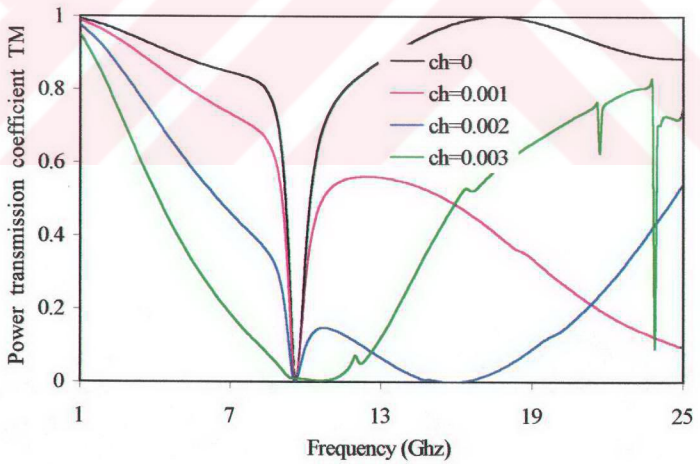


(c)

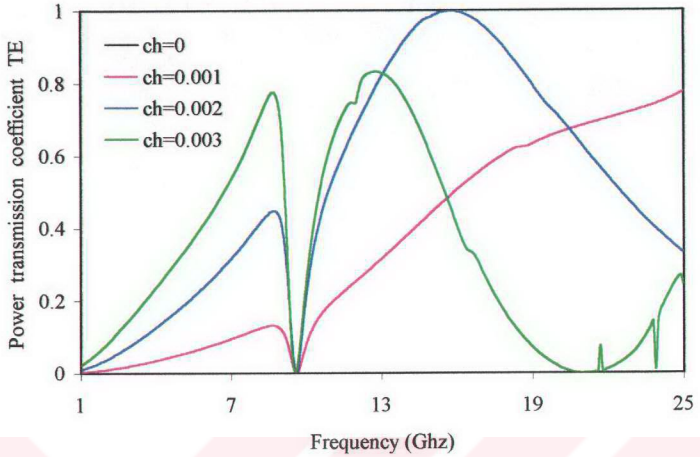
Figure 4.4. Normalized power reflection and transmission coefficients against frequency for different values of dielectric constant; TE normal incidence, $\xi=0.003$ S and $d=6.25$ mm. (a) – Power reflection coefficient TE, (b) – Power transmission coefficient TE, (c) – Power transmission coefficient TM.



(a)

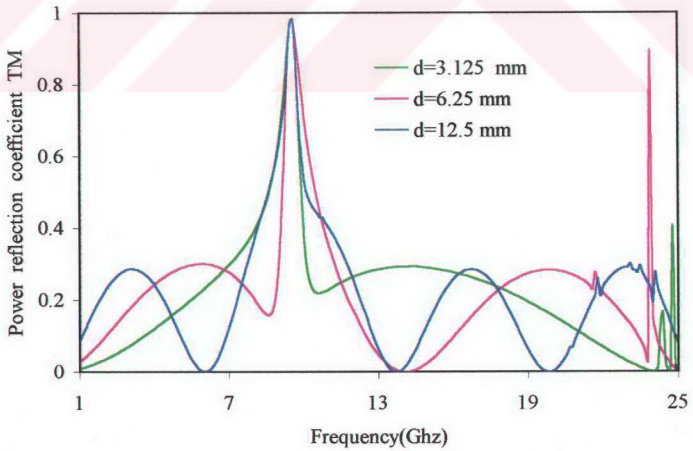


(b)

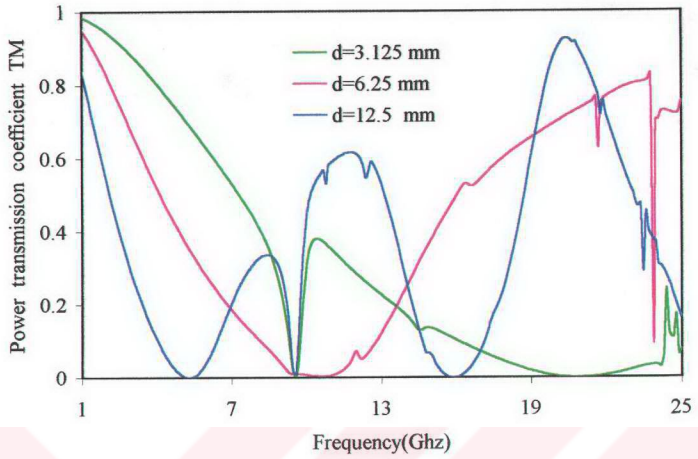


(c)

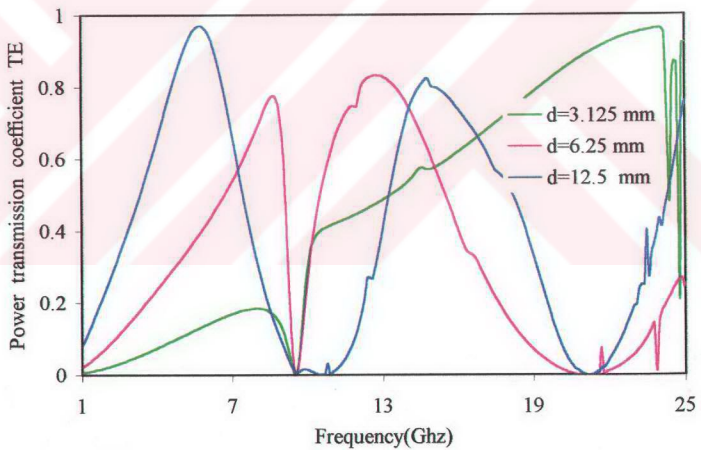
Figure 4.5. Normalized power reflection and transmission coefficients against frequency for different values of chirality admittances ; TM normal incidence, $d=6.25$ mm and $\epsilon_r=2.0$. (a)–Power reflection coefficient TM, (b)–Power transmission coefficient TM, (c)–Power transmission coefficient TE.



(a)

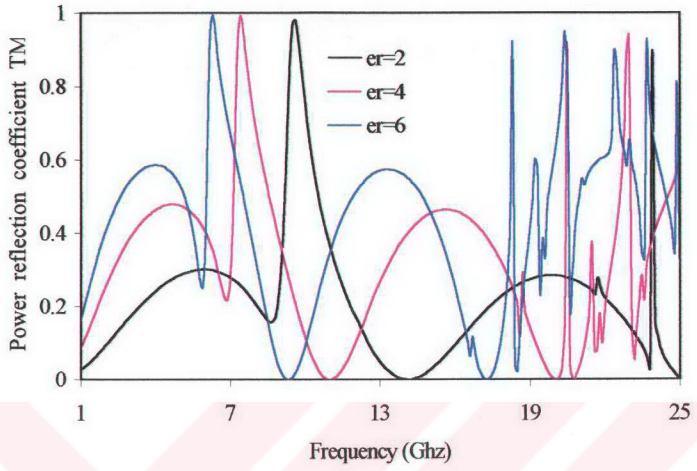


(b)

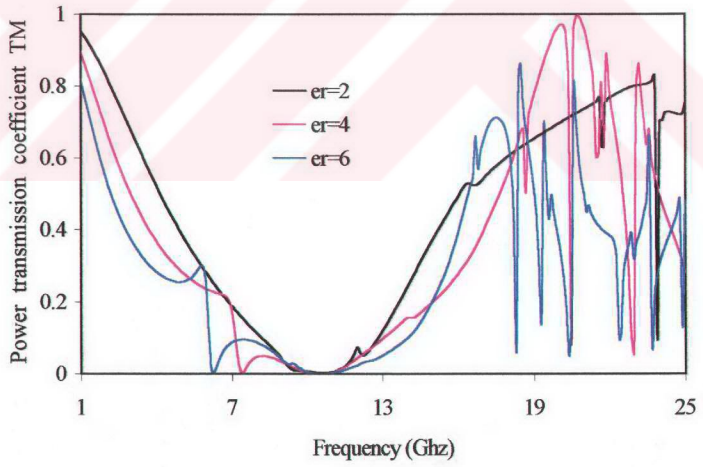


(c)

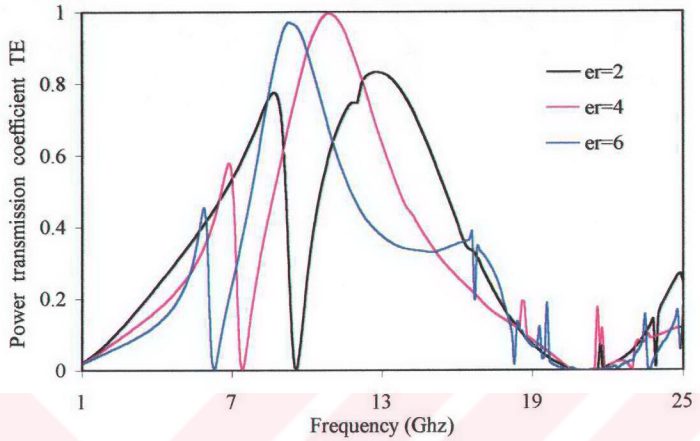
Figure 4.6. Normalized power reflection and transmission coefficients against frequency for different values of slab thickness ; TM normal incidence, $\xi = 0.003$ S and $\epsilon_r = 2.0$. (a) – Power reflection coefficient TM , (b) – Power transmission coefficient TM , (c)–Power transmission coefficient TE.



(a)

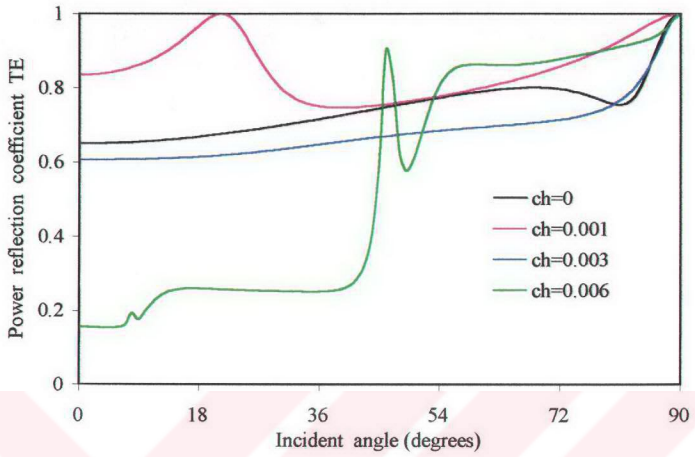


(b)

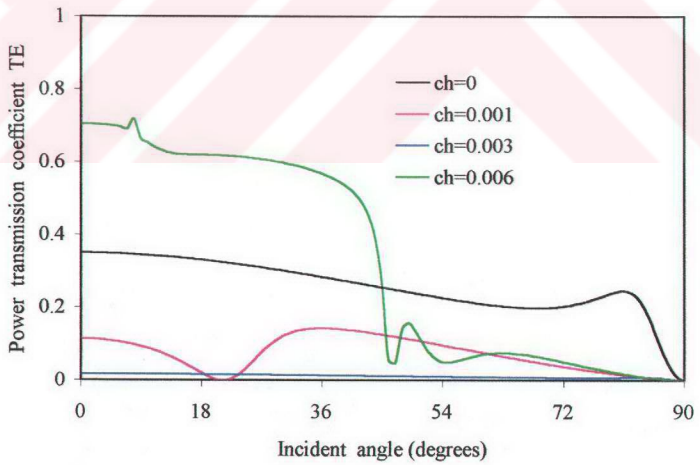


(c)

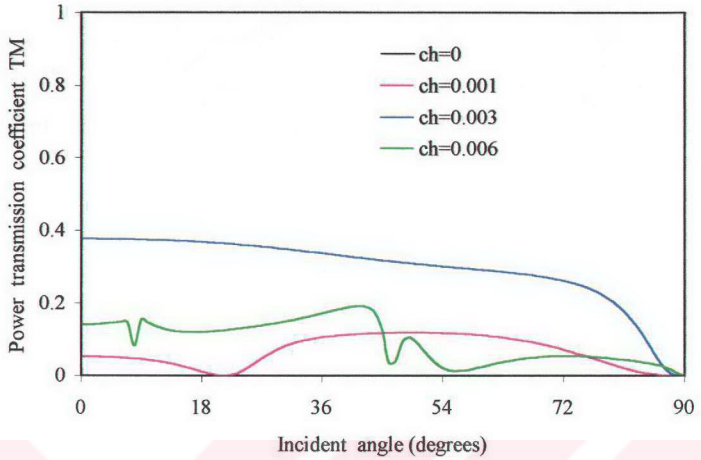
Figure 4.7. Normalized power reflection and transmission coefficients against frequency for different values of dielectric constants; TM normal incidence, $\xi=0.003$ S and $d=6.25$ mm. (a) – Power reflection coefficient TM, (b) – Power transmission coefficient TM, (c)–Power transmission coefficient TE.



(a)

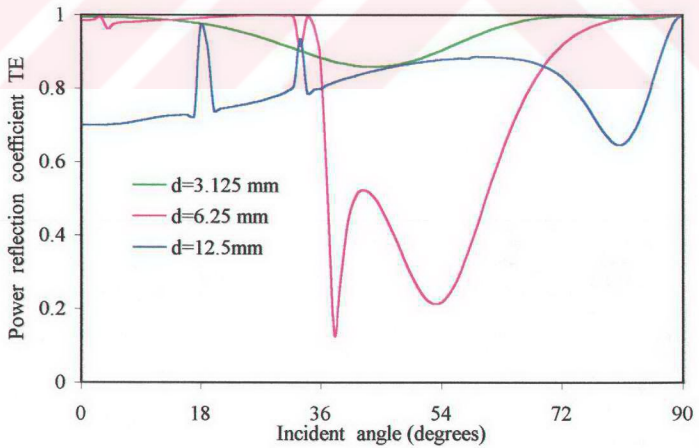


(b)

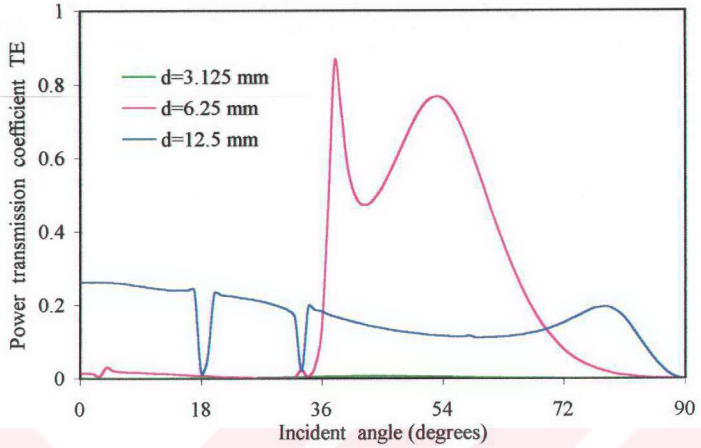


(c)

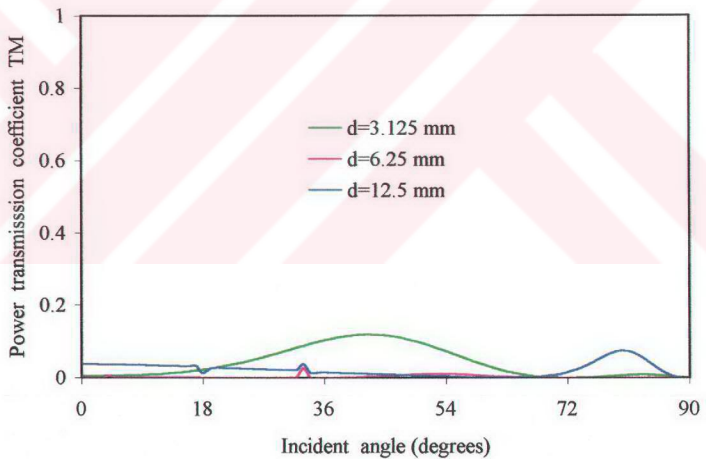
Figure 4.8. Normalized power reflection and transmission coefficients against incident angle θ for different values of chirality admittances; TE incidence, $\epsilon_r=9$ and $d=6.25$ mm. (a) – Power reflection coefficient TE, (b) – Power transmission coefficient TE, (c) – Power transmission coefficient TM.



(a)

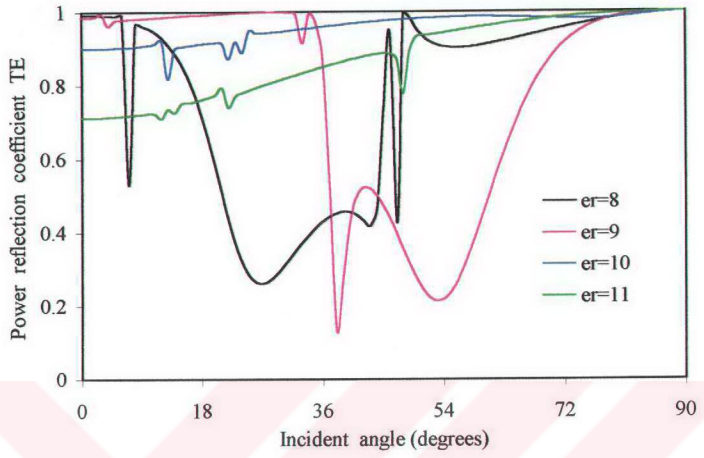


(b)

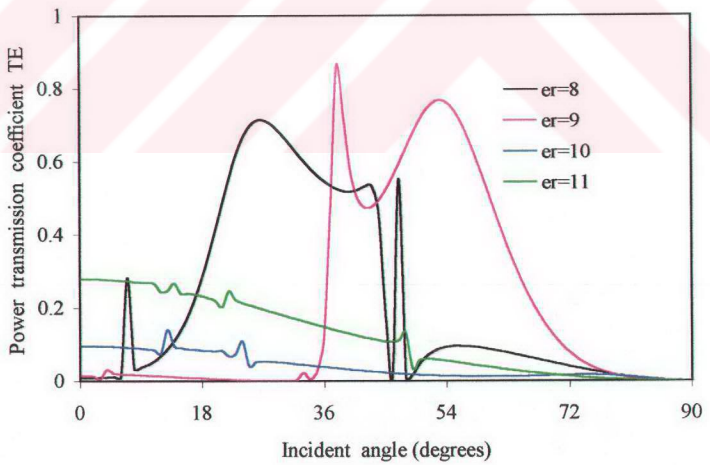


(c)

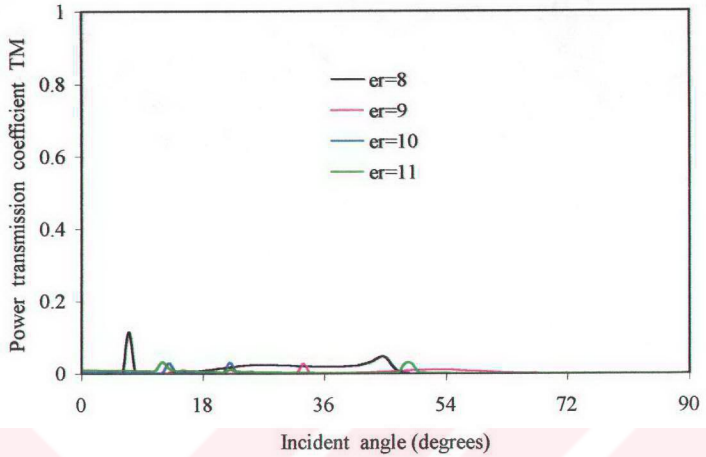
Figure 4.9. Normalized power reflection and transmission coefficients against incident angle θ for different values of slab thickness; TE incidence, $\xi=0.005$ and $\epsilon_r=9$. (a) – Power reflection coefficient TE, (b) – Power transmission coefficient TE, (c) – Power transmission coefficient TM.



(a)

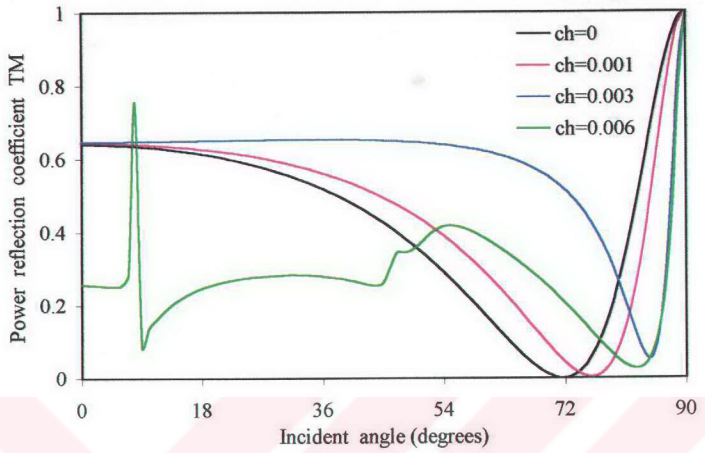


(b)

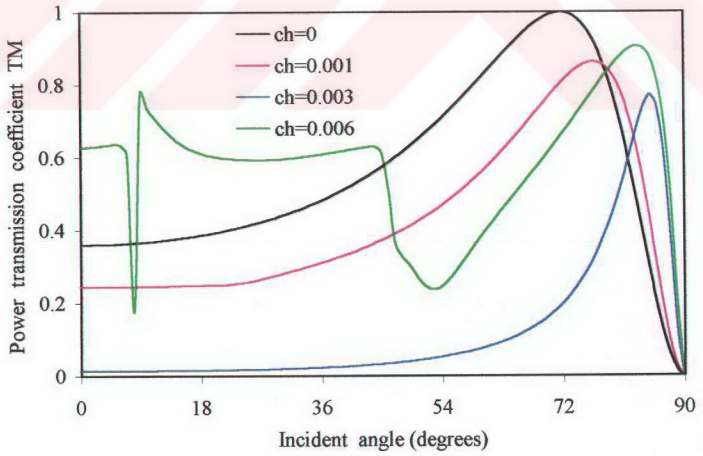


(c)

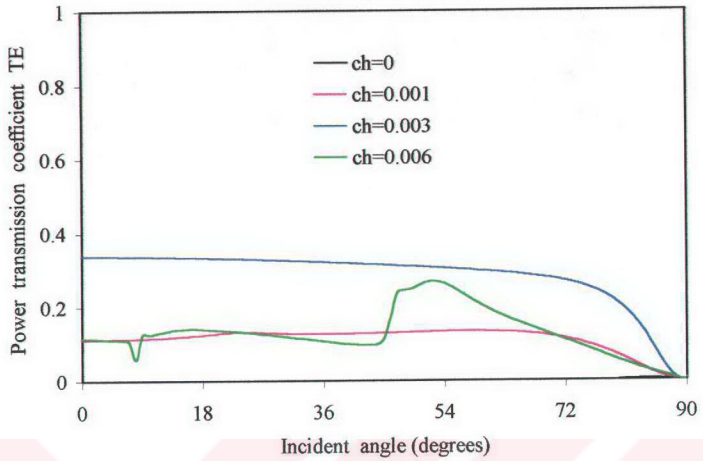
Figure 4.10. Normalized power reflection and transmission coefficients against incident angle θ for different values of dielectric constant; TE incidence and $\xi=0.005$, $d=6.25$ mm. (a) – Power reflection coefficient TE, (b) – Power transmission coefficient TE, (c) – Power transmission coefficient TM.



(a)

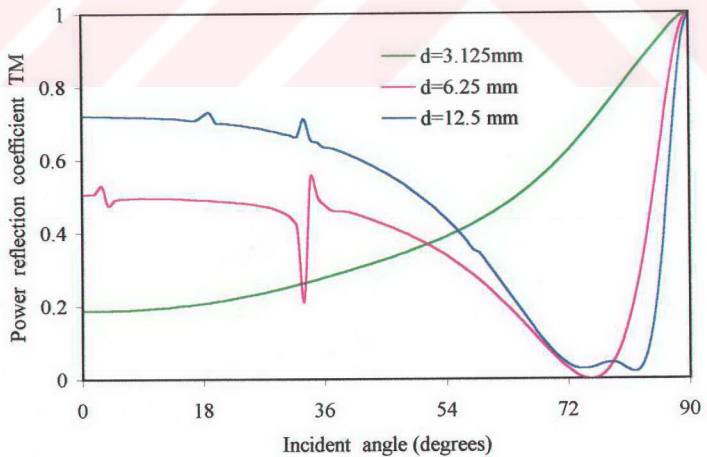


(b)

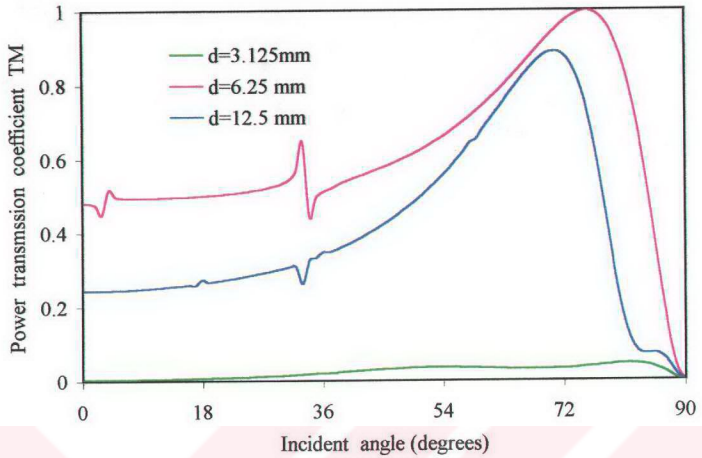


(c)

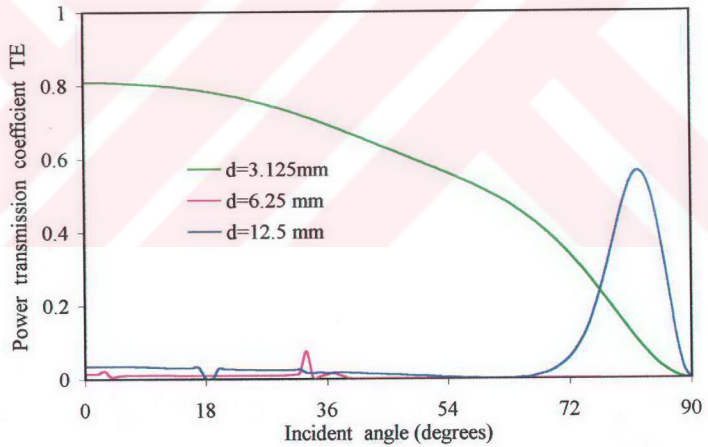
Figure 4.11. Normalized power reflection and transmission coefficients against incident angle θ for different values of chirality admittances; TM incidence, $\epsilon_r=9$ and $d=6.25$ mm. (a) – Power reflection coefficient TM, (b) – Power transmission coefficient TM, (c) – Power transmission coefficient TE.



(a)

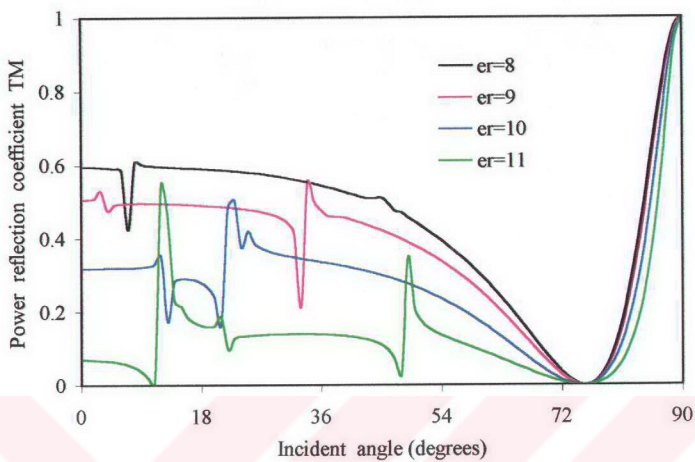


(b)

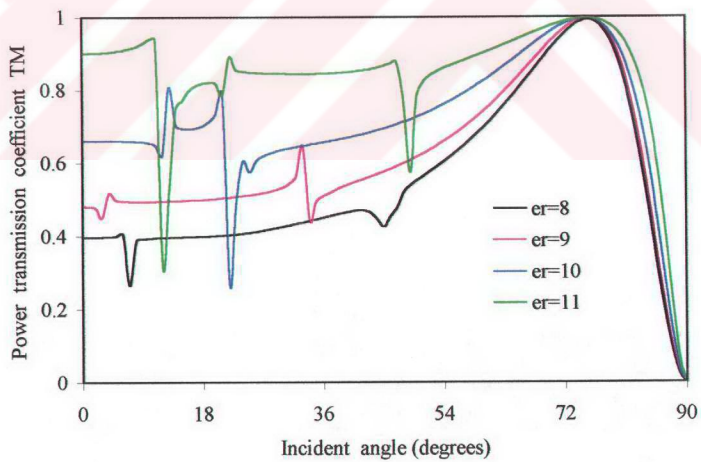


(c)

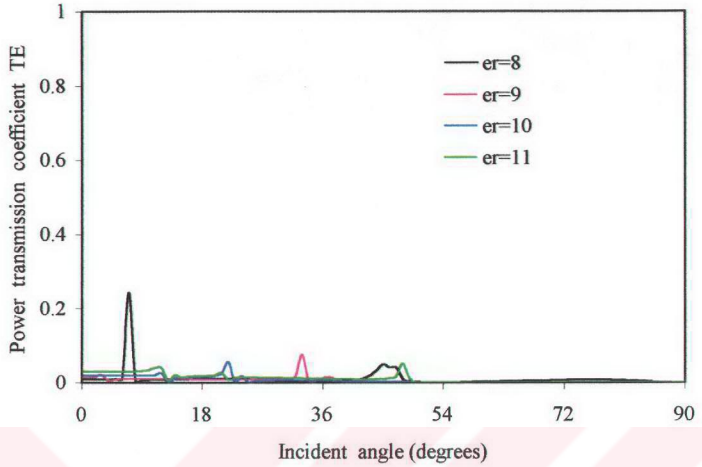
Figure 4.12. Normalized power reflection and transmission coefficients against incident angle θ for different values of slab thickness; TM incidence, $\xi=0.005$ S and $\epsilon_r=9$. (a) – Power reflection coefficient TM, (b) – Power transmission coefficient TM, (c) – Power transmission coefficient TE.



(a)



(b)



(c)

Figure 4.13. Normalized power reflection and transmission coefficients against incident angle θ for different values of dielectric constant; TM incidence, $\xi=0.005$ S and $d=6.25$ mm. (a) – Power reflection coefficient TM, (b) – Power transmission coefficient TM, (c)–Power transmission coefficient TE.

CHAPTER 5

CONCLUSION

In this thesis, the power reflection and transmission coefficients of chiral slab and meander-line polarizer with chiral slab were studied. They were plotted with respect to frequency and incident angle for different values of the chirality admittance, slab thickness and dielectric constant of chiral slab.

For the chiral slab without meander-line polarizer, we assumed that the incident field is the linearly polarized plane wave of either TE or TM polarization. When the chiral slab was illuminated with a normally incident linearly polarized wave, the reflected wave did not contain any cross polarization for its electric field. For normal incidence the amplitudes of power reflection and transmission coefficients were exactly the same for both TE and TM case. The cross-polar power reflection and transmission coefficients were the same for both TE and TM waves whatever the variables being used for chiral slab. It was seen that the chirality admittance was the most effective design parameter such that any small change in chirality admittance caused much variation in power reflection and transmission coefficients. When TE (co-polar) wave was incident on a chiral slab, full transmission was observed for the cross-polar (TM) power transmission coefficient. For this reason, chiral slab can be used as a TE to TM converter or vice versa. There was a Brewster angle for TM polarization but not for TE case for a chiral slab. The energy flow of the reflected and transmitted waves satisfied the law of energy conservation.

For meander-line polarizer with chiral slab, we applied the Moment method to find the unknown current density induced on the meander-line strips by suitable basis functions. After finding unknown current coefficients by means of matrix inversion, the reflection and transmission coefficients were

computed. The resonant frequency was the same for different values of chirality admittance and slab thickness. The resonance frequencies were shifted to lower frequencies for different values of dielectric constant and more resonances appeared at high frequencies for TM incident plane wave. More resonances were also obtained for TE incident wave and the resonant frequencies were shifted to lower frequencies by narrowing their bandwidths for different values of chirality admittance. There was a Brewster angle for TM incident plane wave and no Brewster angle was observed for TE incident plane wave.

Chiral media have found many potential applications in the fields of electromagnetic and microwave. In the light of this study several suggestions can be put forward for further research. The method used in this study can be extended for the cascade connections. It is known that chiral slabs can be used as polarization transformers which transform any incoming polarization into any other polarization by rotating the axes of the two slabs of certain angles. That is why the results obtained in Chapter 2, chiral slab without meander – line polarizer, can be used in the study of polarization transformers. A linearly polarized wave can be converted to a circularly polarized wave by using meander – line strips on a dielectric slab. In this case the design parameters are the dimensions of the strips and the dielectric slab. If dielectric slab is interchanged with a chiral slab the number of variation parameters will be increased by an effective parameter, chirality admittance. This presents an alternative for the design parameters.

REFERENCES

1. D. F. Arago, Mem. Inst., vol. 1, p 93-134, 1811.
2. J. B. Biot, Mem. Inst. vol. 1, p 1-372, 1812.
3. J. B. Biot, Mem. Acad. Sci. vol. 2, p 41-136, 1817.
4. J. B. Biot, Mem. Acad. Sci. vol. 13, p 39-175, 1835.
5. J. B. Biot, Bull. Soc. Philomath. p 190-192, 1815.
6. A. Fresnel, Oeuvres, vol. 1, p 731-751, 1822.
7. L. Pasteur, Ann. Chim. Phys. vol. 24, p 442-459, 1848.
8. K. F. Lindman, Ann. Phys. vol. 63, p 621-644, 1920.
9. K. F. Lindman, Ann. Phys. vol. 69, p 270-284, 1922.
10. W.H. Pickering, California Institute of Technology, Pasadena, California 91125 (personal communication), 1945.
11. S. Bassiri, C. H. Papas, and N. Engheta, “ Electromagnetic Wave Propagation Through a Dielectric - Chiral Interface and Through a Chiral Slab ”, J. Opt. Soc. Am. A, v 5, n 9, p 1450-1459, Sep 1988.
12. D.L. Jaggart, N. Engheta, M.W. Kowarz, P. Pelet, J.C. Liu, and Y. Kim, “ Periodic Chiral Structures ”, IEEE Trans. on Antennas and Propagat., v 37, n 11, p 1447-1452, Nov 1989.
13. A. J. Viitanen and I. V. Lindell, “ Uniaxial Chiral Quarter – Wave Polarisation Transformer ”, Electronic Letters, vol. 29, no. 12, Jun 1993.
14. T. Guire, V.V. Varadan, and V. K. Varadan, “ Influence of the Chirality on the Reflection of EM Waves by Planar Dielectric Slabs ”, IEEE Trans. on Electromagnetic Compatibility, v 32, n 4, p 300-303, Nov 1990.

15. H. Cory and I. Rosenhouse, "Electromagnetic Wave Propagation along a Chiral Slab", IEE Proceedings, Part H: Microwave Antennas and Propagation, v 39, n 5, p 676–677 May, 1991.
16. M. S. Kluskens and E. H. Newman, "Image Theory for Chiral Bodies", IEEE Transactions on Antennas and Propagation, v 39, n 5, p 676-677 May, 1991.
17. K. A. Barsukov and L. N. Kiseleva, "Surface Wave in chiral Media", Optics and Spectroscopy (English translation of Optika i Spektroskopiya), v 73, n 1, p 75-78, Jul 1992.
18. P. Hillion, "Plane Waves in Chiral Media", Optik (Stuttgart) v 98, n 4, p 147-152, Feb 1995.
19. Lekner J. "Optical Properties of Isotropic Chiral Media", Pure and Applied Optics: Journal of the European Optical Society Part A, v 5, n 4, p 417-443, Jul 1996.
20. L. Young, L. A. Robinson, and C. A. Hacking, "Meander-line Polariser", IEEE Trans. Propagat., 21, 376, May 1973.
21. J. P. Montgomery, "Scattering by an Infinite Periodic Array of Thin Conductors on a Dielectric Sheet", IEEE Trans. Antennas Propagat., 23, 70 1975
22. J. R. Levré, C. Terret, K. Mahdjoubi, and B. Lavigne, "Scattering by an Infinite Two-dimensional Periodic of Meander-line Thin Conductors on a Dielectric Sheet", Proc. 3rd Int. Conf. Antennas Propagat. ICAP-83, 1, Norwich (U.K.), 258 Apr. 1983.
23. P. Poey and P. L. Guigue, "Determination of the current distribution on an Infinite Periodic Structure of Thin-Metallic Wires", IEEE Trans. Antennas Propagat., vol. AP-32, No.1, January, 1984.

24. R. S. Chu and K. M. Lee, "Analytical Model of Multilayered Meander-line Polariser Plate with Normal and Oblique Plane-wave Incidence", IEEE Trans. Antennas and Propagat., 35, 652 Jun 1987.
25. S. Makino, N. Miyahara, H. Mizutamari, S. Urasaki, "Design of Meander-Line Polariser with Three Layers", Electronics & Communications in Japan, Part 1: Communications, v 72 n 11 p 35-42 Nov 1989.
26. S. Uckun, T. Ege, "Computation of susceptance for thick meanderline polariser", Electronic Letters, v 27, n 22, p 2076-2077, Oct 1991
27. Te-Kao Wu, "Meander-line polariser for arbitrary rotation of linear polarisation", IEEE Microwave and Guided Wave Letters, v 4, n 6, p 199-201, Jun 1994.
28. A. K. Bhattacharya, T. J. Chwalek, "Analysis of multilayered meander line polariser", International Journal of Microwave and Millimeter -wave Computer-aided Engineering, v 7, n 6, p 442-454 Nov 1997.
29. K. Delihacioglu and S. Uckun "Calculation of the Reflection and Transmission Powers of Chiral Slab for TE and TM wave Excitations", Proceedings of 8th International Crimean Microwave Conference, Crimico'98, September 1998, Sevastopol, Crimea, Ukraine.
30. A. Lakhtakia, V. V. Varadan, and V. K. Varadan, "A Parametric Study of Microwave Reflection Characteristics of a Planar Achiral - Chiral Interface", IEEE Trans. Electromagnetic Compatibility EMC-28, p 90-95, 1986.
31. N. Engheta and D. L. Jaggard, "Electromagnetic Chirality and its Applications", IEEE Antennas and Propagation Society Newsletter, vol. 30, pp. 6-12, Oct. 1988.
32. N. Amitay, V. Galindo, and C. P. Wu, Theory and Analysis of Phased Array Antennas, Wiley - Interscience, New York, 1972.

33. R. F. Harrington, Field Computation by Moment Methods, New York: MacMillan, 1968.
34. C. Terret, J. R. Levrel, and K. Mahdioubi , “ Susceptance Computation of a Meander –Line Polarizer Layer ”, IEEE Transactions on Antennas and Propagation, vol. AP – 32 , no.9, September 1984.

